Bulk Coating Processes with Sodium Silicate Slurries

by

Charles William Rowe

B.S. Materials Science
Rice University, 1992

Submitted to the Department of Materials Science and Engineering on August 9, 1996 in partial fulfillment of the requirements for the degree of Doctor of Philosophy in Ceramics.

Massachusetts Institute of Technology
September 1996

Signature of Author . . . . . .
Department of Materials Science and Engineering
August 9, 1996

Certified by . . . . . .
Professor Michael J. Cima
Thesis Supervisor

Accepted by . . . . . .
Linn W. Hobbs
Chairman, Departmental Committee on Graduate Students

Bulk Coating Processes with Sodium Silicate Slurries

by

Charles W. Rowe

Submitted to the Department of Materials Science and Engineering

on August 9, 1996 in partial fulfillment of the requirements for the

degree of Doctor of Philosophy in Ceramics.

Abstract

A bulk coating process used to manufacture roofing granules was studied in this thesis. Roofing granules are crushed rock coated with a slurry of sodium silicate, clay and various pigments to give the granules color. The granules are used in the manufacture of asphalt roofing shingles. The research for this thesis was directed toward better control of the coating process to achieve higher quality coatings.

UV/Vis diffuse reflectance spectroscopy was used to measure the optical properties of the coatings. Separate measurements of diffuse and specular reflection detected no measurable specular reflection. The diffuse scatter from the coatings was a function of the thickness of the coating, and a minimum thickness of 25 μm is required to maintain a consistent granule color. Cross-sections of roofing granules produced by the current process show large variations in coating thickness; both above and below the critical thickness.

The initial spreading of the slurry onto the rock surface was found to be strongly enhanced by the presence of a small quantity of water on the rock surface prior to slurry application. The contact angle of the slurry on the rock was 131° on dry rock, but was reduced to 51° on wet rock. Rock temperature did not show any correlation with slurry spreading as long as the temperature was not too high for the film of water to remain on the rock until the slurry was applied.

Roofing granules are coated in rotary kiln mixers, and the slurry is injected by a single pipe onto the bed of granules in the mixer. Experiments showed that the slurry penetrates only the top fraction (typically 1/8) of the rock bed. Subsequent tumbling action of the mixer is required to complete slurry spreading. This penetration depth into the rock bed was found to be inversely proportional to the yield stress of the slurry used in the coating process. A model of a shear-thinning slurry penetrating a porous powder bed was developed and compared to the experimental data. The experimental results were predicted accurately by the model equation.

Residence time studies were performed on a roofing granule mixer and average granule velocities through the mixer were calculated. The geometry of the flights, or baffles, in

the mixer vary along its length, and average velocities for these sections were computed. The slowest velocity was in the screw flight section, where significant "back-mixing" is occurring. Residence time data were fitted to a mathematical model of a series of continuous flow stirred tank reactors (CSTR). The data indicated that 12 CSTR's were sufficient to reproduce the actual residence time distribution. A heat and moisture balance model of the mixer was developed using 12 CSTR's in series. The model was tuned using known conditions, and process parameters were varied to study the sensitivity of the process to various changes.

Solubility of the coatings in water is a major concern since the granule must remain in service on a roof for the length of the guarantee, typically 15-30 years. The silicate matrix and the coating are highly soluble in water after the mixing process. A firing step, typically 450 °C for 10 minutes, renders the coating insoluble. A reduction of coating solubility was achieved by adding an aluminum containing salt directly to the slurry. The concentration of aluminum required to match the solubility of silicate/ clay slurries caused the slurry to gel, and would not be useable in the coating process. Experimental data showed that aluminum ions released from the clay during the firing step reduce the solubility of the silicate matrix and prevent dissolution of the coating.

Thesis Supervisor: Michael J. Cima
Title: Norton Professor of Ceramics

Table of Contents

LIST OF FIGURES

LIST OF TABLES

LIST OF SYMBOLS USED

Chapter 2

a^*	Red-Green value on $L^*a^*b^*$ scale.
b^*	Blue-Yellow value on $L^*a^*b^*$ scale.
f(R)	Kubelka-Munk remission function.
I_o	Incident light intensity.
I_x	Light intensity at a distance x into the material.
K	Absorption coefficient.
L^*	Lightness value on $L^*a^*b^*$ scale. $L^*=0$ is black and $L^*=100$ is white.
R	Diffuse reflectance.
S	Scattering coefficient.
x	Light penetration distance.
μ	Linear absorption coefficient.

Chapter 3

A	Pre-exponential constant for penetration depth vs. yield stress (Eq. 3.7)
a	Pore radius.
B	Exponent for penetration depth vs. yield stress relation (Eq. 3.7).
b_n	nth quartile boundary.
D_{eff}	Effective diameter of a pore.
D_p	Particle diameter.
F	Force on slurry pushing it into a pore in the rock bed.
g	Acceleration of gravity.
h	Depth of the rock bed in the mixer.
high	Highest observed pixel value.
L	Half the width of the top surface of the rock bed.
low	Lowest observed pixel value.
n	Quartile boundary number. n=0,1,2,3,4.
P.D.	Penetration depth of slurry into rock bed.
p	Pressure
r	Mixer radius.
v	Flow rate
x	Distance between the axis of the mixer and the rock bed surface.
Y	Height of slurry head.
z	Penetration depth of slurry into pore.
z_y	Penetration depth of slurry into pore when shear stress equals τ_y.
ε	Void fraction.
η	Viscosity
θ	Half angle subtended by mixer rock bed.
ρ	Density of slurry.
τ_y	Yield stress.

Chapter 4

A	Area of the bed.
C	Concentration of a reactant in a CSTR
C_1	Output of the first CSTR in a series, input for the seconds CSTR.
$C_{1,t=0}$	Initial concentration of a reactant in a CSTR (t=0).
C_2	Output of the second CSTR in series.
$c_{p,air}$	Heat capacity of air.
$c_{p,rock}$	Heat capacity of the rock.
$c_{p,solids}$	Heat capacity of the slurry solids.
$c_{p,vap}$	Heat capacity of water vapor.
$c_{p,water}$	Heat capacity of water.
f	Fractional solids content of the slurry.
$F(s)$	Laplace transform of $C_1(t)$.
F_{input}, F_{output}	Input and output flow rate from a CSTR.
h	Heat transfer coefficient.
ΔA, $h_m A$	Model optimization parameters.
h_m	Mass transfer coefficient.
H_n	Humidity ratio in the nth CSTR. n=1..12. Humidity ratio is the mass of water vapor divided by the mass of dry air.
m_{slurry}	Slurry application rate.
$m_{vap,n}$	Mass of water vaporized in the nth CSTR .
MW_{air}	Molecular weight of air.
m_{water}	Water application rate
MW_{water}	Molecular weight of water.
P_{sat}	Saturation vapor pressure of water.
P_{total}	Total pressure in the system. Atmospheric pressure.
Q	Volumetric flow rate.
ΔQ	Heat exchanged between rock/slurry stream and the air stream.
Q_a	Air flow rate.
Q_{rock}	Rock flow rate.
$Q_{w,0}$	Rock moisture content after slurry injection. Input rock moisture for CSTR #1.
$Q_{w,n}$	Rock moisture content in the nth CSTR. n=1..12.
R	Universal gas constant.
$R_{reaction}$	Reaction rate in a CSTR.
$T_{a,13}$	Air inlet temperature. Input for CSTR #12.
$T_{a,n}$	Air temperature in the nth CSTR. n=1..12.
$T_{a,n+1}$	Temperature of the air in the $(n+1)$th CSTR. Input to the nth CSTR.
$T_{r,-1}$	Rock temperature after water injection.
$T_{r,-2}$	Rock inlet temperature.
$T_{r,0}$	Rock temperature after slurry application. Input rock temperature for CSTR #1.
$T_{r,n}$	Rock temperature in the nth CSTR. n=1..12.

$T_{r,n,i}$	Temperature of the rock in the *n*th CSTR in the *i*th iteration.
$T_{r,n,i-1}$	Temperature of the rock in the *n*th CSTR in the *(i-1)*th iteration.
$T_{r,n-1}$	Temperature of the rock in the *(n-1)*th CSTR. Input to the *n*th CSTR.
T_{slurry}	Slurry application temperature.
T_{water}	Temperature of the injected water.
V	CSTR volume.
V_T	Total volume of a series of CSTR's.
$\delta(t-t_o)$	Delta impulse function applied at $t=t_O$.
ϕ	Percent relative humidity.
λ_{water}	Latent heat of evaporation of water.
$\rho_{sat.air}$	Density of air saturated with water vapor.
τ	Characteristic time constant of a CSTR (Eq. 4.8)

Chapter 5

A	Surface area of the leach sample.
C	Concentration of ions in solution.
C_s	Concentration of standard solution.
E	Measured electrode potential.
E_{10}	Measured potential in the 10 ppm standard.
E_{100}	Measured potential in the 100 ppm standard.
m_l	Mass leached.
rate	Leach rate.
S	Electrode slope.
t	Duration of the leach test.
V_l	Leach solution volume analyzed.
V_o	Leach solution volume.

ACKNOWLEDGEMENTS

There are many people that I would like to thank for contributions toward my thesis. First of all, I would like to thank my advisor, Professor Michael Cima for his guidance and suggestions throughout my thesis research. I would also like to thank: Professor Yet-Ming Chiang and Professor Donald R. Sadoway for contributing their time to serve on my thesis committee, John Centorino and Lenny Rigione for all the answers to my questions and their assistance in the laboratory, Barbara Layne for all those details she took care of, and Mike Frongillo for his help with the TEM.

I would like to thank 3M Corp. for sponsoring this research and Robert Messner, Pete Flemings, and Vince Lariah for answering all my questions.

Many other people have made my life more bearable during my four years at MIT, and I would like to express my thanks: Kevin and Barbara for lunches at Mary Chung's; Ben, Bob, Jason, Ken, and Lynne for making the office a fun place to work; and the other CPRLers: Bugra, Cesare, Jae, John, Kamala, Karina, Mike, Neville, and Todd. Many thanks to the MIT Figure Skating Club and Louise Silver for teaching me to skate and giving me such a fun way to avoid work.

Many thanks to Stephen for putting up with me while I wrote my thesis, and to my family for all their encouragement and support of my education.

CHAPTER 1
INTRODUCTION TO BULK COATING PROCESSES

Bulk coating processes are important in many industries for coating of macroscopic parts with films based on polymers and/or ceramics. Pharmaceuticals, food production and handling, roofing materials, and agriculture are four industries that use bulk coating in their manufacturing processes. This chapter will examine the various techniques, materials, and uses of these types of coatings.

1.1 FOOD PRODUCTION AND HANDLING

1.1.1 FRUITS AND VEGATABLES

Fruits and vegetables are frequently coated with various polymeric and waxy coatings in order to improve storage life, appearance, and texture during shipping and sale of the product. These coatings were developed to replace or supplement the more traditional controlled atmosphere storage that uses a combination of cold temperatures and atmospheric gases to preserve the fruit. Such methods require large capital outlays and maintenance and are impractical for small scale storage in retail stores.[1] Studies have shown that coating the fruit's outer skin can control the interior atmosphere of each individual fruit.

Several properties are required of these coatings. The coatings will be applied to food products so they must be edible without altering the taste of the fruit. The coatings often are required to posses high surface finishes to improve perceived appearance. Coating permeability to oxygen, carbon dioxide, and water vapor is crucially important to its function to control the atmosphere inside the fruit. Thickness control is especially

important to the process since coatings that are too thick slow down gas diffusion and can lead to reduced oxygen and increased carbon dioxide levels in the fruit, causing anaerobic fermentation problems.[2]

Typical coated foods are soft fruits and vegetables such as apples[1], tomatoes[2], and cucumbers. Sucrose ester coatings are used on apples[1] and tomatoes[2] to maintain texture and firmness, while waxes are common on apples and cucumbers to prevent water loss.

Industrial coating of fruits and vegetables involves methods such as dipping, brushing, and spraying. All three types of processes apply an aqueous solution of the coating material to the fruit as it moves on some type of conveyor system. The coating is allowed to dry in a forced air stream. This process does not use tumbling of the parts because of possible damage to the fruit.

1.1.2 CANDY MANUFACTURE

Another food production bulk coating process is found in the candy industry which produces many types of products with a layered structure. These layers are applied in sequence over a central core. The functions of the layers include changes in color, taste, and appearance of the candy. One such process is the manufacture of M&M Candies by the M&M Mars Co.[3] The coatings are applied to the chocolate centers of the candies and consist of sugar solutions that contain dyes to color the M&M's. Up to ten such coatings may be applied. Clear sugar surface finish coatings are applied on top of the color layers to provide a gloss appearance. Evenly distributed color and high surface luster are important to customer perception of the product.

Both types of coatings are applied in a pan coating process. Pan coating is a batch process in which the parts to be coated are placed in a rotary reactor and the coating slurry or solution is applied by an injection pipe or spray nozzle while the parts are tumbled. The process involves simultaneous spreading and drying/ hardening of the coating slurry. The coated parts are removed from the reactor when the coating has reached sufficient mechanical stability to withstand further processing.

The sugar solutions used in the manufacture of M&M's are aqueous sugar syrups. The viscosity of the coating slurry increases as the coating cools. Batch time and operating parameters such as rotation speed of the pan coater must be optimized for the particular coating process in order to ensure an even coating on each part and proper surface finish. Coating slurry that dries and hardens too quickly in the pan coater will not sufficiently coat all the parts to optimum thickness. This results in spotty color of the finished M&M, or poor surface luster.[3] Operating conditions which inhibit drying of the slurry cause longer batch times to be necessary and slow down the manufacturing process.

M&M Mars company has investigated the possibility of using a continuous process rather than a batch process in the manufacture of M&M's. These studies show that the initial spreading of the colored dye/ sugar syrup is the critical phase in the production of high quality coatings, but changes in the core shape, such as with almond M&M's, have a large impact on coating mechanics.[3]

1.2 PHARMACEUTICAL INDUSTRY

The pharmaceutical industry uses pan coating as well as other bulk coating techniques in the production of drug-containing tablets and capsules. The coatings are used to mask taste or odor of ingredients in the tablet, to protect an ingredient which is moisture sensitive, to change the appearance of the tablet[4], or to control the release rate of one or more of the drugs in the tablet or capsule.[5]

Materials used in pan coating of tablets vary widely and can include: hydroxypropyl methylcellulose, ethylcellulose, methacrylic acid ester copolymers, polyethylene glycol, sugars, dyes, and various plasticizers for altering coated film properties.[4] Sugar coatings are applied in a manner similar to M&M's: a hot syrup is applied to the tablets and allowed to spread while cooling. The organic polymer coatings are achieved by mixing the polymer and any plasticizers in a suitable solvent. The solution is applied to the tumbling tablets in the pan coater, the solvent is evaporated, and the polymer remains on the tablet forming a film. Concerns about residual organic solvents in the tablets and

environmental issues of solvent recovery have lead researchers to develop water based coatings systems using suspensions of polymer particles. Other coatings include waxes used in polishing coats, and shellac resins used as sealers between layers.[4]

Pan coating equipment varies greatly depending on the particular process, but the basic component is the pan itself. Figure 1.1 depicts several pan coaters. Design parameters that affect the process include: shape, tilt angle, rotation speed, inlet ports for applying coating materials, and ports for drying gas flow. Some pans have solid walls and have gas flowing through the reactor via ports in the front and back. Others allow gas to escape through perforated walls to increase the contact between the drying gas and the tablets so that drying rates are increased.[4]

Optional baffles or flights are sometimes included to aid in the tumbling action of the coated parts. Increased tumbling of the parts enhances uniformity of coating thickness on each part and between parts in the batch. Size and shape of the baffles is highly variable and is optimized for the process involved. Mechanical stability of the tablet core is an important consideration in the selection of baffles since increased agitation can lead to erosion of the tablets due to impact.[4]

Coating slurry is usually applied to the moving bed by a spray nozzle arrangement. The nozzle can be positioned above the bed. Other spray systems atomize the spray into the drying air stream which is introduced into the middle of the tablet bed. This promotes higher drying efficiency; see Figure 1.2.[4]

Drying rate control is crucial for high quality coating formation. High application rates of coating solution or low drying rates cause adjacent tablets to stick together. The b dge of coating material will fracture on subsequent tumbling, leaving a roughened area on both tablets and/or an uncoated area on one of the tablets. This phenomenon is known as picking. High drying rates cause the droplets to dry before they arrive at the tablet surface. These droplets will not be able to spread into a continuous film, and thickness variations and high surface roughness will result.[4]

Spray-drying is used to coat smaller solid drug-containing cores, usually referred to as microencapsulation. Microencapsulation generally refers to coating processes involving parts on the order of 1-3 mm in diameter or less. Tablet coating, by contrast, deals with

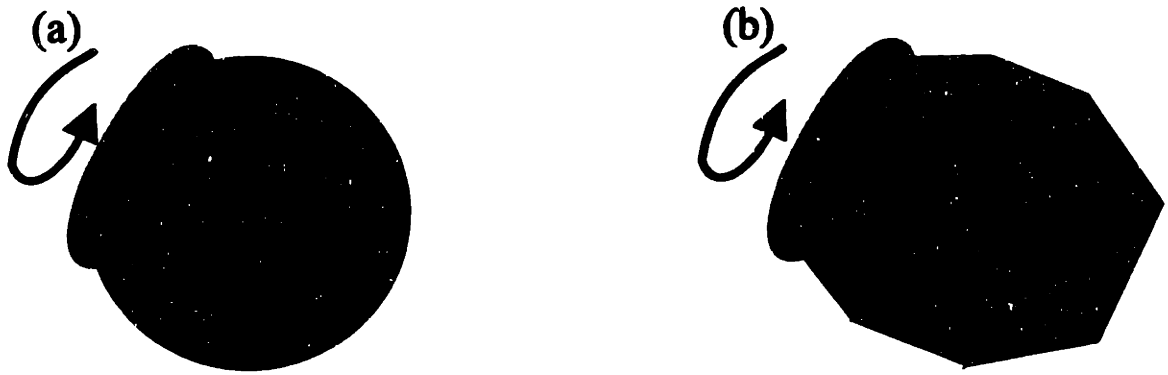

Figure 1.1 Schematic diagram of two pan coater designs: (a) spherical; (b) hexagonal. Typical pan sizes are 0.5-3.0 m in diameter, and typical rotation speeds are 1-10 rpm.

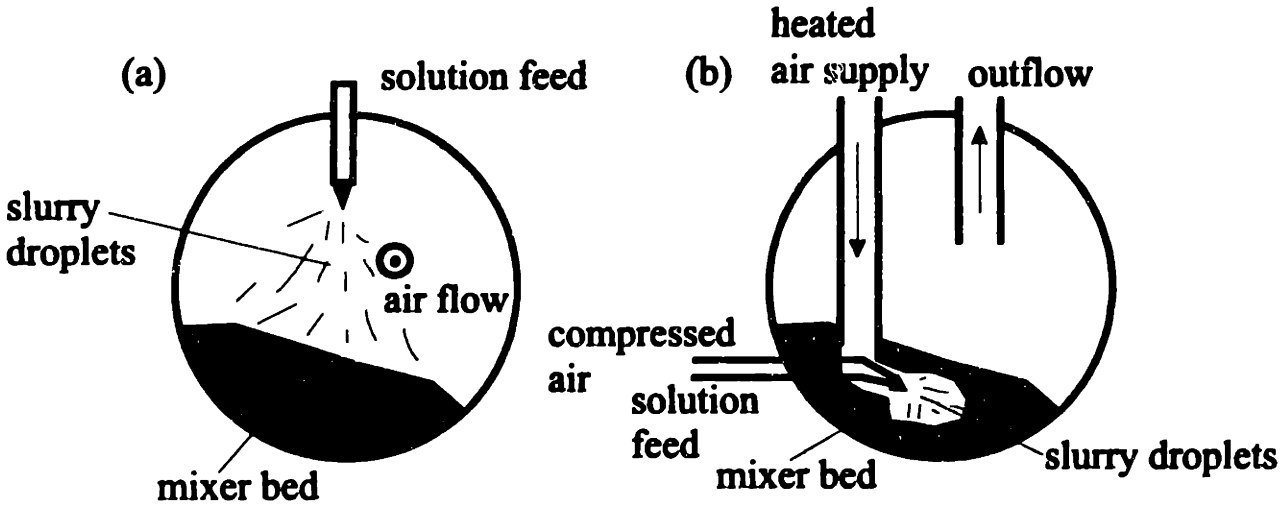

Figure 1.2 Two methods of slurry injection in pan coating: (a) above the bed; (b) inside the bed.

parts of at least several millimeters. Spray-dried coatings are produced by suspending the solids in a solution containing the coating material. The suspension is then atomized into a high temperature air stream and the coating forms as the solvent is removed. This process usually produces aggregates, rather than individual coated particles.[6]

Aqueous coacervation techniques are also used to microencapsulate drugs. The solid parts to be coated are suspended in a solvent containing the coating material in solution or colloidal form. Induced chemical or physical changes cause the coating material to preferentially deposit on the solid cores and form a film.[6]

Examples of the induced changes that cause coacervation and film formation include chemical additions that cause the coating material to become insoluble in the coacervation medium (usually aqueous-based) and salt out on the solid cores. A gelatin coating can be prepared with this technique using Na_2SO_4 as a coacervation agent.[6]

Carboxymethyl ethylcellulose coatings are formed on aspirin granules by dissolving the polymer in an alkali aqueous solution and then adding the drug cores. Aspirin is slightly water soluble and acidic. Small amounts of the drug dissolve in the coating medium, neutralizing the basic solution. This causes the polymer to become locally insoluble and it precipitates onto the drug core surface.[7]

Ascorbic acid can be coated with ethylcellulose by dissolving the polymer in cyclohexane and a coacervation agent such as polyethylene. The solution is heated to 78 °C and the ascorbic acid granules are added. The solution is then cooled, causing the ethylcellulose to form a coating.[8]

Spouted bed or fluidized bed processes are also used for bulk coating in the pharmaceutical industry. Lactose tablets are coated with a latex copolymer coating in this manner.[9] Spouted bed coating is performed by loading the parts to be coated into a reactor. The granule bed is then fluidized by injecting compressed air from underneath. The air can be injected in a single location creating a spouted bed, or in multiple locations creating a fluidized bed; see Figure 1.3. The coating solution is atomized and introduced into the input air stream and allowed to contact the granule bed. The air flow that fluidizes the bed also serves to evaporate the solvents and dry the coating.[9] Other systems spray the coating solution onto the top surface of the fluidized bed.[5]

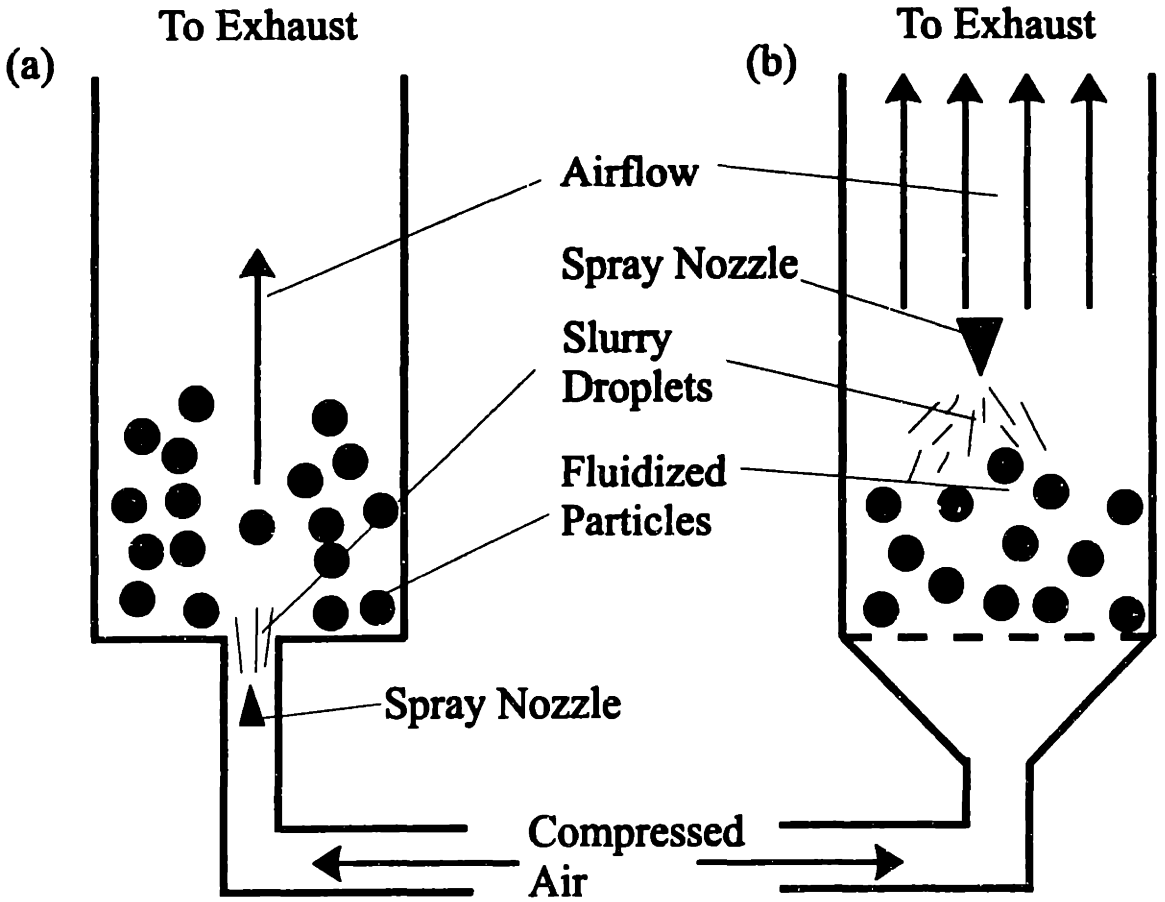

Figure 1.3 Schematic diagram of: (a) spouted bed and (b) fluidized bed coating processes.

Many tablet coatings and microencapsulations are designed to release the drug contained in the solid core at a specified rate, or after a specified delay. The reasons for this type of control include: side effects at high dosage levels or drug release in a specific segment of the gastrointestinal tract.[10] Membrane coating techniques are used to control the release rate of the drug. The coating material and process are optimized to produce a water-insoluble coating with a controlled porosity. Once in the body, gastric fluids enter the pores of the coating and attack the solid core. The drug is dissolved at a rate controlled by the number density and size of the pores in the coating.

Typical coating materials include polyvinyl pyrrolidone,[10] ethylcellulose.[11] Various granular water soluble additives are included in the coating solution to control the porosity of the films. These additives will later dissolve, creating the necessary pores. Number and size of the pores are controlled by the concentration and size of the particles added. These types of coating solutions are necessarily non-aqueous based. An ethanol-acetone mixture is a common solvent.[10]

Other porosity control techniques do not use granular additives which can complicate the film-formation process. Ethylcellulose coatings have been produced with controlled porosity by dissolving the polymer in an ethanol-water mixture. The exact ratio of the two solvent controls the density of the final film.[12]

1.3 AGRICULTURE

The agricultural industry also uses bulk coating processes. Plant seeds are often coated with fertilizer and pesticides before planting. The goal of such processes is to limit the application of such chemicals to the locations where they are needed, near the germinating seed, instead of spraying over entire fields. Cost reduction and reduced environmental impact are two goals of this process.

The seeds are coated in a spouted bed process similar to that used in the pharmaceutical tablet coating. The seeds are loaded into a cylindrical hopper and fluidized with a central jet of compressed air. The coating slurry, usually an aqueous solution of monocalcium

phosphate and tricalcium phosphate with a methylcellulose binder, is atomized into the inlet air stream. The atomized droplets strike the seeds and adhere. The solvent evaporates into the moving air stream as the coating dries.[13]

1.4 ROOFING MATERIALS

The roofing materials industry uses bulk coating processes to produce roofing granules, the first step in the manufacture of asphalt roofing shingles. These granules are typically a rock core coated with a thin layer of a sodium silicate based coating. The coating contains clays and pigments to alter the chemical and optical properties of the coating. A typical slurry formulation is 25 wt.% sodium silicate solids, 21 wt.% clay, 14 wt.% titania and 40 wt.% water.[14]

The granules are produced by crushing rock, screening to the proper size, and preheating to the coating temperature. The preheated rock is injected into a drum mixer where the coating slurry is applied. The tumbling action of the mixer spreads the slurry over the individual rocks, while the internal heat of the rock dries the slurry. Parallel or countercurrent air flow through the drum mixer removes the evaporated water. A low temperature firing process is performed after the granules emerge from the mixer to improve the mechanical stability and water resistance of the coating. The fired granules are mixed with other batches to achieve the proper color mixture and then pressed into asphalt sheets to make shingles.[14]

The drum coating process is similar to pan coating, except that the process is continuous rather than batch. Many of the issues, however, are the same for both processes. Process parameters must be optimized so that the product emerging from the mixer is at the proper stage of drying. A product that is too wet will still contain agglomerates which must be screened out of the final product. A coating that is too dry before final firing can delaminate from the substrate and leave portions of the granule uncoated. A major difference between pan coating and drum coating is that the former is a batch process so that residence time in the reactor is very precisely controlled.

Residence times in the drum mixer are not uniform for all parts being coated. There is a residence time distribution, centered around a mean.

The mean residence time and the width of the distribution depend on many parameters such as: mixer speed and tilt, internal baffle arrangements, mass flow rate, and slurry application rate. Mixer and baffle geometry are typically fixed and the operating conditions optimized to produce a product of the desired quality. The complicated relationships between the operating parameters and the resulting product properties make it difficult to predict the effects of a single change in process parameters.

The goal of this thesis is to investigate these relationships in order to provide better understanding of bulk coating processes in general and specific information on the sodium silicate based system chosen for study. Chapter 2 of the thesis will examine the properties required of the roofing granules, concentrating on the optical properties. The result of these studies is an optimal coating thickness for the process to achieve. Chapter 3 describes the initial contact of the slurry with the rock substrate after injection. Slurry spreading is also treated in this chapter. Residence time distributions and drying rates are discussed in Chapter 4. Chapter 5 covers the behavior of sodium silicate coatings in contact with water and the connection to roofing granule weathering on a roof. Chapter 6 presents a summary of the major conclusions from Chapters 2-5.

CHAPTER 2

OPTICAL PROPERTIES OF SODIUM SILICATE BASED COATINGS

2.1 INTRODUCTION

The main function of the roofing granule in an asphalt shingle is to provide color and texture. This property is one of the measures used to determine whether the process is operating correctly. Color consistency from batch to batch is a major concern since replacement shingles must match those that were manufactured and installed at an earlier date. This chapter will show that coating thickness has a large effect on the measured color of the coating, and thicker coatings have a more consistent color. The pigments are one of the most costly components in the coatings, so an optimum thickness exists.

Current industry tests evaluate color in terms of a three parameter scale called $L^*a^*b^*$.[14] The next section of this chapter will describe the current color test and discuss some of its inadequacies. The third section describes controlled laboratory experiments to address these issues and determine an optimum thickness. The fourth section discusses coating microstructure. The fifth section presents optical properties data showing that a minimum coating thickness for color consistency exists. This thickness is compared with actual coating thicknesses for commercial roofing granules. The sixth section discusses the applicability of the Kubelka-Munk assumptions and relates the minimum thickness observed to a light penetration model. The final section presents the conclusions of this chapter.

2.2 INDUSTRY STANDARD COLOR MEASUREMENTS

Current roofing granule industry color tests are measured on a representative sample of granules from the production line. A standard illuminant white light source is directed towards the sample from a prescribed distance, and the diffusely scattered light is collected. A monochrometer is used to separate wavelengths of interest and the measured light intensity is compared with light reflected from color standards.[15] The measurements returned are on the $L^*a^*b^*$ scale. Control values can be established for the production process, defining a cube in the three dimensional $L^*a^*b^*$ space in which the product is acceptable.

The $L^*a^*b^*$ scale was developed from the opposing color theory[16] and was established as a standard by the Commission Internationale de l'Eclairage (CIE).[17] Color is measured on three axes, the numerical value for each axis is a comparison of the colored sample to two opposing colors. The L^* axis, also known as the lightness value, is the comparison between black ($L^* = 0$) and white ($L^* = 100$). The a^* and b^* scales are red-green and blue-yellow comparisons, respectively.[16]

This three-axis measurement is an excellent tool for product evaluation and process control, but it is not a research tool. It is not clear from the instrument specifications how the three color numbers are measured and calculated. More representative data would include a continuous wavelength scan over all visible wavelengths.

There are some additional inadequacies in the test that are important for research and industrial use. The surface finish of the granules can strongly affect the measurement, since the measured reflectance is diffusely scattered light. Post-firing treatments such as oiling, which are used to inhibit dust, will interfere with the test. Standard industry tests require specific granule cleaning procedures to remove surface contaminants, but these water washes can erode the surface of the silicate coating.

The surface of the collection of granules that make up a sample also affects the diffusely scattered light. Variations in granule size and sample collection technique can introduce large variations and poor reproducibility of the measurements. Specific procedures must be implemented to ensure a narrow size distribution of granules and a

reproducible scattering surface. The scattering surface must have a reproducible number density of granules as well as a mean surface that can be oriented at a specific observing angle relative to the light source.

2.3 EXPERIMENTAL PROCEDURES

A scanning UV/Visible spectrophotometer (Beckman DU-640[18]) was used to provide reflectance versus wavelength data. The instrument was fitted with an integrating sphere (Labsphere Inc., RSA-BE-65[19]) to provide diffuse reflectance data. A schematic diagram of the apparatus appears in Figure 2.1. Light from the source is reflected by a series of mirrors through the input port of the integrating sphere. The light beam passes through the center of the sphere and strikes the sample at the sample port. Diffusely scattered light from the sample strikes the interior of the sphere which is coated with a low absorption coating. The geometry of the sphere concentrates the scattered light at the output port which sends it to the photodiode detector.

The sample holder has two geometries, 0° and 8° angular inclination of the surface normal, measured relative to the incoming beam. The relative amounts of diffuse scatter and specular reflection can be determined using measurements made at these two inclinations. Measurements carried out at the 0° inclination contain information on diffuse scatter only, since any specular reflection is reflected out the input port and is not collected by the sphere. Specular reflection is collected in the 8° measurement as well as the diffuse scatter. Subtraction of the spectra from the two techniques will yield a spectrum of specular reflectance only.

Surface effects discussed in Section 2.2 were eliminated by producing coatings by tape casting. Figure 2.2 is a schematic representation of the tape casting process. A doctor blade containing a slurry reservoir is moved across the substrate at a controlled speed. The height of the doctor blade is adjustable and is used to control the thickness of the cast film. Provided the slurry is of the proper viscosity, thickness accuracy of 1-2 μm can be achieved for films of 10-100 μm.

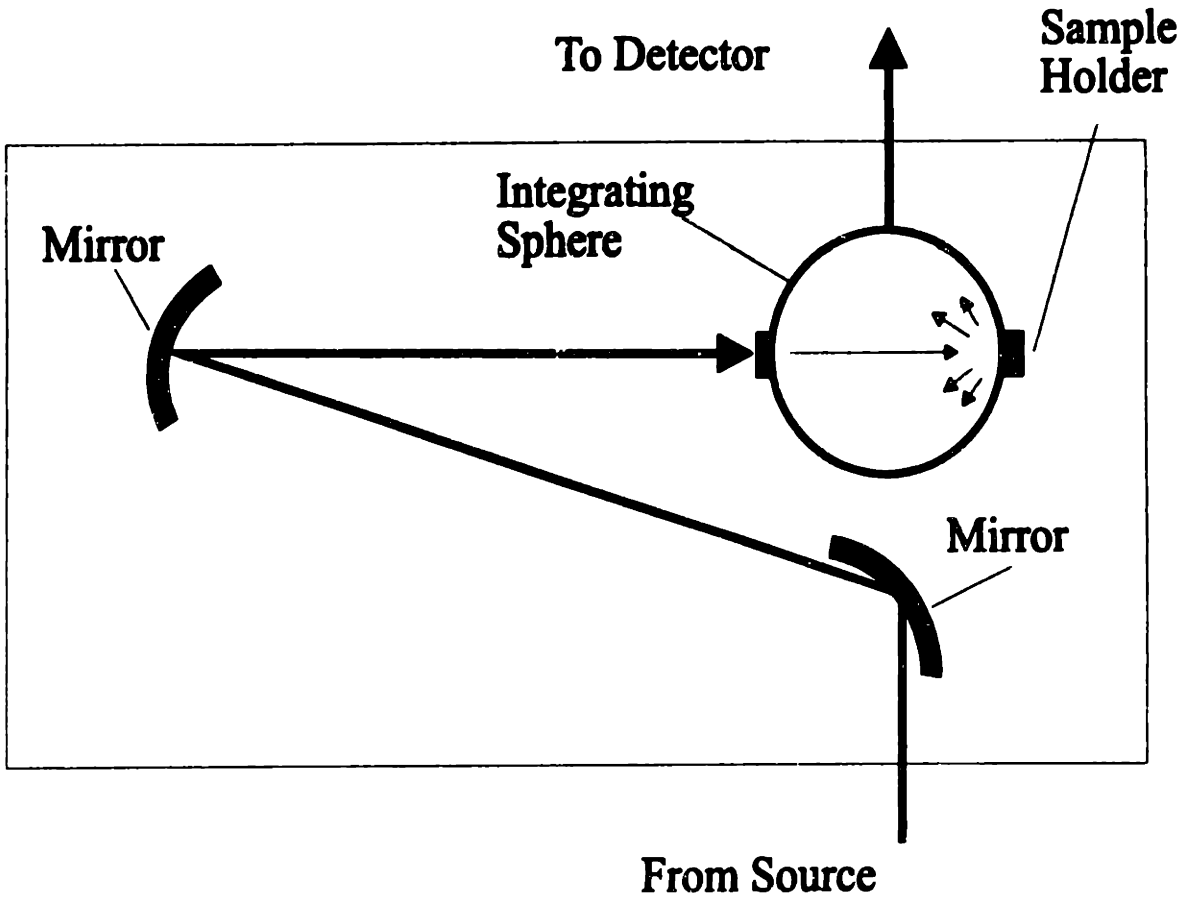

Figure 2.1 Schematic of the UV/Visible diffuse reflectance apparatus. Sphere diameter is 5 cm.

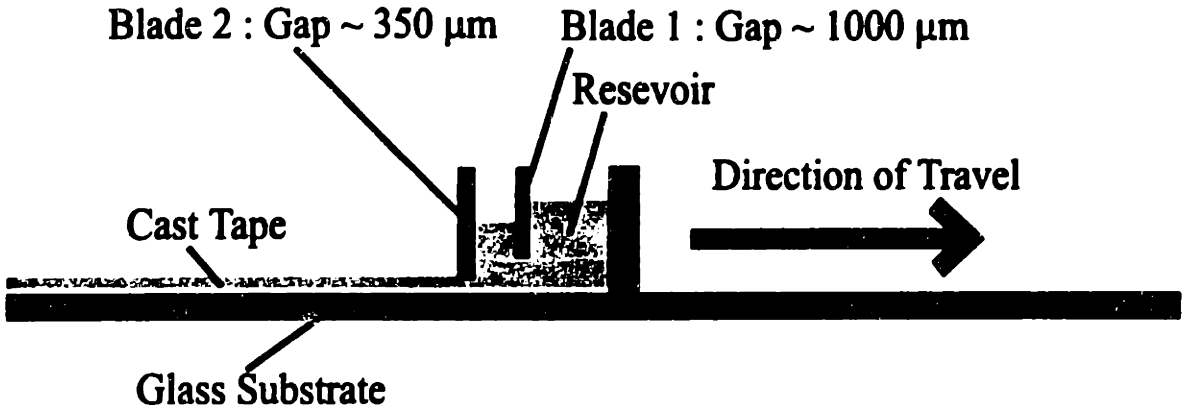

Figure 2.2 Schematic illustration of tape casting.

The substrates used for tape casting in this study were polished rock sections. The rock is similar to the raw quarry material used in industry. The rock was sectioned into slices approximately 5 cm x 10 cm x 0.5 cm in dimension and polished to 600 grit.[20]

The casting slurry was based on a typical industry slurry formula.[14] Additional water was added to the slurry to lower viscosity and make the casting consistent. Table 2.1 lists the casting parameters used to cast six tape cast coatings for use in this study. The coatings were allowed to dry in air for 12 hours after casting and then fired to 455°C. Thickness data were measured after firing with a calibrated optical microscope. The thickness measurement was made on a marked region that was later centered in the beam of the UV/Visible spectrophotometer.

Table 2.1 Tape Casting parameters used to cast sample coatings for UV/Vis diffuse reflectance measurements.

Run	Blade 1 (μm)	Blade 2 (μm)	Blade Speed (cm sec^{-1})	Fired Thickness (μm)
46A	980	350	1.27	40
46B	980	450	1.27	28
46C	980	550	1.27	72
47A	970	250	1.27	21
47B	970	250	1.27	12
47C	970	200	1.27	20

The coatings were scanned from 800 to 250 nm at a scan speed of 1200 nm/min. Each coating was scanned twenty times, and the scans were numerically averaged to yield a composite scan. The reflectance data collected were converted to Kubelka-Munk[21] absorbance units by the following formula.

$$f(R) = \frac{(1-R)^2}{2R} = \frac{K}{S} \tag{2.1}$$

where R is the measured reflectance and K and S are the absorption and scattering coefficients, respectively. Kubelka-Munk units were used to linearize the relationship between reflectance data and the concentration of scattering centers in a sample. The

procedure is similar to using the logarithm of transmittance for transmission measurements.

Several assumptions are implicit in the derivation of the Kubelka-Munk remission function in Equation 2.1. The derivation assumes that incoming light is scattered diffusely but not absorbed or specularly reflected by small scattering centers in the sample and multiple internal scattering events occur before the light reemerges from the sample. K and S are assumed to be constant throughout the medium and the layer is assumed to be optically "thick." The final assumption is that the scattering centers are sufficiently close such that their separation is much smaller than the layer thickness and the intervening medium between the particles does not significantly absorb any radiation.[22] The implications of these assumptions and their applicability to the tape cast coatings will be discussed in Section 2.4.2.

2.4 COATING MICROSTRUCTURE

Figure 2.3 is schematic of the tape cast coating microstructure and the interaction of light with the coating. The coating consists of a silicate matrix containing discrete particles of clay and pigment. Titania was the pigment chosen for the tape casting studies. Figures 2.4 and 2.5 are SEM micrographs of the clay and titania powder, respectively, as received from the supplier.[23] Typical particle sizes observed are 3-4 μm for the clay and 0.2 μm for the titania. The as-received clay particles are quite large due to agglomeration.

These agglomerates are broken up into individual particles when the powder is dispersed in the sodium silicate during the preparation of the slurry. Figure 2.6 is a TEM micrograph of a thinned coating prepared from sodium silicate and clay. The slurry was dispersed on a ball mill and cast onto a glass microscope slide by smearing. The film was allowed to dry in air and was mechanically removed from the substrate. A small section of the film was mounted on a TEM grid and thinned on an ion mill[24] until perforation. The thinning was done without the normal dimpling stage because the coating had not

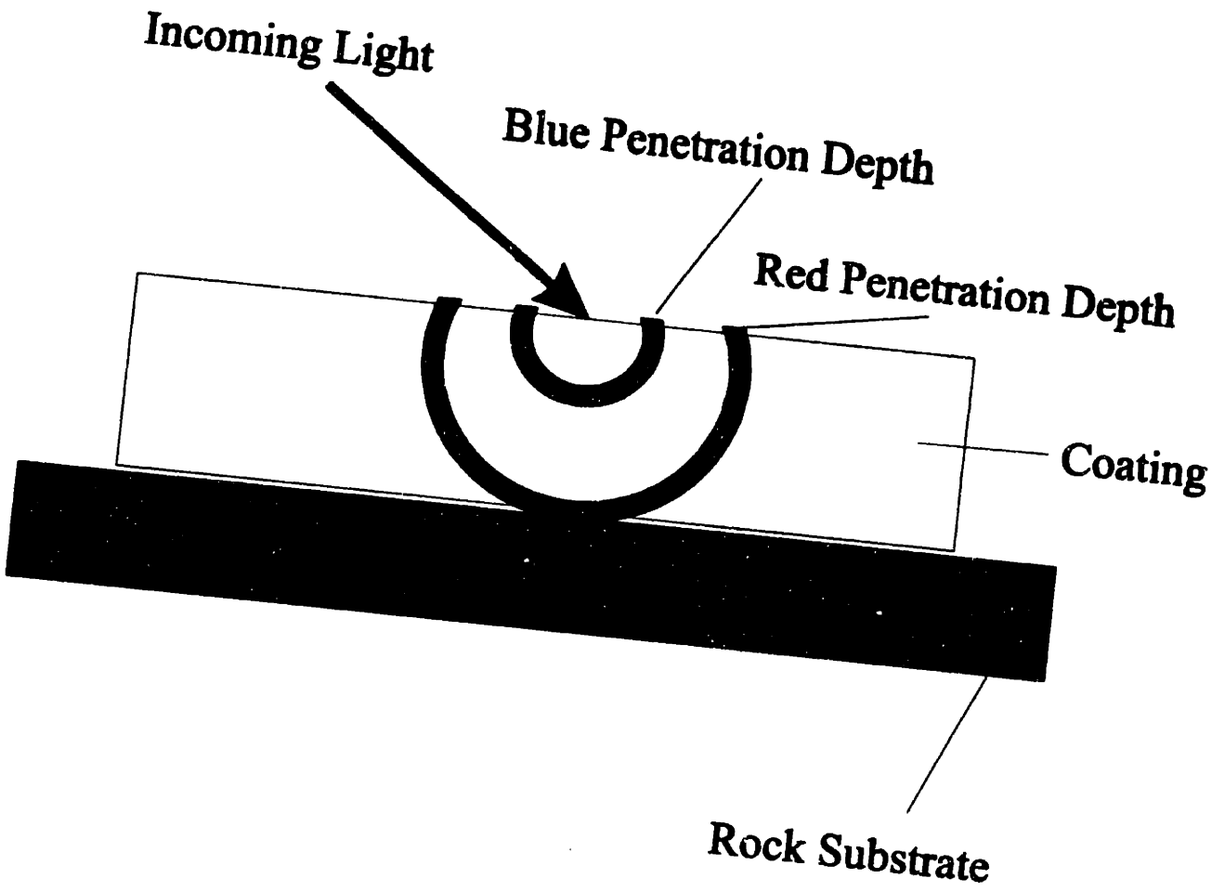

Figure 2.3 Schematic of a tape cast coating with light penetration depths indicated.

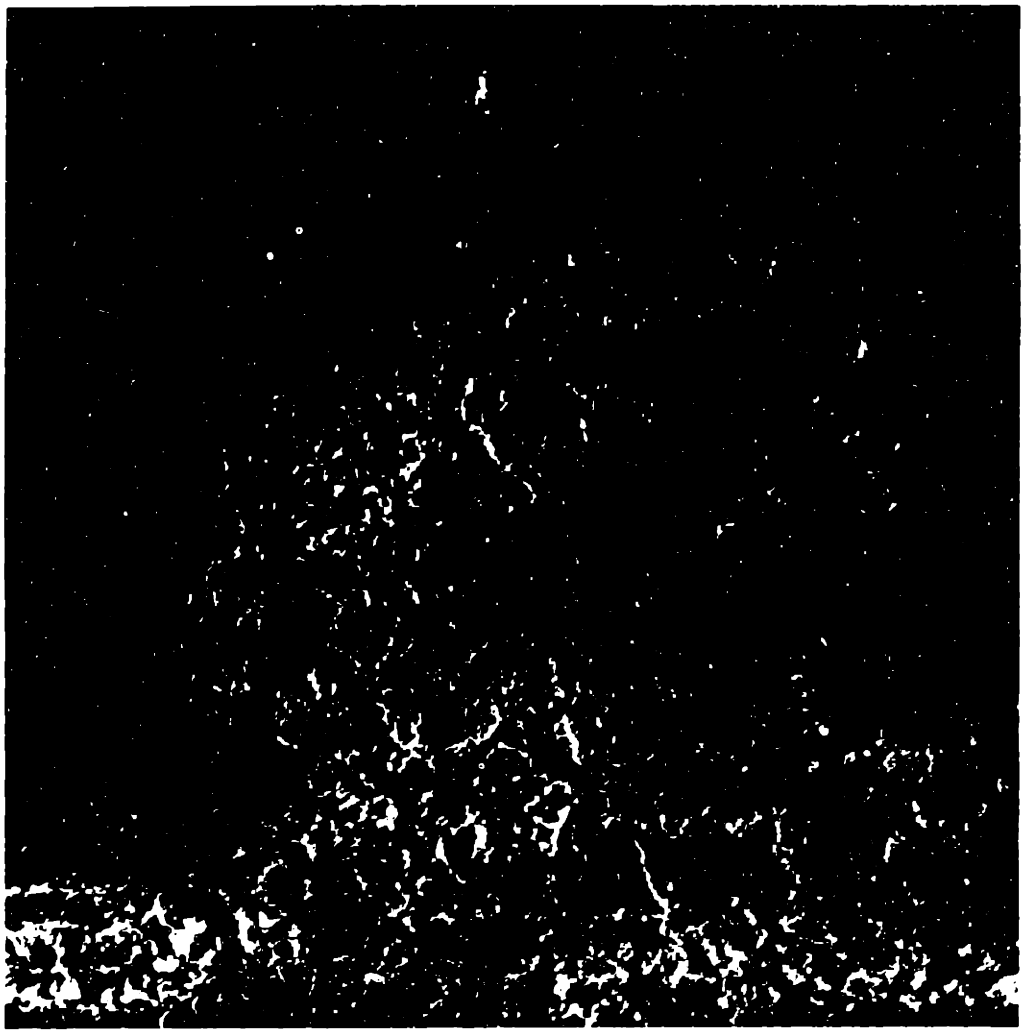

Figure 2.4 SEM micrograph of as received clay powder.

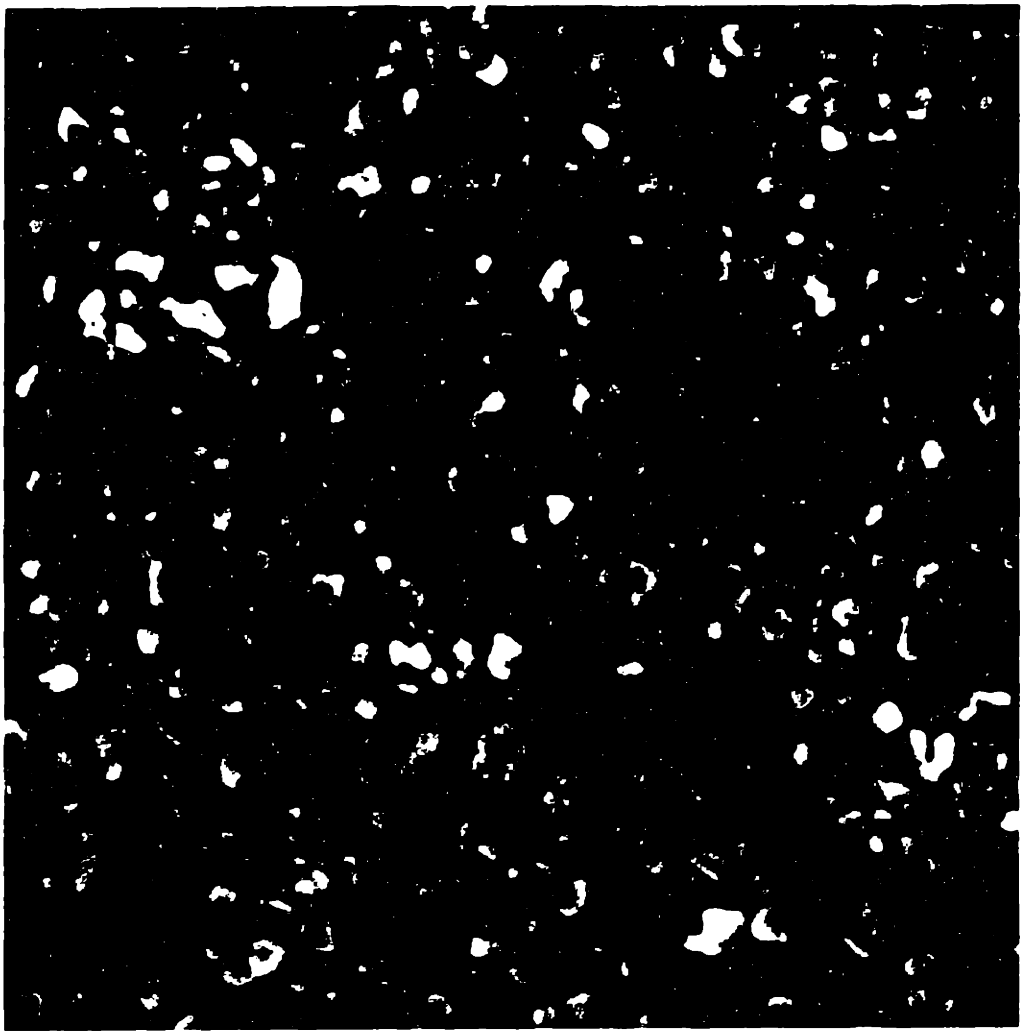

Figure 2.5 SEM micrograph of as received titania powder.

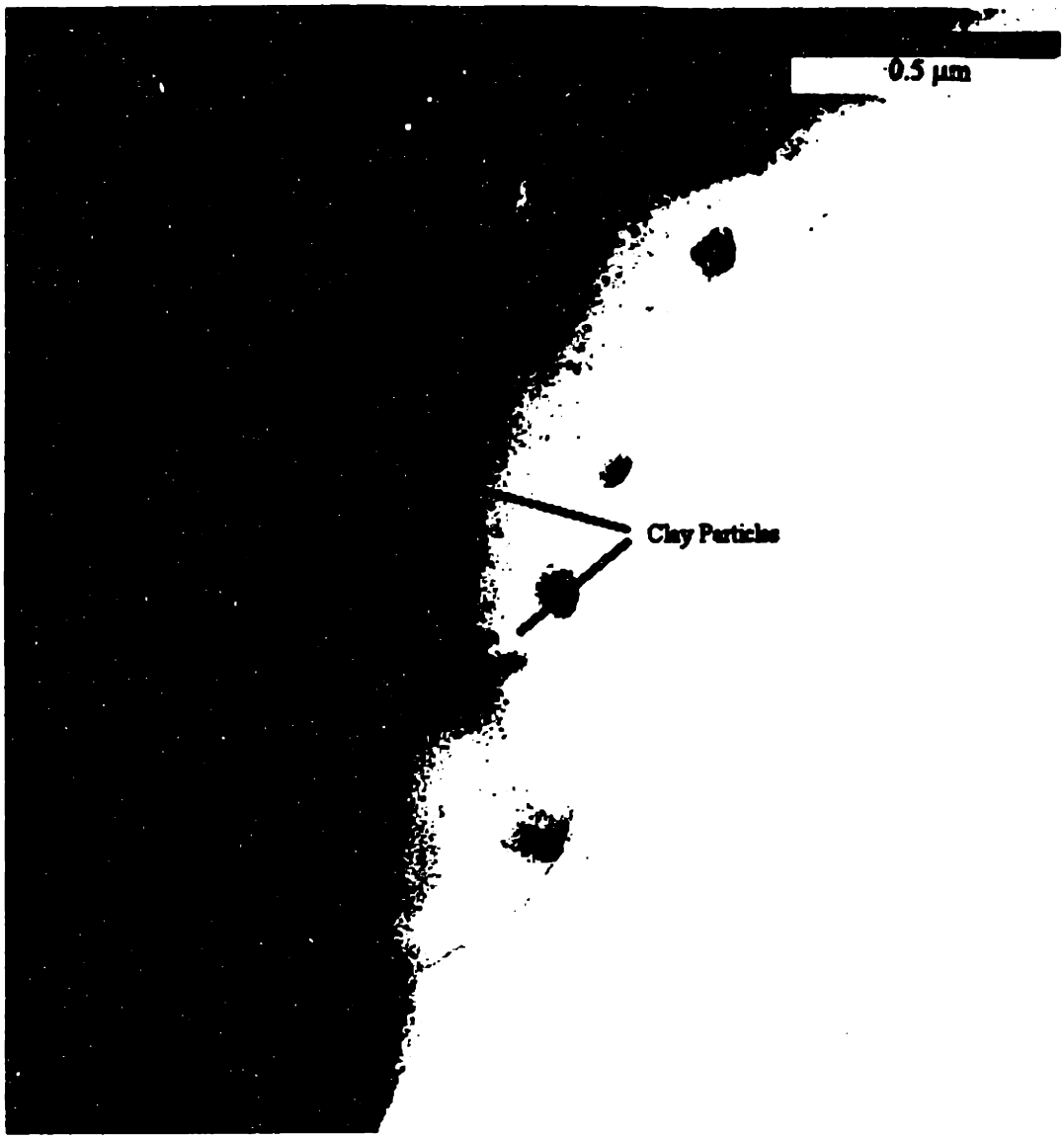

Figure 2.6 TEM micrograph of a silicate/ clay film.

been fired and was still water soluble.

The TEM micrograph (Figure 2.6) shows two clay particles in the silicate matrix. The particles show plate-like morphology common to clay powders and are 0.4-0.5 μm in length along the major axis. This is significantly smaller than the observed particle size in the as-received powder.

The titania did not show any significant size change when it was dispersed. Figure 2.7 is a TEM micrograph of a coating containing clay and titania in the silicate matrix. Preparation of the TEM sample was similar to the procedure outlined above. No clay particles are visible in the micrograph; however, a cluster of titania particles are visible. They are more equiaxed than the clay particles and are approximately 0.20-0.25 μm in size. The clustering of the titania particles and the absence of clay particles in the region suggests that the coating is not homogeneous and contains some segregation of clay and titania on scales on the order of 1-5 μm.

2.5 OBSERVATIONS

Figure 2.8 is a plot of Kubelka-Munk absorbance versus wavelength for one of the tape cast coatings. Several features of the plot are important. There are no absorption bands in the visible wavelengths, 400-800 nm, since the coating is white. The absorbance at the blue end of the spectrum is 0.065 Kubelka-Munk units and is slightly higher than the red absorbance of 0.055 Kubelka-Munk units, indicating that the coating would register as slightly red in colorimetric tests similar to those outlined in Section 2.2. The second feature of note is the strong absorption edge in the near UV wavelengths around 390 nm. This is characteristic of the titania used as the principal pigment in the coating. Comparison of scans with 0° and 8° sample orientations showed no measurable specular reflection. Thus the scattering was purely diffuse.

Figure 2.9 shows two plots of the diffuse spectrum of the uncoated polished rock sections. Figure 2.9 (a) is a plot of the diffuse and specular absorbance (8° sample orientation), and Figure 2.9 (b) shows the data for 0° orientation, which includes only the

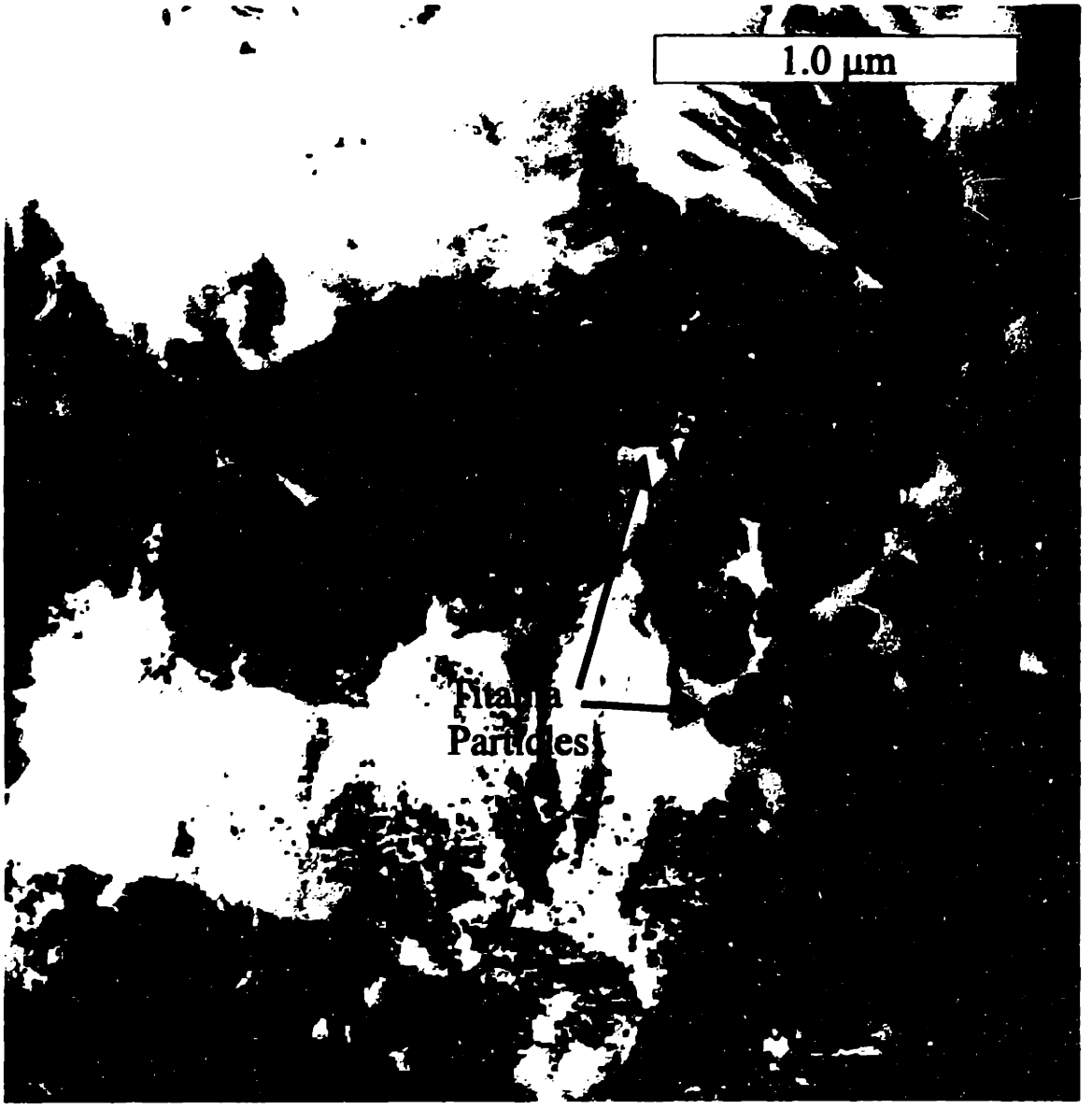

Figure 2.7 TEM micrograph of a silicate/ clay/ titania film.

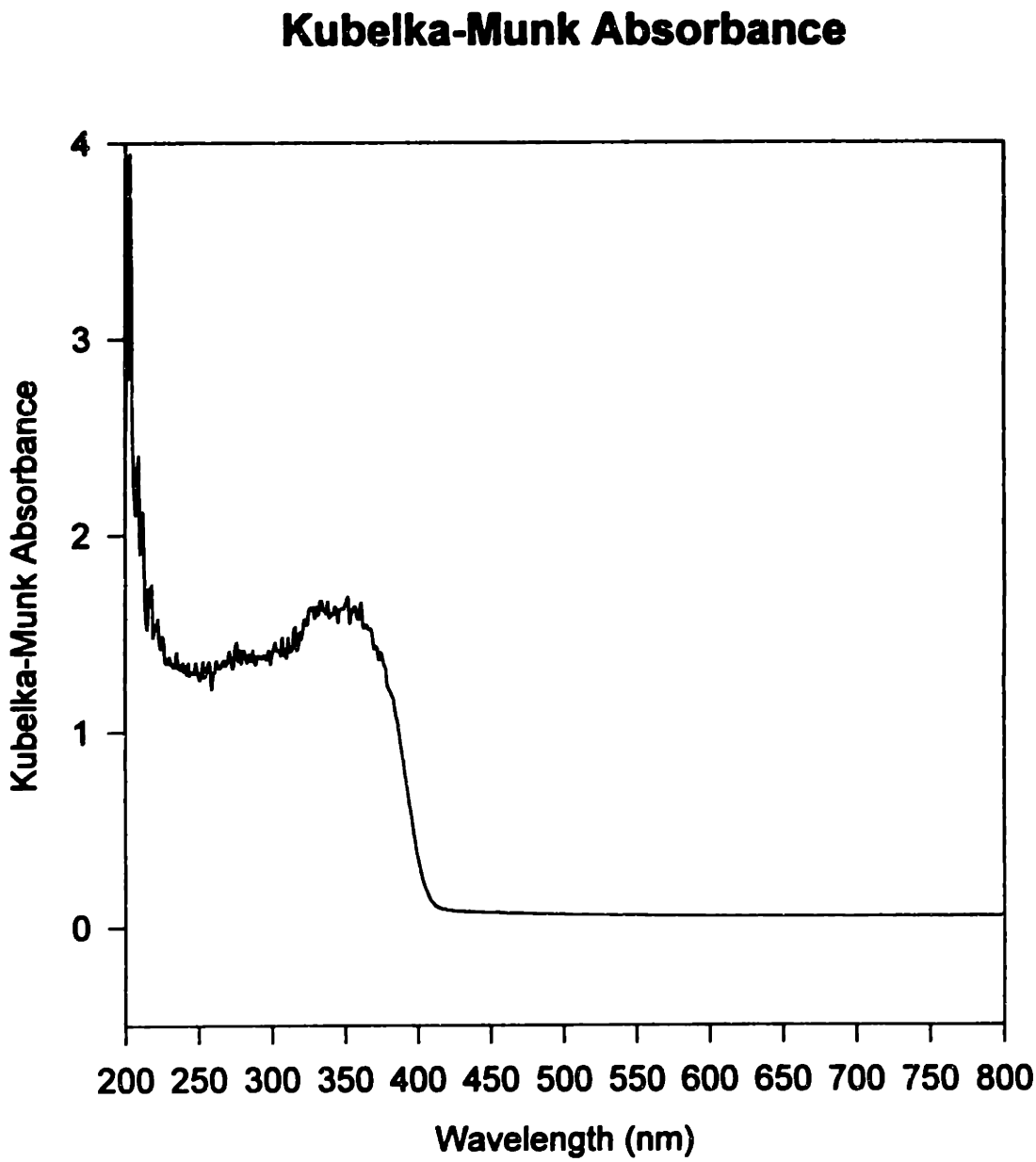

Figure 2.8 Plot of Kubelka-Munk absorbance vs. wavelength for tape cast coating 46A.

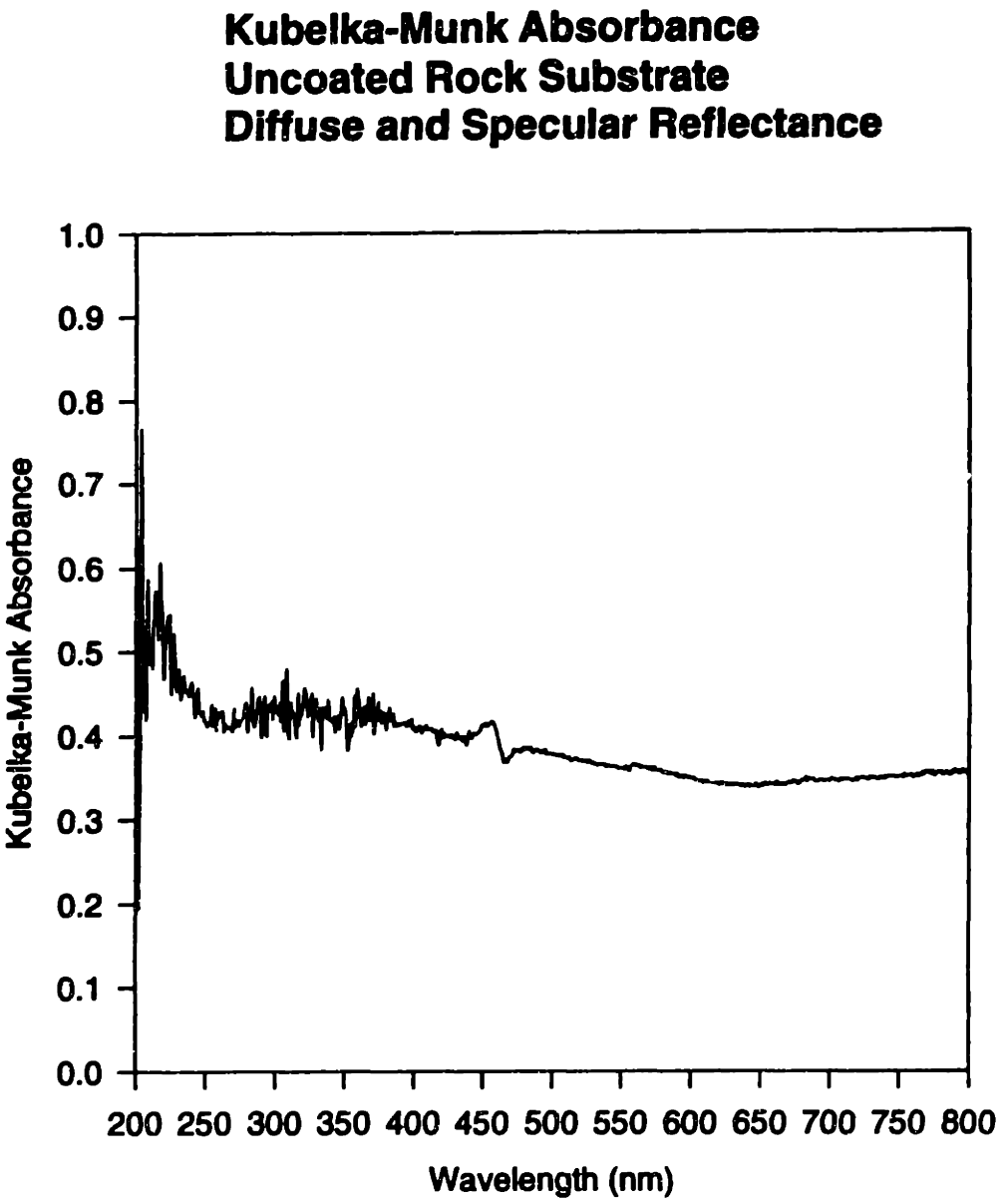

Figure 2.9 (a) Plot of Kubelka-Munk absorbance vs. wavelength for uncoated rock substrate: 8^0 sample orientation, diffuse and specular reflection.

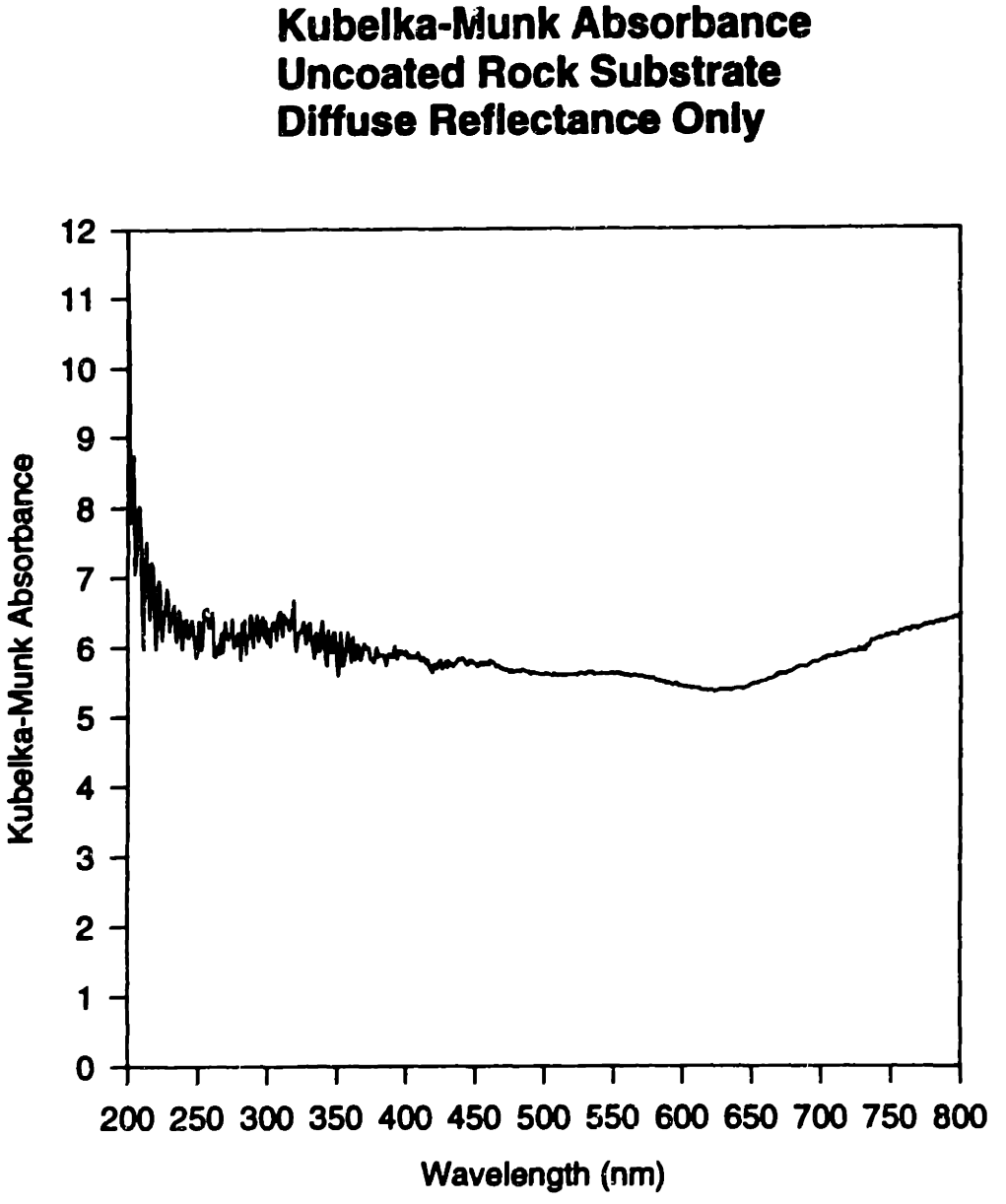

Figure 2.9 (b) Plot of Kubelka-Munk absorbance vs. wavelength for uncoated rock substrate: 0° sample orientation, diffuse scatter only.

diffuse scatter. The rock shows much larger visible absorption due to its dark color. The specular reflection is largely independent of wavelength, but the diffuse scatter shows enhanced absorption in the red end of the spectrum, from 650-800 nm, relative to the blue end of the spectrum.

Figure 2.10 presents the absorbance data for all six tape cast coatings with the spectrum of the uncoated rock substrate. The trend in the data shows that the coating absorbs more visible light and scatters less as thickness decreases. The correlation is shown in Figure 2.11 for two wavelengths: 500 nm (blue) and 800 nm (red). The data for zero thickness is taken from the diffuse spectrum of the uncoated rock substrate. The curves for both wavelengths are in the same relative position for thicknesses greater than 30 μm, indicating that the color of the coating remains constant. The absorbance increases slightly as the thickness decreases and the coating appears darker. This change would correspond to constant a^* and b^* and a decrease in L^* as thickness decreases on the $L^*a^*b^*$ scale.

The color does not remain constant at thicknesses below approximately 25 μm. The absorbance in the red wavelengths increases at a much faster rate with decreasing thickness. The thinner coatings appear more blue than the thicker coatings and L^*, a^* and b^* will all show a decrease with decreasing thickness.

The implication for the production process is that color consistency can be achieved for a^* and b^* with a coating thicker than 25 μm for this slurry formulation. A constant lightness, L^*, with thickness requires much thicker coatings, on the order of 60-70 μm, as indicated by the gradual change in absorbance in this thickness range.

Samples of roofing granules were mounted in epoxy, cross-sectioned and polished to determine coating thicknesses. Figure 2.12 shows a typical granule cross-section. It is apparent from the micrograph that the coating is not uniform across the surface of a granule. There are large variations in thickness, as well as gaps, where there is no detectable coating. Table 2.2 summarizes the thickness data for three different granule samples: A and B were produced in the same plant with different slurry formulations, while A and C were produced in different plants with the same slurry formulation. The data listed in the table are the average minimum and maximum coating thickness

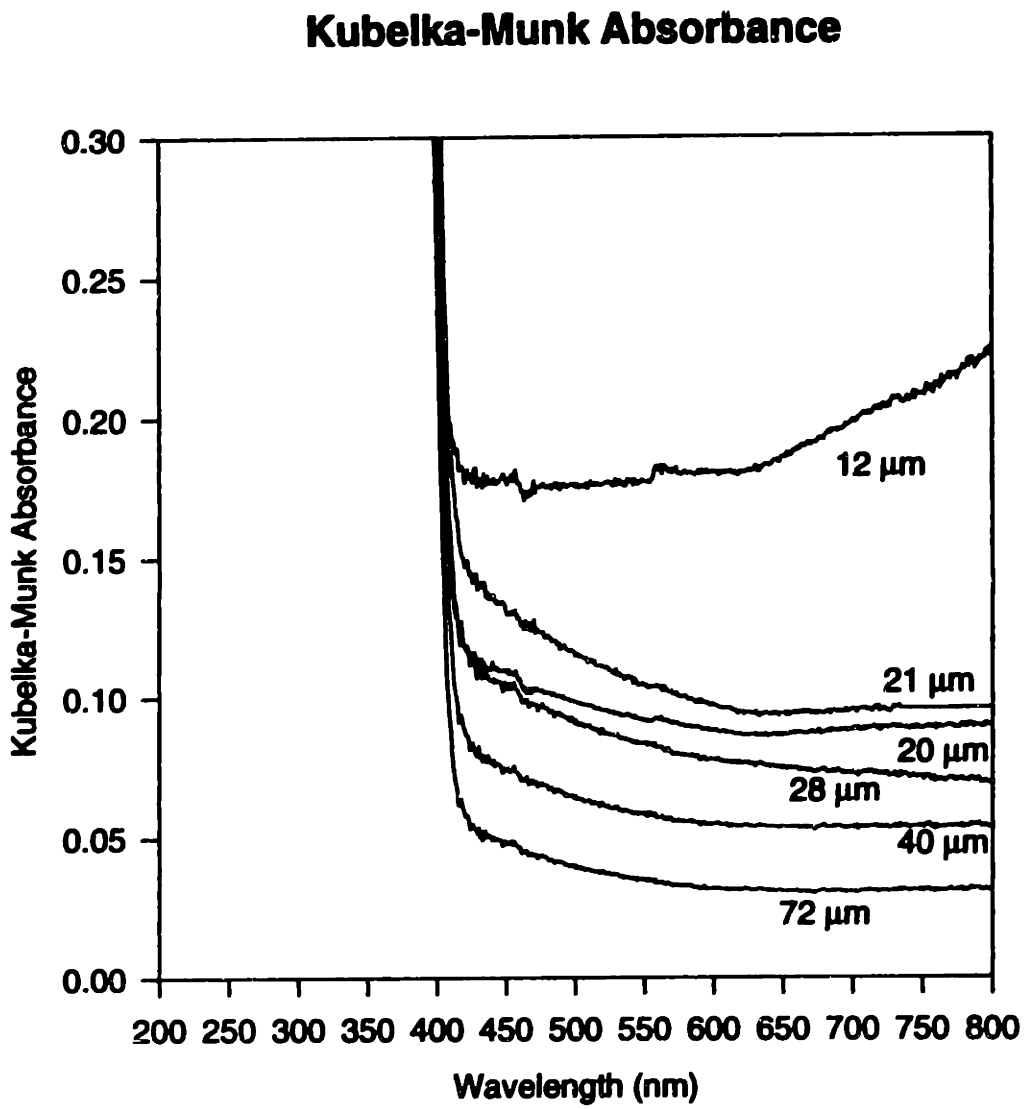

Figure 2.10 Plot of Kubelka-Munk absorbance vs. wavelength for all six tape cast coatings and the uncoated rock substrate.

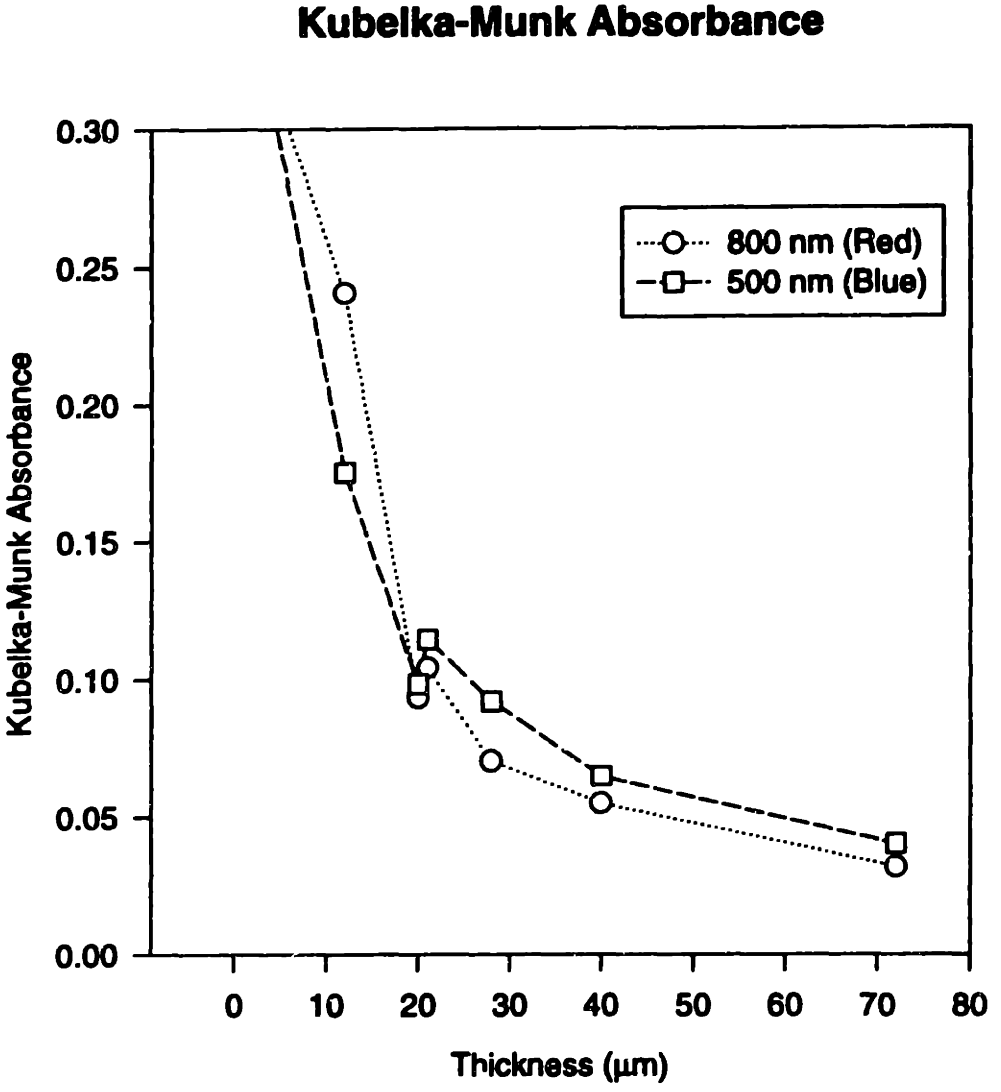

Figure 2.11 Plot of Kubelka-Munk absorbance vs. thickness for 500 and 800 nm.

(a)

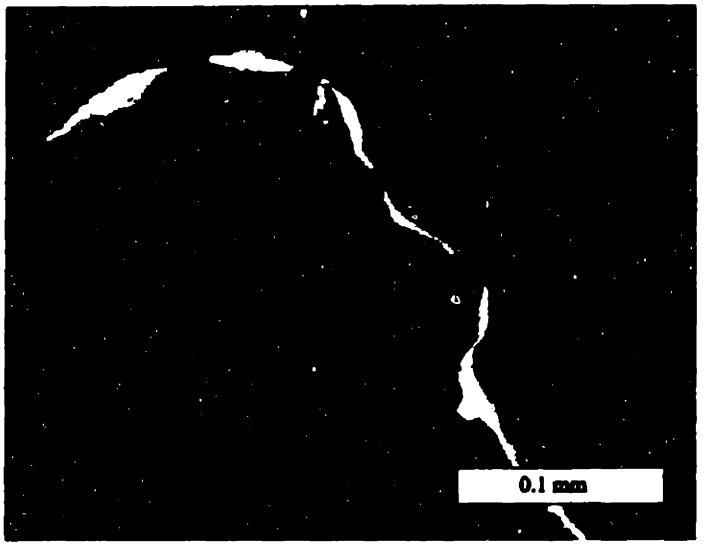

(b)

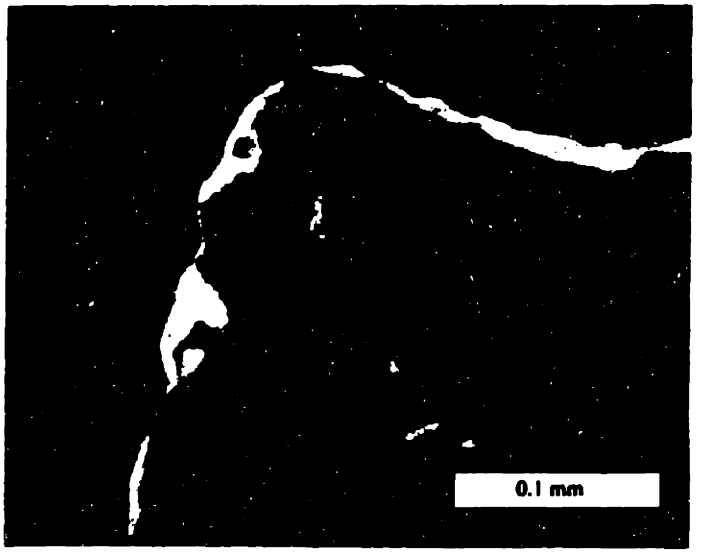

Figure 2.12 Optical micrographs of a polished cross-section of a roofing granule.

observed for a random sample of 10-12 granules. The gap length data is an average of the observed lengths of the gaps in the coating.

Table 2.2 Coating thicknesses measured from optical micrographs of roofing granule cross-sections.

Batch A

Minimum	17 μm
Maximum	128 μm
Gap Length	159 μm

Batch B - Same manufacturing plant as A, different slurry formulation.

Minimum	13 μm
Maximum	63 μm
Gap Length	145 μm

Batch C - Same slurry formulation as A, different manufacturing plant.

Minimum	16 μm
Maximum	112 μm
Gap Length	246 μm

These data indicate that the coating currently being applied to the granules is not conducive to color consistency. Coating thickness is below the 25 μm threshold in many places, and the coating is completely absent in some locations, allowing the rock to be visible. The coating is also much thicker than necessary in many other places, wasting coating material.

2.6 DISCUSSION

2.6.1 KUBELKA-MUNK ASSUMPTIONS

The tape-cast coatings conform to most but not all of the Kubelka-Munk assumptions discussed in Section 2.3. The number of scattering events for each incoming photon is high due to the thickness of the coating and the low absorbance of the titania in the visible wavelengths. The experimental data show that there is no detectable specular reflection from the coating. As discussed above, the coating is not homogeneous on the micron scale. It is homogeneous, however, on larger scales and the area illuminated by the sample beam was large enough to cancel out these effects. K and S are roughly constant throughout the medium. All the tape-cast samples were prepared from the same slurry and were dried under the same conditions so any segregation effects would be equal for all six samples.

The titania makes up approximately 40 vol.% of the coating and the clay another 45 vol.%. Nearly all of the coating is made up of the scattering centers and the particles sizes of these centers are on the order of 1-4% of the thickness of the coatings studied here, meeting the requirement that the scattering centers be of a size much smaller than the layer thickness. The high volume concentration of scattering centers also ensures that they are close together with very little of the matrix silicate in between. Light traveling between two particles between scattering events would have only a small chance of being absorbed.

The increase in absorption with decreasing thickness indicates that the coating is not optically "thick." Some absorption from the rock substrate is occurring, particularly for coatings with a thickness of less than 20 μm. However, this is the effect being measured so the restriction is not relevant to the experiment.

2.6.2 LIGHT PENETRATION INTO THE COATING

The particles sizes observed in the TEM micrographs produce a large number of scattering centers when cast into a coating 10-100 μm thick. Titania scatters more than the clay, since titania absorbs less light in the visible wavelengths. Incoming light hitting the top surface of the coating penetrates a short distance into the coating before striking a particle. Most of the light is diffusely scattered, some energy re-emerges from the coating, but most is scattered into the interior. This process is repeated as the photons strike other particles in the coating until they either emerge from the top of the coating or are absorbed.

The statistics of this Rayleigh scattering depend on the wavelength of the light striking the surface. Shorter wavelengths are scattered more randomly than the longer wavelengths, which tend to be scattered less and travel in straighter lines. The longer red wavelengths will penetrate farther into the coating than the shorter blue wavelengths. Red intensity will be higher than blue intensity at a specific depth in the coating. Inversely, a specific red intensity contour will be deeper in the coating that the same blue intensity contour. The equation for penetration of radiation into an absorbing medium is:

$$I_x = I_0 e^{-\mu(\lambda)x} \tag{2.2}$$

where I_O is the incident intensity, I_x is the intensity of the radiation at a distance x into the material, and $\mu(\lambda)$ is the linear absorption coefficient. This coefficient is a function of the material through which the light is passing and the wavelength of the light. The silicate coatings have a higher absorption coefficient in the blue wavelengths than the red. Significant penetration of the red light occurs at thicknesses of 25 μm. Significant penetration of the blue light occurs at about 20 μm. Using these data, the absorption coefficients can be calculated, assuming that the ratio I_x/I_O is the same for red at 25 μm as for blue at 20 μm and equal to e^{-1}. The calculated values are μ_{red}=4.0 x 10^4 m^{-1} and μ_{blue}=5.0 x 10^4 m^{-1}.

This difference causes the color to change in the thinner coatings as the intensity of light penetrating to the rock surface becomes a significant fraction of the total light striking the upper surface. The effect is further amplified by the higher absorbtivity of the rock in the red end of the spectrum.

2.7 CONCLUSIONS

This experimental protocol can be repeated for any slurry formulation and provides a research tool to determine optimal coating thickness to achieve the desired color roofing granule. This 25 μm threshold is the smaller of the two thicknesses determined from the spectroscopy data. It is also thinner than much of the observed coating in the optical micrographs of the cross-sections. Thus, the current process puts a large excess of coating material on the granules, probably in an effort to hide the effects of the gaps and thin areas of the coating.

Color coefficients, a^* and b^*, remain constant for 25 μm and 70 μm films, but L^* decreases as the film gets thinner. Process improvements that produce a more uniform coating thickness across the surface of each granule and between granules would eliminate this source of variability. The goal of the remainder of this thesis is to make improvements in the bulk coating process that will lead to a more uniform coating.

CHAPTER 3
SLURRY SPREADING

3.1 INTRODUCTION

A typical process for producing roofing granules is diagrammed in Figure 3.1. Raw rock is quarried, crushed, and sieved to the proper size. A typical size range is 1.0-2.5 mm in diameter. The crushed rock is heated in a rotary kiln preheater using a gas fired burner in the input air stream. Current production practices heat the rock well above the desired coating temperature. Water is applied to the rock in order to cool it to the proper temperature after transferring the heated rock to the drum mixer. This is followed by application of the slurry. A series of flights in the mixer lifts the coated material to ensure maximum contact with the air flowing through the mixer. This air stream, which dries the coating, is not heated; the heat in the rocks is sufficient to dry the coating. The coated granules emerging from the mixer are not completely dry, but the coating no longer transfers between granules. The firing kiln completes the drying and induces chemical changes that make the coating insoluble in water. Final post-firing procedures such as oiling to prevent dust formation are often applied.

The processes occurring in the mixer are complex and have been separated into two unit operations for study. The first operation is the spreading of the slurry over the surface of the granules and is the subject of this chapter. The second operation, the initial drying of the coating in the mixer, will be treated in a later chapter.

The initial interaction of the slurry with heated rock can be broken down into three types of interaction. The first interaction that occurs is the contact between slurry and an individual rock surface. The second interaction is the slurry penetration into the rock bed. The final interaction results when coated granules transfer slurry to uncoated rocks.

The slurry interaction with the rock surface was studied by observing drops of slurry

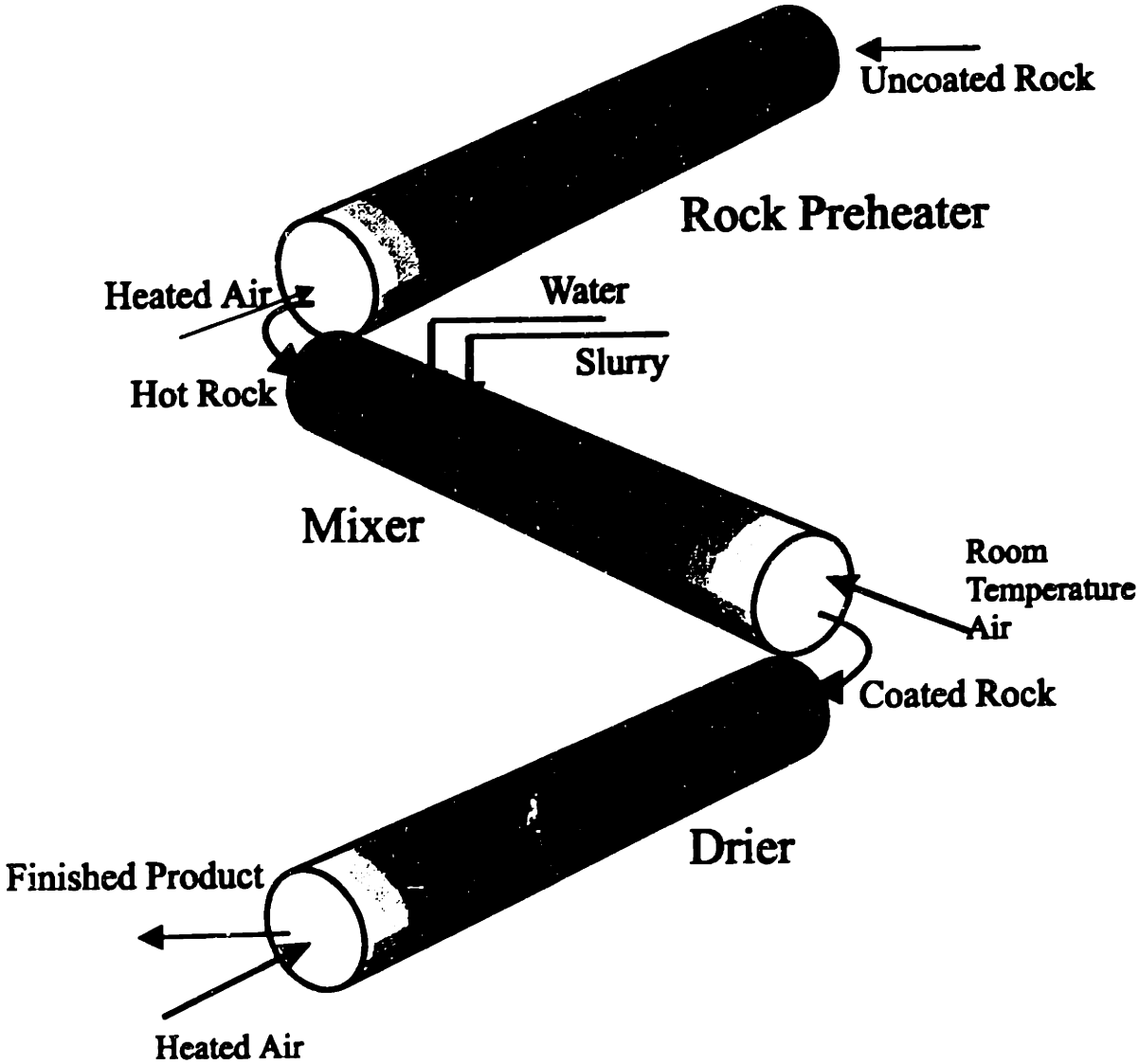

Figure 3.1 Schematic of a typical roofing granule production process.

during impact on rock substrates. The surface temperature and conditions of the rock were varied to determine how the coating parameters such as water feed rate and preheated rock temperature affect the slurry spreading, and the results are presented in Section 3.2. The third section of this chapter examines the slurry penetration into the porous rock bed. The penetration depth into the bed is correlated with the same parameters examined in Section 3.2. These experiments show that the initial interaction between the slurry and the rock bed causes a layer of the bed to be saturated with slurry, while other parts of the bed remain uncoated. Later tumbling in the mixer must distribute the coating material. This section also presents a theoretical model of slurry penetration into the mixer bed based on a derivation similar to a Kozeny model. The model describes the qualitative behavior of the slurry interaction with the mixer bed and provides a quantitative relationship between the penetration depth into the mixer bed and the yield stress of the slurry. The results of this model are compared with experimental data.

The kinetics of slurry transfer between granules is examined in a laboratory and pilot plant experiments in Section 3.4. Both experiments show that slurry spreading in the drum mixer occurs over a narrow section, which is relatively distinct from the region of the mixer where drying occurs. The next section describes the results of production scale experiments to implement specific process changes based on this research. The final section presents the major conclusions of this chapter.

3.2 SLURRY INTERACTION WITH THE ROCK SURFACE

The initial interaction between the slurry and the rock granules depends on the surface properties of the rock. The applied slurry can either spread easily over the rock surface or it can bead up, depending on the surface conditions. Two principal process variables can affect the initial slurry/ rock interaction: rock preheat temperature and water application rate. Water is applied to the rock in the mixer, just prior to slurry application, see Figure 3.1. Studies performed by a manufacturer had shown that the application of a

small amount of water improved coated granule quality.[14] The assumption was that the cooling effect of the water slowed the drying process and produced a better coating.

3.2.1 EXPERIMENTAL PROCEDURES

The assumption that application of water to the heated rock was improving coating quality by lowering the rock temperature was tested by heating polished sections of rock to the coating temperature and applying drops of slurry to them. Sections of polished rock were obtained, similar to those used in the tape casting experiments in Chapter 2. The slurry used was based on a formula and materials provided by a manufacturer.[14]

The rock was heated on a hot plate to a specified temperature, ranging from 80-130 °C, which includes a typical range used in the manufacturing process. Temperature was measured by a thermocouple on the rock surface. Water was applied with a cotton swab in some experiments, the rock was left dry in others. Slurry was applied from above by a pipette, and the drops falling on the surface were recorded with a video camera. See Figure 3.2 for a diagram of the experimental setup.

A second experiment was performed to separate the effects of temperature and surface condition of the rock. Water was applied to a small area of the rock surface, leaving a boundary between wet and dry areas. Ten to fifteen seconds were allowed to elapse to allow thermal equilibration between the wet and dry regions, and slurry was dropped onto the boundary area. The drops of slurry experienced two different rock surfaces: wet and dry. The slurry contact angle could be measured from still photographs captured from the video footage of the experiment, see Figure 3.3. This contact angle is not a true contact angle based on surface energy. It is limited, instead, by the competition between flow and drying during the spreading process.

Rock sections were precoated with a silicate slurry at room temperature. This coating was dried in air and then fired to 200 °C. The precoated rock was then heated to the preheat temperatures used in the above experiments.

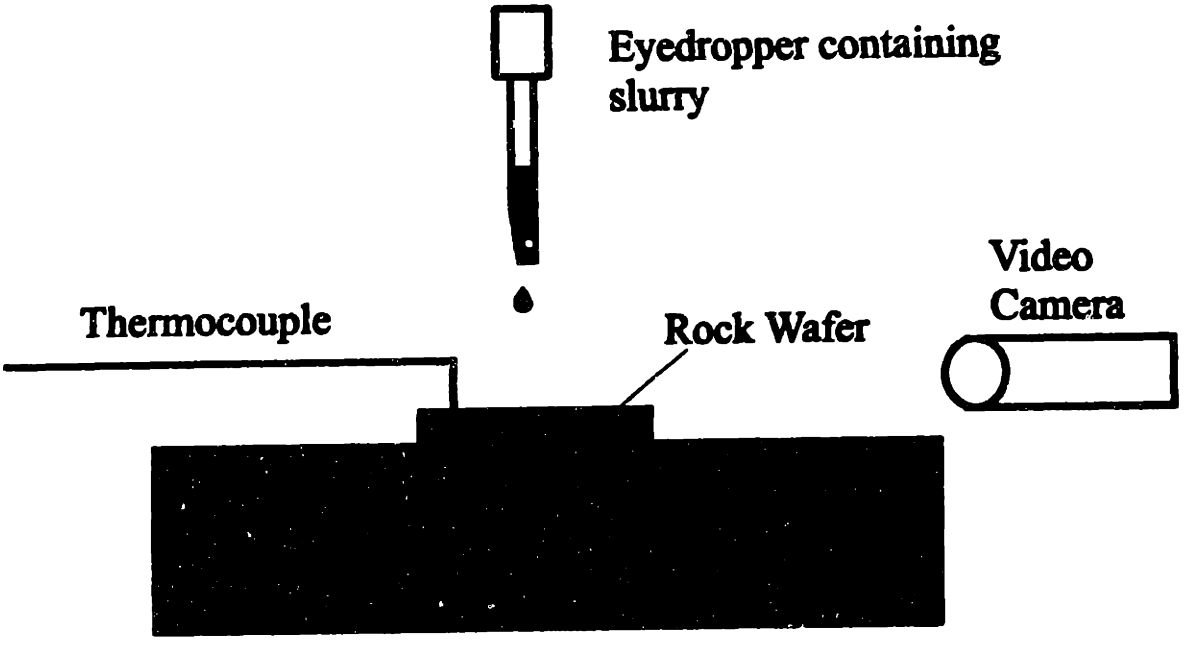

Figure 3.2 Experimental setup for slurry/ rock contact angle experiments.

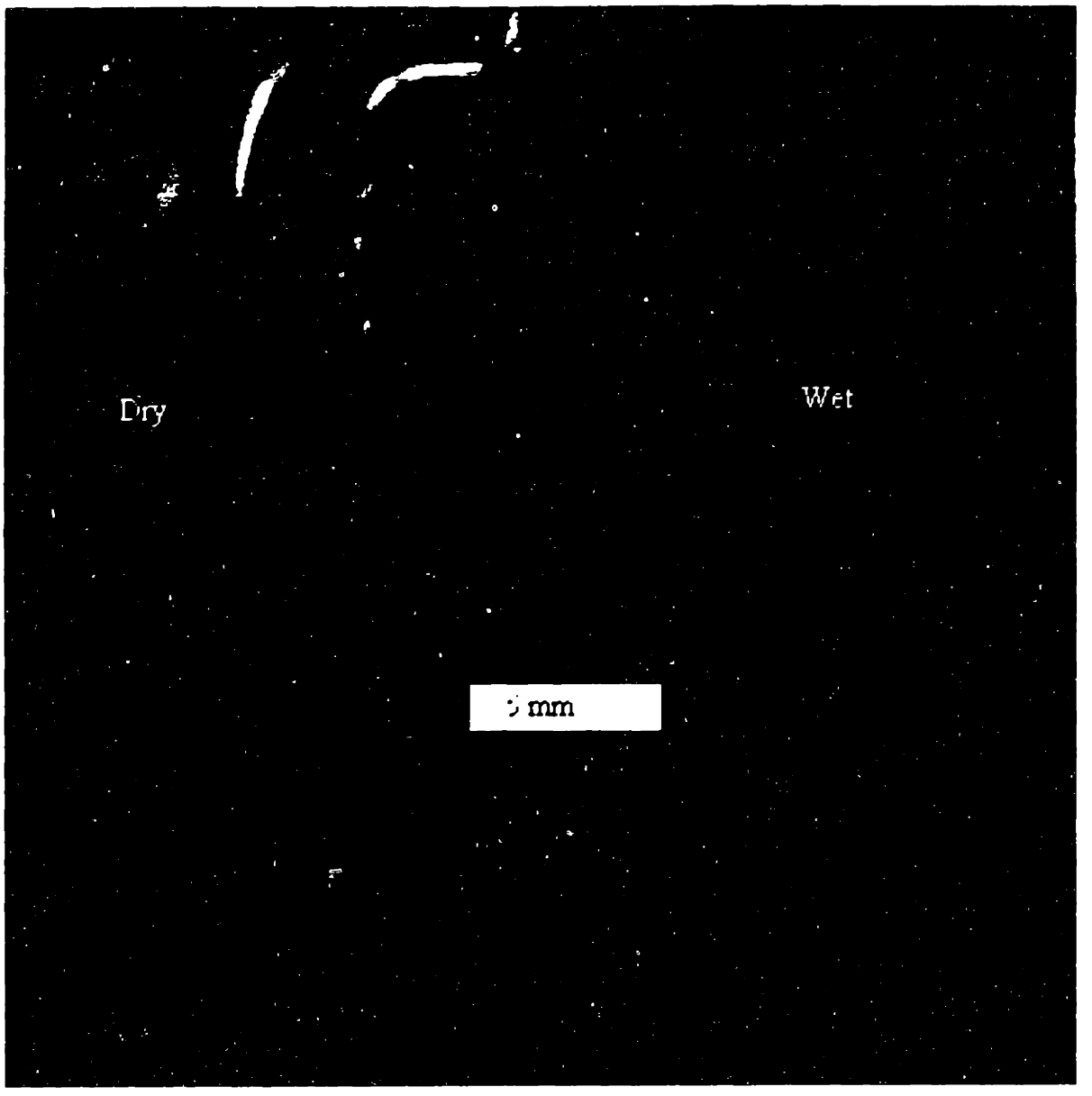

Figure 3.3 Slurry interaction with a heated rock section. The rock has been prewet with a small amount of water on the right side of the figure. The left side of the rock was dry.

3.2.2 OBSERVATIONS

The slurry dried very quickly upon hitting dry rock and did not spread as the preheat temperature was increased. The slurry formed beads with large contact angles. Small amounts of water applied to the rock prior to the slurry drops promoted spreading of the slurry before drying became significant. This effect was more difficult to achieve at higher preheat temperatures because the water dried from the surface of the rock very quickly.

Contact angles were measured from the video tape frames and are shown in Table 3.1. The angles measured show a large difference in spreadability of the slurry between wet and dry rock. This is entirely due to the change in surface energy caused by the presence of water, and is separate from the temperature effects noted above.

Table 3.1 Contact Angles measured for various rock surface treatments.

	Dry	Wet
Slurry on Rock	131°	51°
Slurry on precoat	82°	45°
Precoat on Room Temp. Rock	120°	-

Contact angle data for the rock precoated with dried silicate, presented in Table 3.1, show that the dry precoat surface promotes better spreading than the dry rock surface. However, the wet precoat surface and the wet rock surface had nearly identical contact angles, showing that the presence of water on the surface to be coated is a controlling parameter in the initial spreading of the slurry, and is somewhat independent of the material to be coated.

3.2.3 DISCUSSION

The effect of the smaller contact angle on coating quality is indirect. It has been shown above than the initial contact of the slurry with the hot rock is a competition between

spreading and drying. A smaller contact angle will speed spreading and the coating will become more uniform before drying prevents further slurry motion. Large contact angles, such as those observed for dry rock, cause the slurry to bead up on the rock surface and dry without spreading. This leads to large variations in coating thickness, which were observed in actual granules, e.g. the micrographs in Figure 2.12. Ensuring that the water applied to the rock prior to slurry application forms a film over the rock surface should improve the quality of the coating produced by the process.

These experiments show that slurry spreading over wet rock surfaces is relatively insensitive to temperature effects; however, the rock preheat temperature does play a role in the coating quality by affecting the drying rate of the water film on the rock surface. Lower preheating temperatures will reduce the drying rate of the water film.

There are two basic conclusions from these studies. The first conclusion is that wet rock surface get coated easily, and the second is that wet slurry does transfer easily to dry rock surfaces and dried slurry surfaces. The implications of these conclusions will be discussed further in Section 3.4.

3.3 SLURRY PENETRATION INTO THE MIXER BED

3.3.1 MIXER BED DEPTH MODEL

Slurry injected into the mixer strikes the top surface of the rock bed and is drawn into the pores between the rock granules. Several possibilities arise, depending on the rheological properties of the slurry. The slurry can quickly penetrate though the bed and come into contact with all the granules, or it can pool on top of the bed and spread out to cover the top surface without interacting at all with the granules in the bed interior. A partial penetration of the bed is also possible. An experimental model of the slurry interaction with the bed of granules was developed to characterize the behavior expected in a production mixer.

Figure 3.4 is a schematic cross section of the mixer. The point O is the axis of rotation

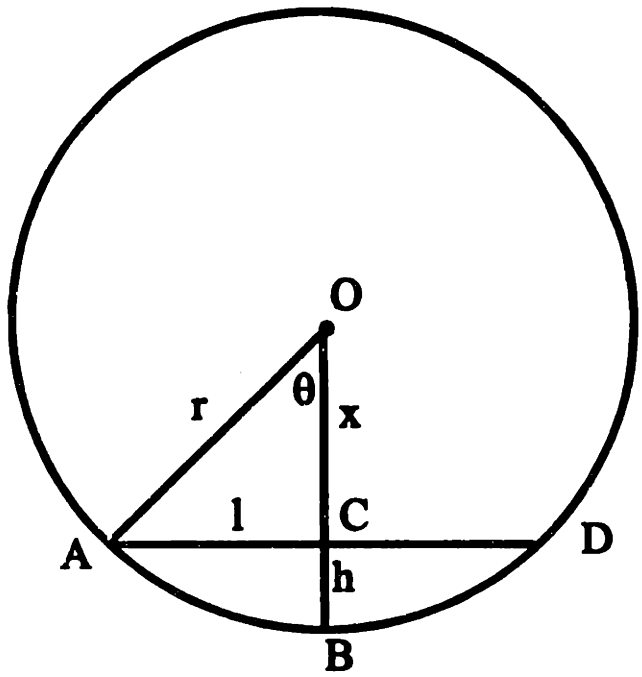

Figure 3.4 Schematic cross-section of the mixer used in the derivation of the bed depth.

of the mixer, and the line AD is the top surface of the bed. BC is the center of the bed, where the maximum depth, h, occurs. The half angle subtended by the bed is θ radians, and the radius of the mixer is r. The area of the sector AOB is:

$$area_{AOB} = \pi r^2 \frac{\theta}{2\pi} \tag{3.1}$$

and the area of triangle AOC is:

$$area_{AOC} = \frac{1}{2} xL = \frac{1}{2} r^2 \cos\theta \sin\theta \tag{3.2}$$

where L is half the width of the top surface of the bed and x is the distance between the axis of the mixer and the bed surface:

$$x = r - h \tag{3.3}$$

The difference between the two areas is ABC, which is half the cross-sectional area of the bed and can be estimated from the operating parameters of the mixer.

$$area_{ABC} = area_{AOB} - area_{AOC} = \frac{1}{2} r^2 (\theta - \cos\theta \sin\theta) \tag{3.4}$$

This equation can be solved iteratively for θ based on the values of r and $area_{ABC}$. For the mixer studied in this thesis, θ was computed to be 0.676 radians (38.7°). The bed depth is related to this angle by the equation:

$$\cos\theta = \frac{x}{r} = \frac{r - h}{r} \tag{3.5}$$

solving for h gives:

$$h = r(1 - \cos\theta) \tag{3.6}$$

The value of h computed for this study was 40.1 cm. This is the estimated depth of the rock bed in the bottom of the mixer near the slurry application point. There are no flights in the section of the mixer immediately following the slurry application point (see Figure 3.5 for a diagram of the mixer), so none of the mass of the bed is lifted upward.

3.3.2 EXPERIMENTAL PROCEDURES

A bed of the calculated depth was constructed in a glass tube; see Figure 3.6. The entire bed was heated using electrical resistance heating tape wrapped around the outside of the tube. Thermocouples were placed in two locations: near the upper surface of the bed, and near the base of the bed. Power delivered to the heating tape and the wrapping of the coils was adjusted to heat the bed uniformly to the coating temperature of 130 °C. Measured amounts of water and slurry were applied to the hot rock with a syringe. The volume of water and slurry were calculated from application rates from the industrial process scaled according to the ratio of width of the bed in the mixer to the width of the bed in the glass tube.

The experiment was videotaped and the temperature readings from the thermocouples were recorded. Several observations, applicable to all the runs, can be made. The dramatic cooling effect of the water can be noted from the plot of temperature versus time in Figure 3.7. This cooling was only observed for the upper thermocouple; the temperature of the rock registered at the bottom of the rock bed was unaffected in all runs. The second observation was that the penetration of the slurry into the bed was always a very small distance, 5-15% of the overall bed depth.

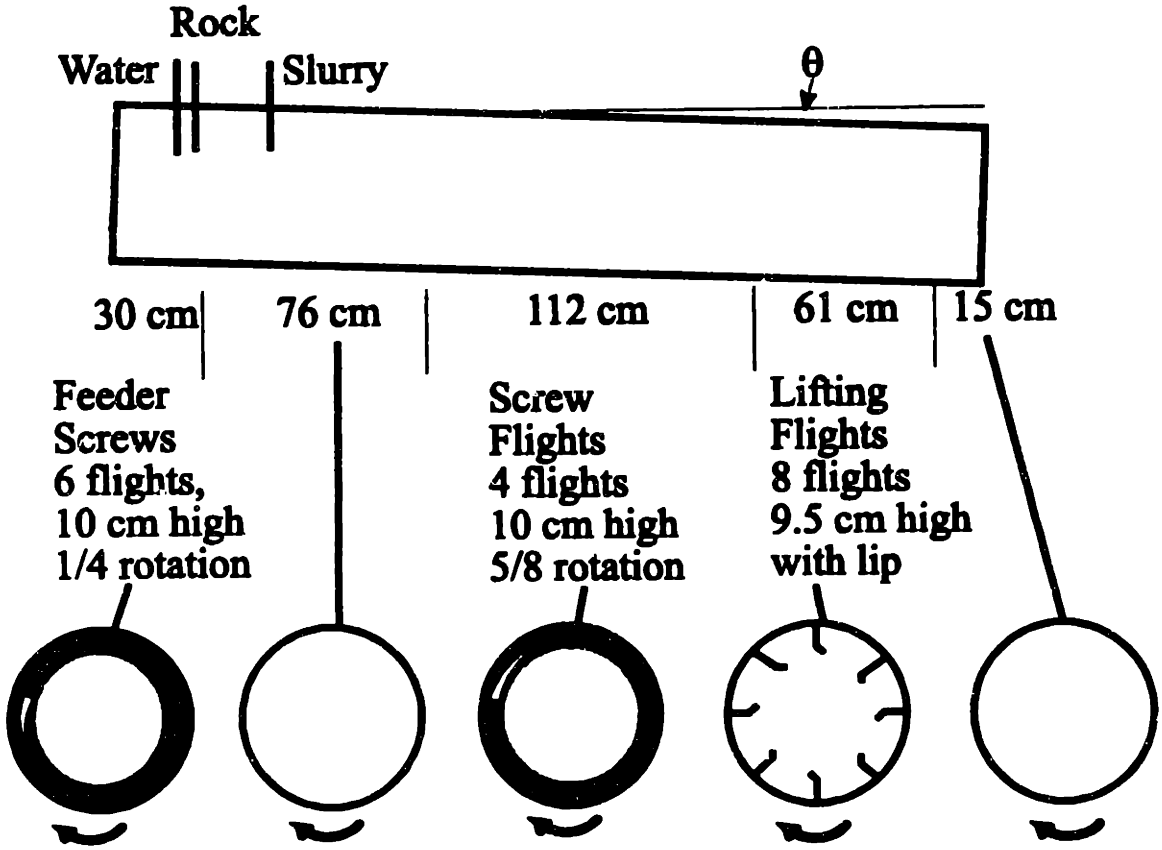

Figure 3.5 Schematic of the arrangement of flights in the mixer. Downward tilt of the mixer has been exaggerated for clarity.

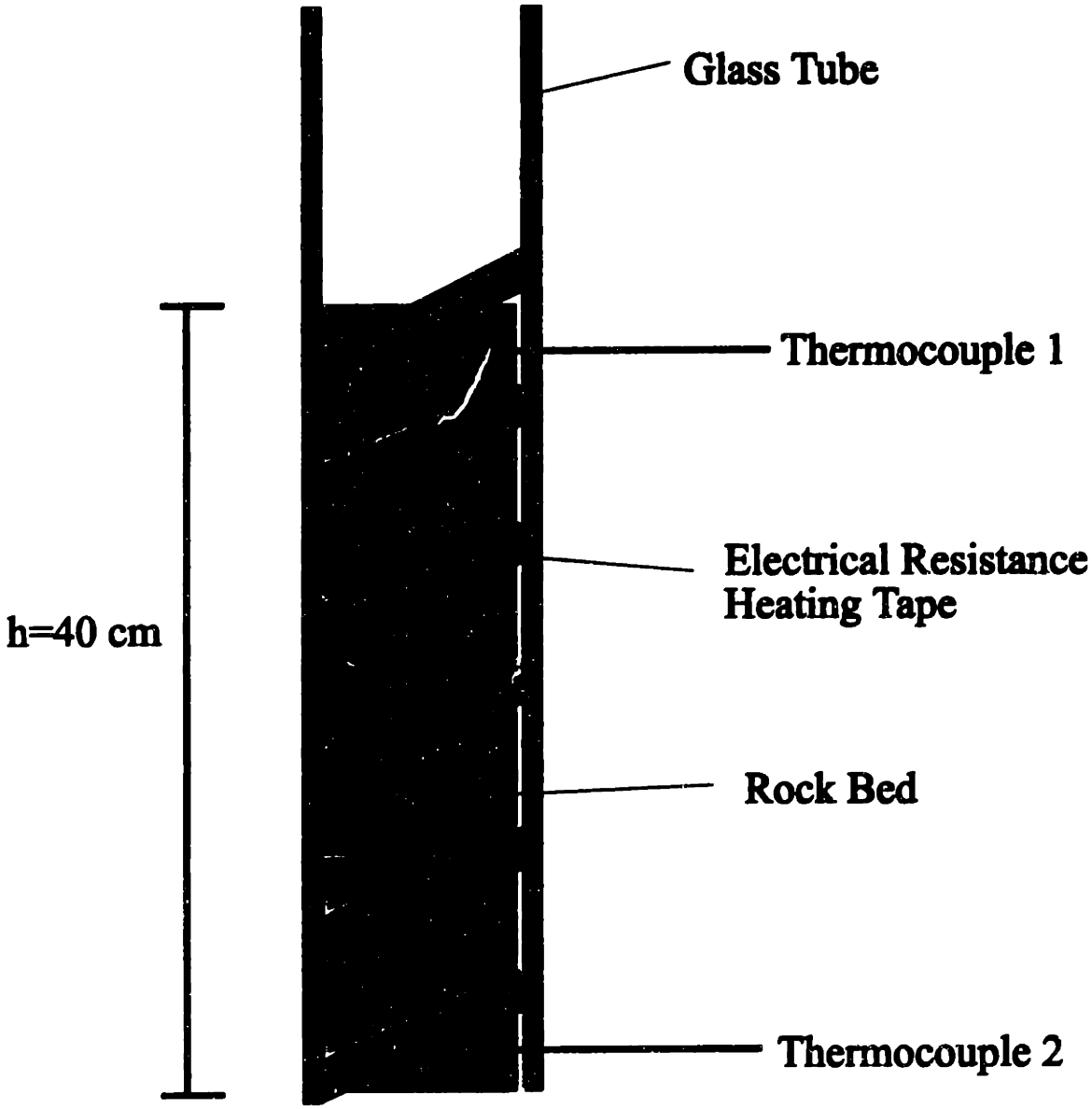

Figure 3.6 Schematic of the mixer bed penetration experiment.

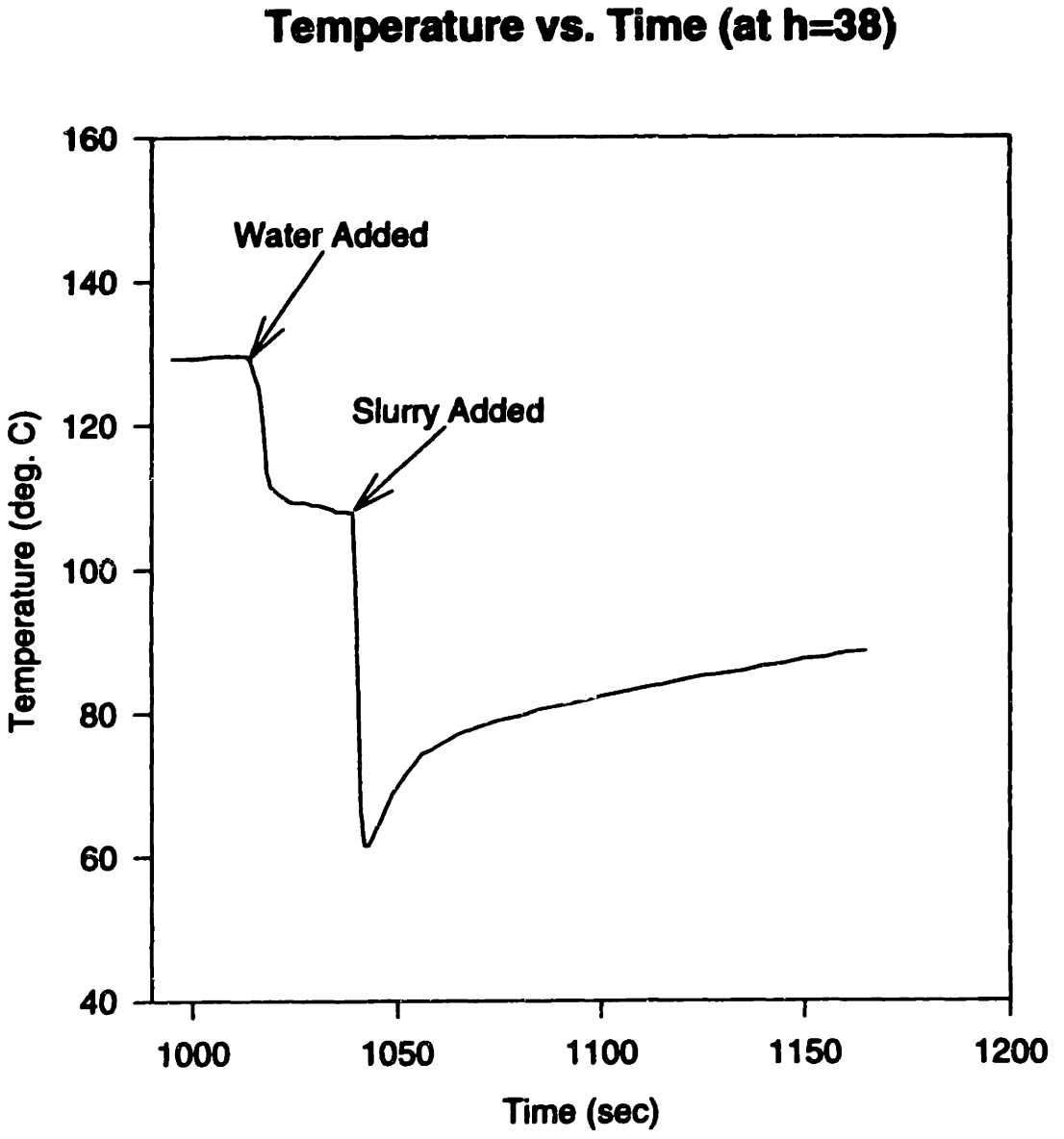

Figure 3.7 Typical temperature vs. time plot for the penetration depth experiments.

3.3.3 OBERVATIONS

The penetration depth was recorded for various conditions and the results are summarized in Table 3.2. The presence of water on the rock prior to slurry application again shows a dramatic effect. Comparing runs 1 and 2, the prewet rock had a penetration depth 3.5 times greater than the dry rock. Lower coating temperatures increased the penetration depth as well (compare runs 2 and 3), but did not have as large an effect. Run 3 was performed without water and started from a rock temperature similar to the temperature of the rock in run 1 after the water was applied.

Table 3.2 Summary of penetration depth experiments.

Run	Rock Temperature (°C)	Water	Penetration Depth (cm)
1	130	No	2.0
2	90	Yes	7.0
3	90	No	2.5

Other experiments were performed with the penetration depth apparatus using slurries with different amounts of clay. These slurries exhibited different rheological properties as shown in Figure 3.8. All of the slurries are highly shear thinning and showed a yield stress which varied with the clay content as shown in Figure 3.9. Each slurry was tested in the penetration depth experiment. The rock was preheated to 130 °C and the slurry was applied. No water was used in these experiments. The penetration depth was recorded once the slurry stopped moving. The penetration depth was greater than the depth of the bed in the apparatus in the case of the pure silicate slurry (0 wt.% clay). Figure 3.10 is a plot of the penetration depths recorded, as well as the time required for the slurry to reach the indicated depth.

Figure 3.11 is a log-log plot of penetration depth versus yield stress. Two data sets are represented, corresponding to two different initial rock temperatures, 25 °C and 130 °C. The data for 130 °C appears to follow a straight line. The data for 25 °C appears to follow a line of similar slope, but with a higher intercept.

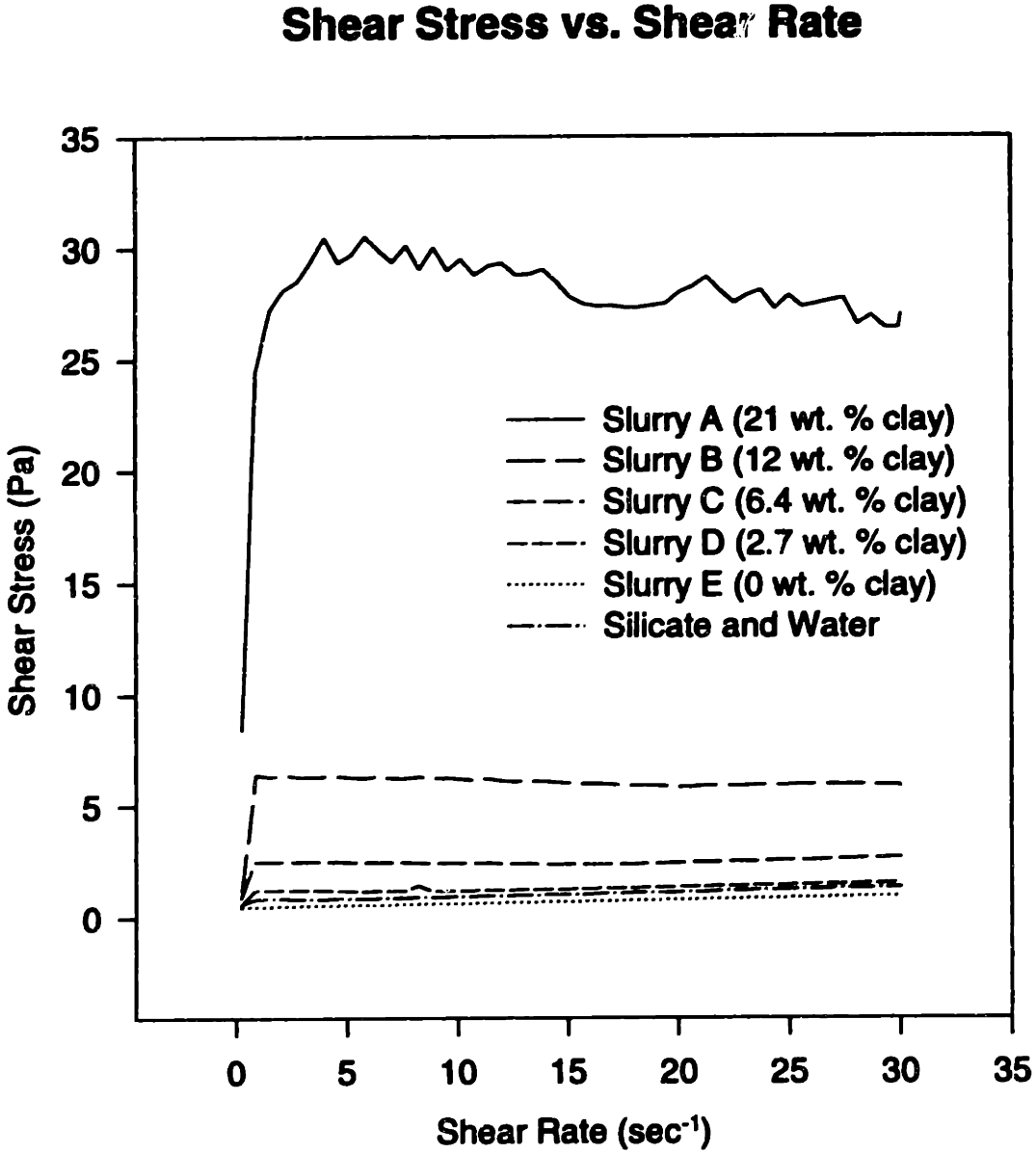

Figure 3.8 Plot of shear stress vs. shear rate for the slurries used in the penetration depth experiment.

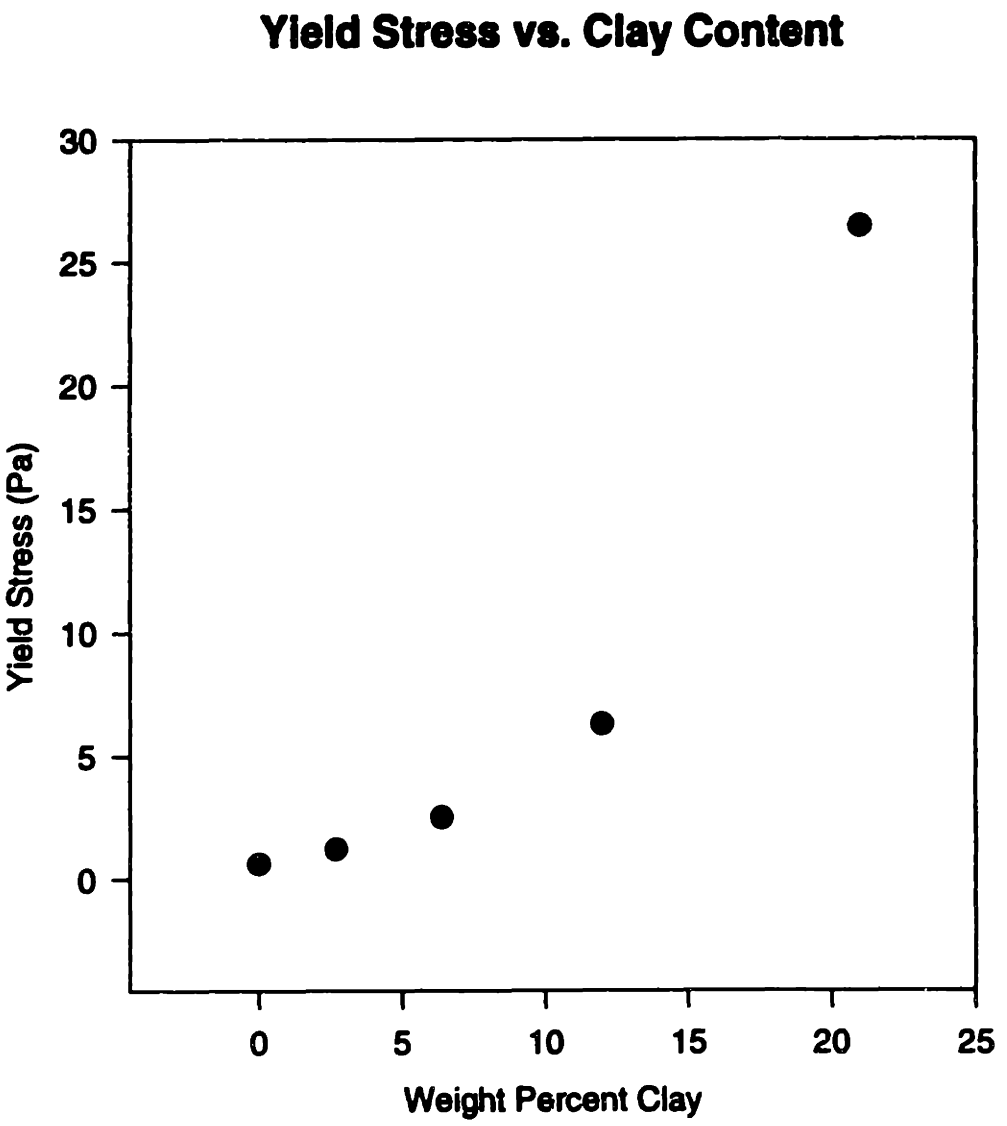

Figure 3.9 Plot of yield stress vs. clay content.

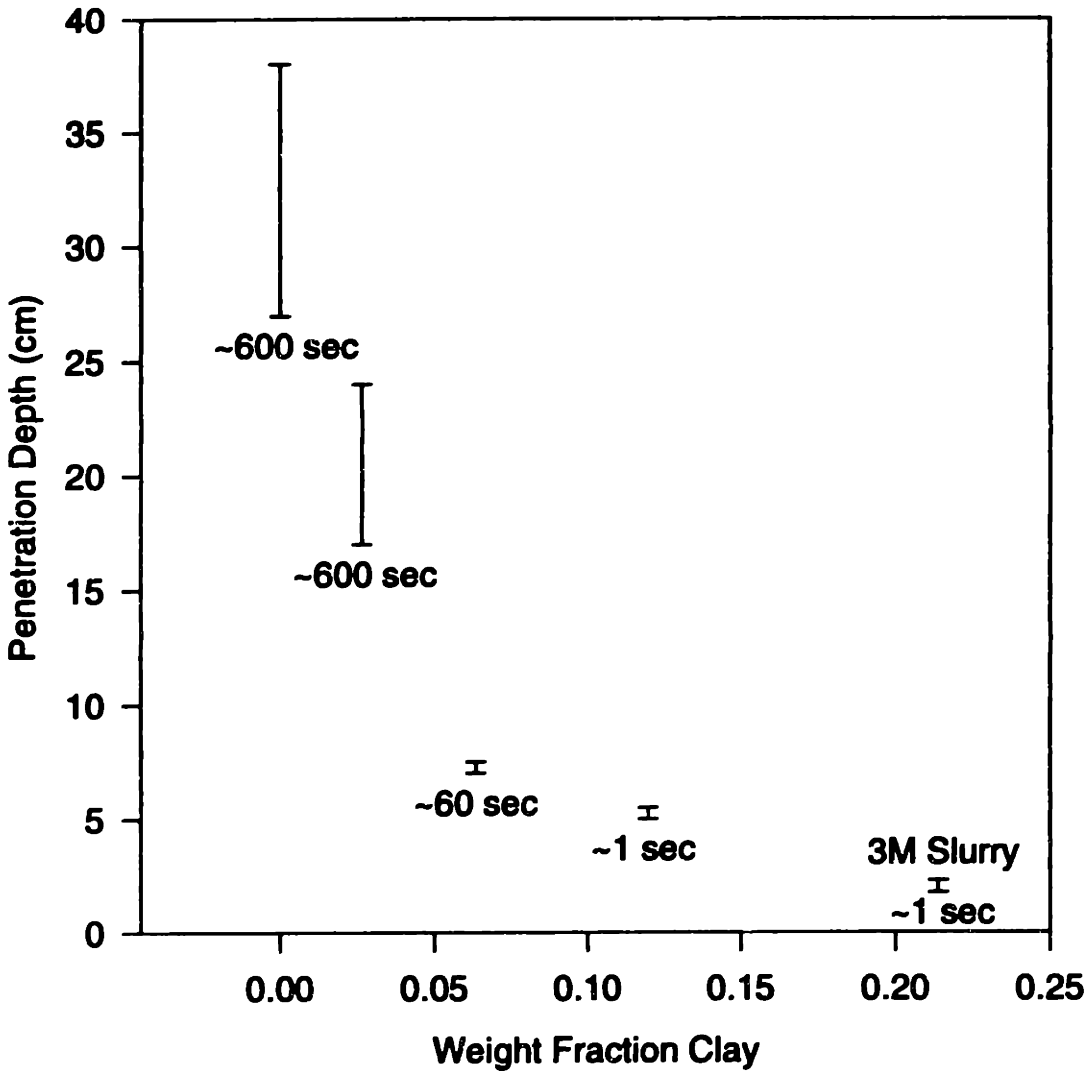

Figure 3.10 Plot of penetration depth vs. clay content of the slurry.

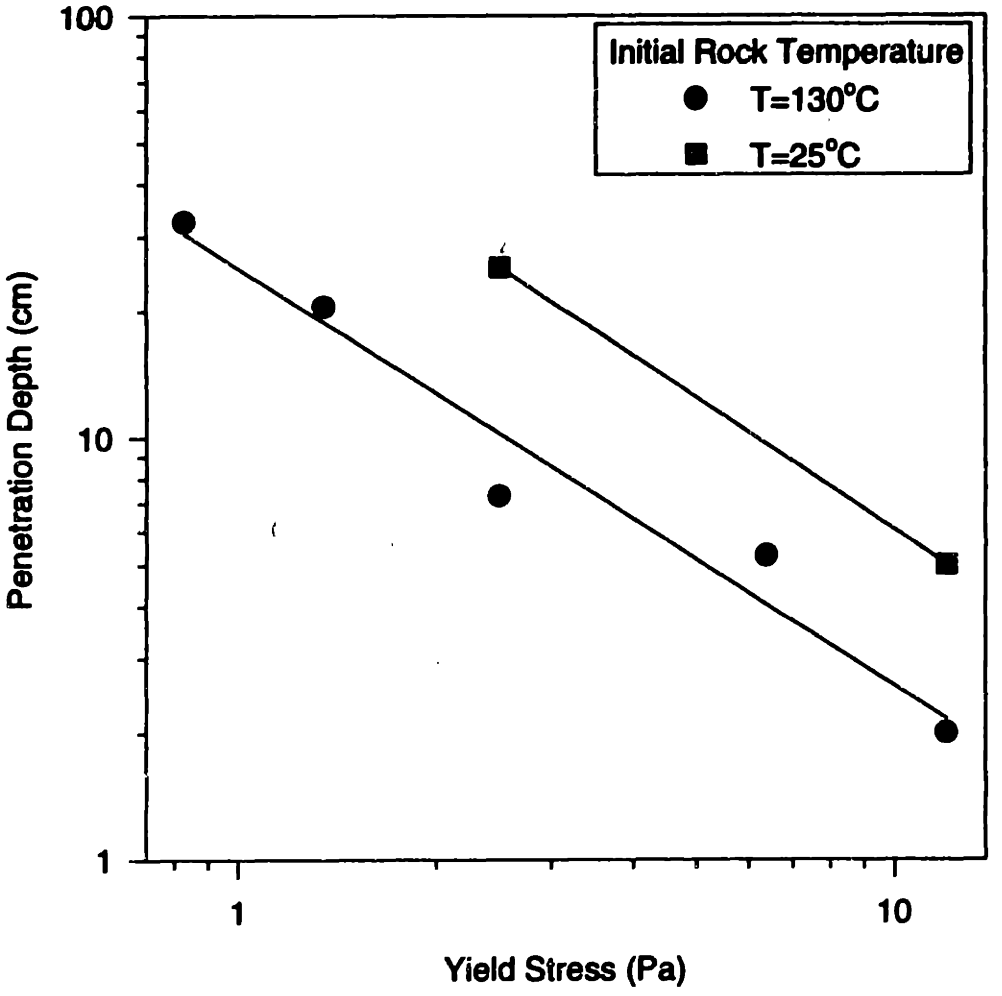

Figure 3.11 Log-log plot of penetration depth vs. yield stress. The slopes for the two rock temperatures are: -0.98 for 130 °C and -1.02 for 25 °C.

The data were fitted to the equation:

$$P.D. = A\tau_y^B \tag{3.7}$$

where *P.D.* is the penetration depth in cm, τ_y is the yield stress in Pascals, and *A* and *B* are the fit parameters. The results of the fit are listed in Table 3.3. These results will be compared with a theoretical model of the slurry infiltration process in the next section.

Table 3.3 Penetration depth versus yield stress fit parameters

Penetration Depth = $A\tau^B$

	A	B
Experimental	25.3	-0.98
Model (Section 3.3.4)	29.0	-1.00

3.3.4 DISCUSSION

The penetration depth data further reinforce the conclusions of Section 3.2; the presence of water on the rock prior to slurry application causes the slurry to better wet the rock, which leads to better coatings. Temperature is a secondary effect, since it controls the time that the prewet water will exist on the surface of the rock.

The small penetration depth leads to the conclusion that the slurry pools on top of the mixer bed rather than penetrating into it, resulting in three layers. A layer of pure slurry sits on top of a layer of rock bed saturated with slurry, and a layer of rock what has not yet contacted the slurry (see Figure 3.12). The tumbling action of the mixer must redistribute the slurry to all the rock. This conclusion is reinforced by studies that show that application of the slurry by spraying through a nozzle rather than the usual open ended pipe produces little or no change in coating quality.[14]

The process of a shear-thinning slurry infiltration into the porous bed of rock was modeled with a derivation based on a Kozeny model. Kozeny modeled a porous powder

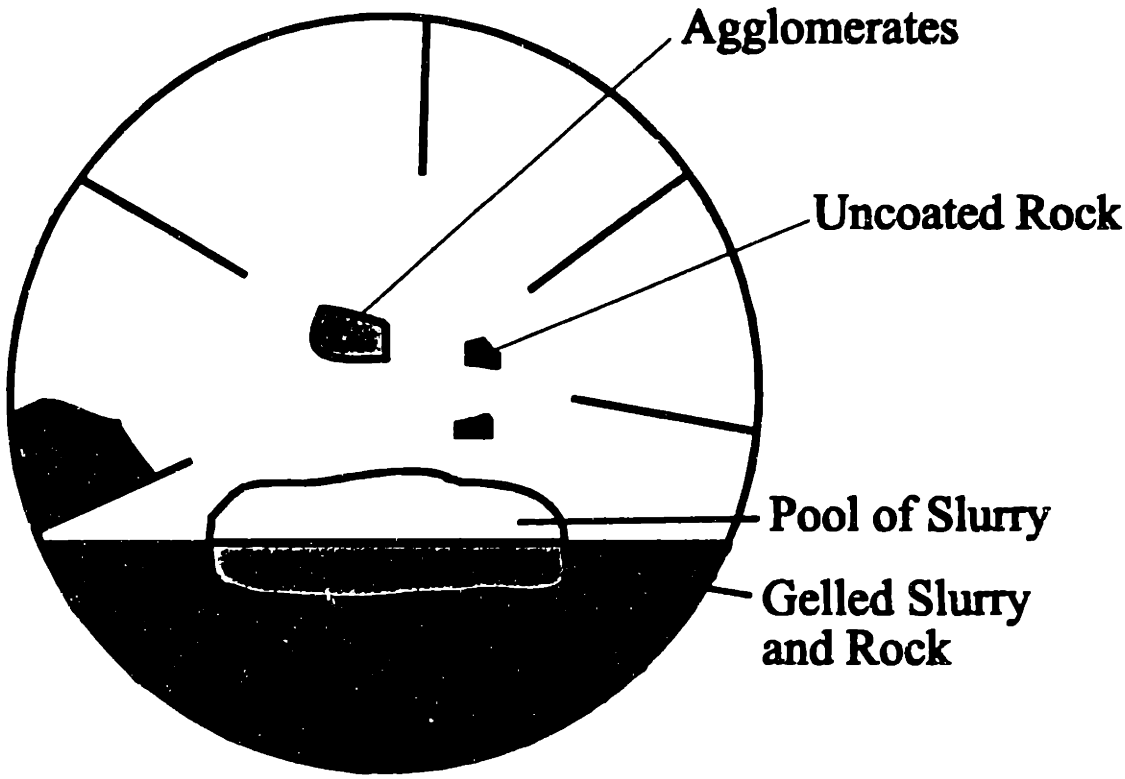

Figure 3.12 Schematic diagram of the layered structure formed during slurry penetration into the mixer bed.

bed as a bundle of parallel open tubes representing the porosity.[25] Figure 3.13 (a) shows a schematic of the slurry in the rock bed and Figure 3.13 (b) is a schematic of the tube bundle model. A single tube in the bed is shown in Figure 3.14. The pool of slurry on top of the bed applies a hydrostatic pressure equal to ρgy, where ρ is the density of the slurry, g is the acceleration of gravity, and y is the height of the slurry head. This pressure acts over the cross-sectional area of the pore, creating a force that drives slurry into the pore:

$$F = \pi a^2 \rho g y \tag{3.8}$$

where a is the radius of the pore. The walls of the tube oppose this force, generating a shear stress in the slurry that has penetrated the pore:

$$\tau = \frac{\pi a^2 \rho g y}{2\pi a z} \tag{3.9}$$

where z is the distance the slurry has penetrated. Assuming the pool of slurry does not change in height significantly, the shear stress in the tube drops as it is distributed over a larger area of the tube wall. There is a critical distance z_y, at which the shear stress in the tube is equal to the yield stress of the slurry, τ_y. The slurry will not penetrate any further into the tube because the shear in the tube is not enough to overcome the slurry's yield stress.

$$\tau_y = \frac{\pi a^2 \rho g y}{2\pi a z_y} \tag{3.10}$$

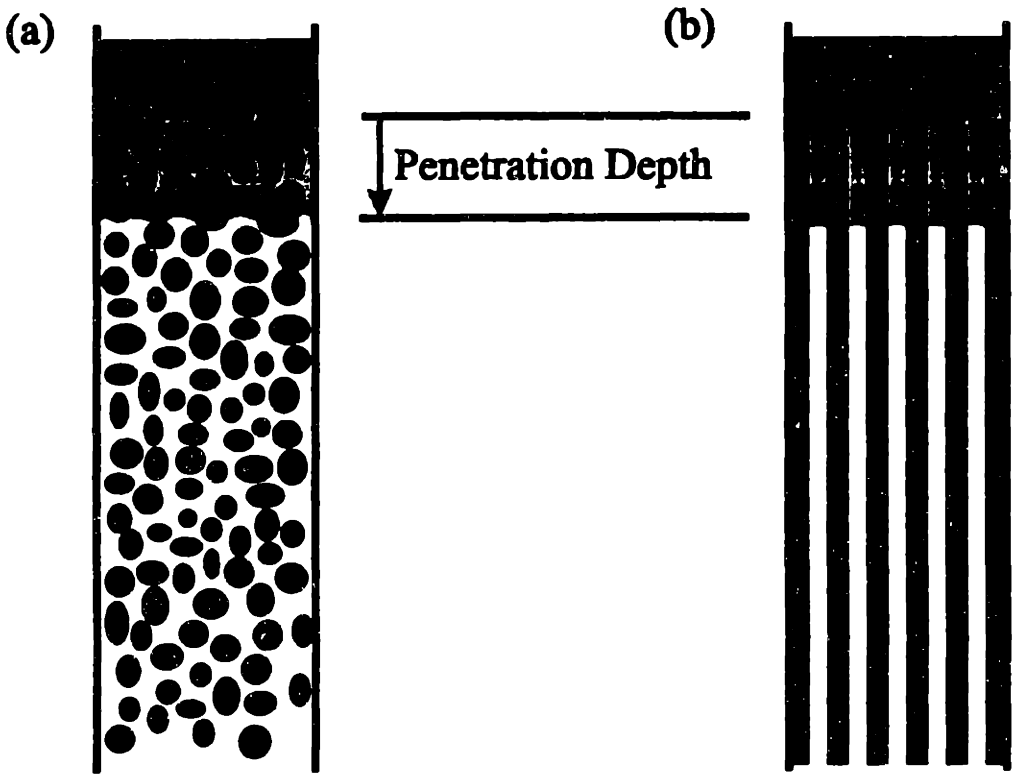

Figure 3.13 (a) Schematic of slurry infiltrating the rock bed. (b) Tube bundle model of slurry infiltrating a porous medium.

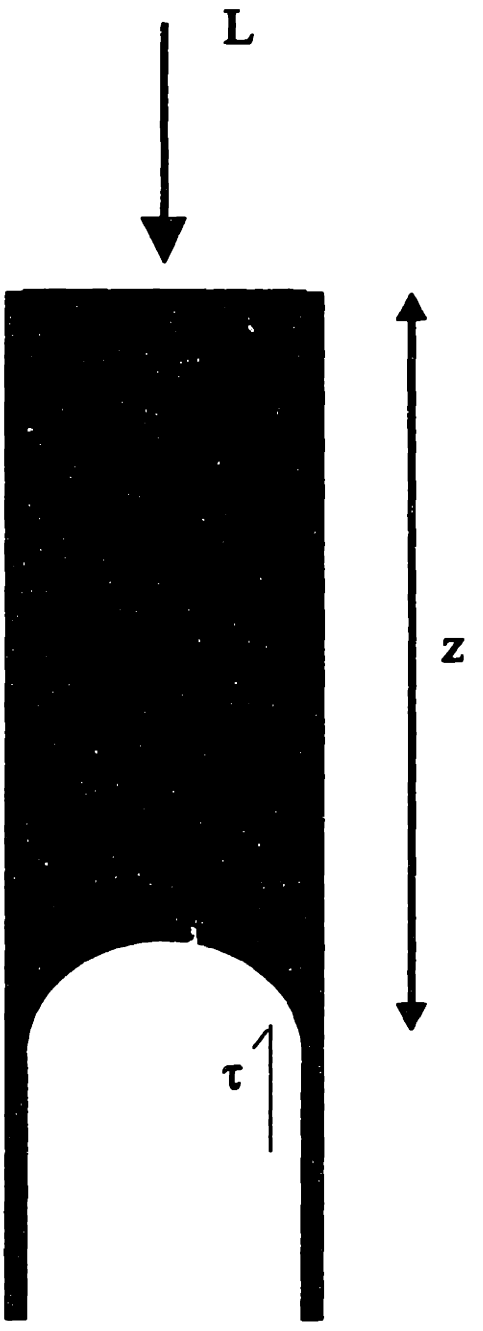

Figure 3.14 Schematic drawing of a tube in the Kozeny derivation of penetration depth as a function of yield stress.

Canceling terms and rearranging to solve for the penetration distance, z_y, gives:

$$z_y = \frac{a\rho g y}{2\tau_y} \tag{3.11}$$

The Kozeny model relates the effective diameter of the pores to the particle size of the powder comprising the bed:[26]

$$2a = D_{eff} = \frac{2}{3} D_p \frac{\varepsilon}{1-\varepsilon} \tag{3.12}$$

where D_{eff} is the effective diameter of the pores, D_p is the particle size, and ε is the void fraction of the powder bed. Substituting into equation 3.11 yields:

$$z_y = \frac{\rho g y}{6} D_p \frac{\varepsilon}{1-\varepsilon} \frac{1}{\tau_y} \tag{3.13}$$

This form of the equation can be related to the experimental data from Section 3.3 by noting that D_p and ε are properties of the powder bed and are assumed to be constant from run to run. Densities of the slurries are roughly constant, despite the changes in the clay content. Equation 3.13 can then be simplified to:

$$z_y = A\tau_y^{-1} \tag{3.14}$$

This form of the equation is identical to the experimental fit in Equation 3.7. The model confirms the experimental finding that penetration depth is inversely proportional to the yield stress of the slurry. Computation of the constant A for the model uses the following values: $\rho = 1.90$ g cm^{-3}, $g = 981$ cm sec^{-2}, $y = 7$ cm, $D_p = 0.2$ cm, $\varepsilon = 0.4$.

Using these values, A is calculated to be 290 g sec^{-2}. These units require τ_y in cgs units;

if the constant is converted to relate shear stress measured in Pascals and penetration depth measured in centimeters, the value is 29.0 kg cm m^{-1} sec^{-2}, which compares extremely well with the experimental values presented in Table 3.3.

Previous treatments of infiltration processes in the literature have modeled infiltration in terms of Darcy's law:

$$v = \frac{k}{\eta}\frac{dp}{dz} \tag{3.15}$$

where v is the flow rate, k is the permeability, η is the viscosity, p is the pressure, and z is the penetration distance.[27] This assumes that the infiltrating fluid is Newtonian, i.e. the viscosity is not a function of the flow rate. This is not true for shear thinning fluids such as particulate slurries, some polymeric systems, and reactive melt infiltration processes.[28,29]

3.4 SLURRY TRANSFER

The penetration depth experiments provide insight into the initial interaction of the slurry with the granule bed, but the tumbling action of the mixer breaks up the layered structure described in Figure 3.12. The process of this breakup and the spreading of slurry to uncoated granules was studied in a controlled laboratory mixer. A small batch mixer was used instead of a continuous process in order to ensure that residence time in the mixer could be accurately controlled.

3.4.1 EXPERIMENTAL PROCEDURES

3.4.1.1 MIXING POT EXPERIMENT

A measured amount of rock granules was preheated to the coating temperature in a rotating mixing pot. Agitation of the granules was provided by a hand held spatula. The experimental arrangement is depicted in Figure 3.15. A predispersed slurry was added to the hot granules and the spatula was used to continue the agitation as the mixing pot continued to rotate. Various batch times were used, ranging from 30 seconds to 240 seconds; a time which was felt to be comparable with the residence time in a production mixer.

The samples were removed from the mixing pot and allowed to dry in air before further analysis. Representative granules from each batch were randomly selected and photographed under an optical microscope. Typical micrographs from two of the batches appear in Figures 3.16 and 3.17. Figure 3.16 is a micrograph of a granule from the batch mixed for only 30 seconds. Figure 3.17 is from the batch mixed for 240 seconds. The rock granules are dark and the slurry appears light gray to white. Large gaps in the coating are apparent, even for the longest mixing times. These gaps are similar to those observed in the cross-sections of production granules, but are larger and more frequent, probably because no water was used in the laboratory experiment and slurry spreading was inhibited.

Twelve micrographs for each batch of granules were digitized for computer analysis. The scanned image was cropped to include only sections of the micrograph where the granule was in focus. None of the background was included in the cropped region. A histogram of the pixel values was constructed and plotted; a typical histogram is shown in Figure 3.18. The lowest pixel values represent the darkest parts of the image and correspond to uncoated rock. The highest pixels values correspond to thick droplets of the white slurry. Intermediate pixels values would represent coatings on the rock of various thicknesses and with varying lighting.

Figure 3.19 (a) shows an idealized histogram just after the slurry was introduced: there

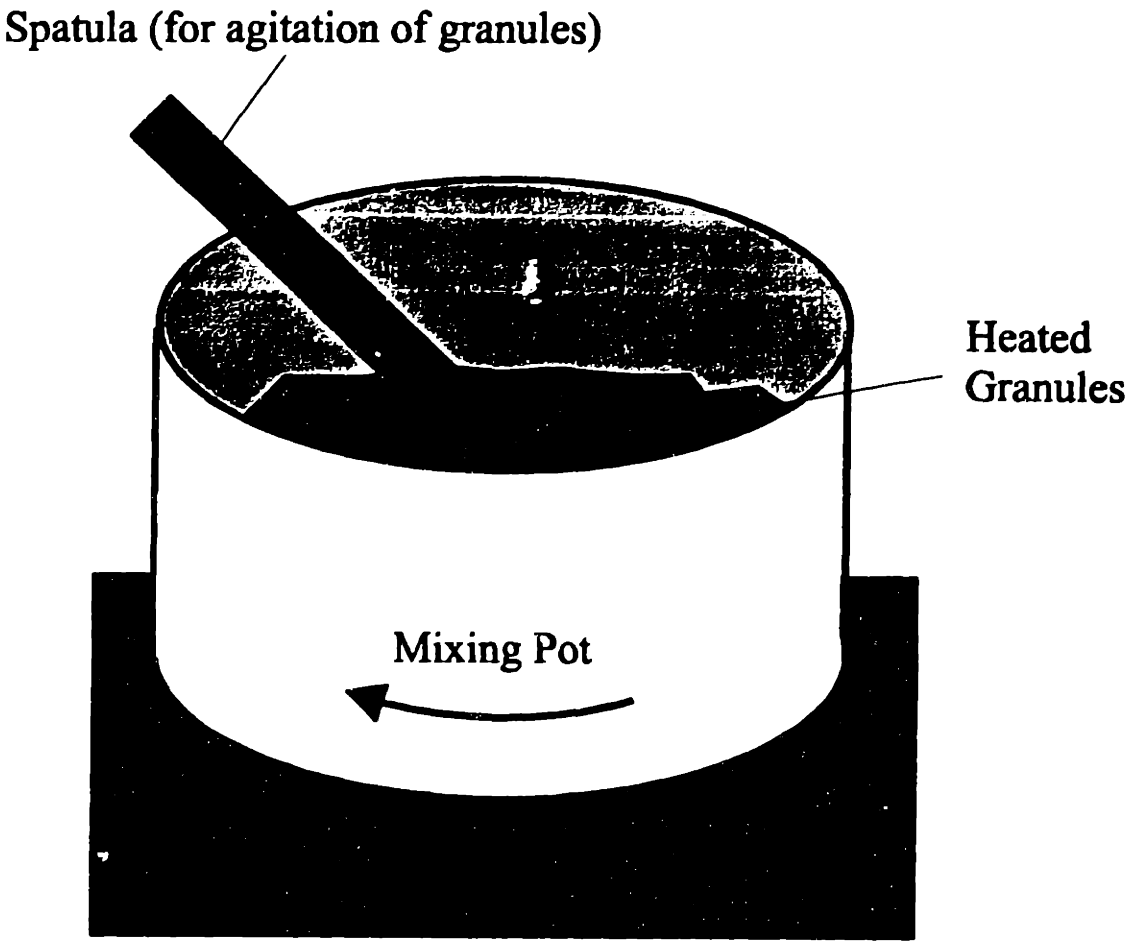

Figure 3.15 Experimental mixing pot apparatus.

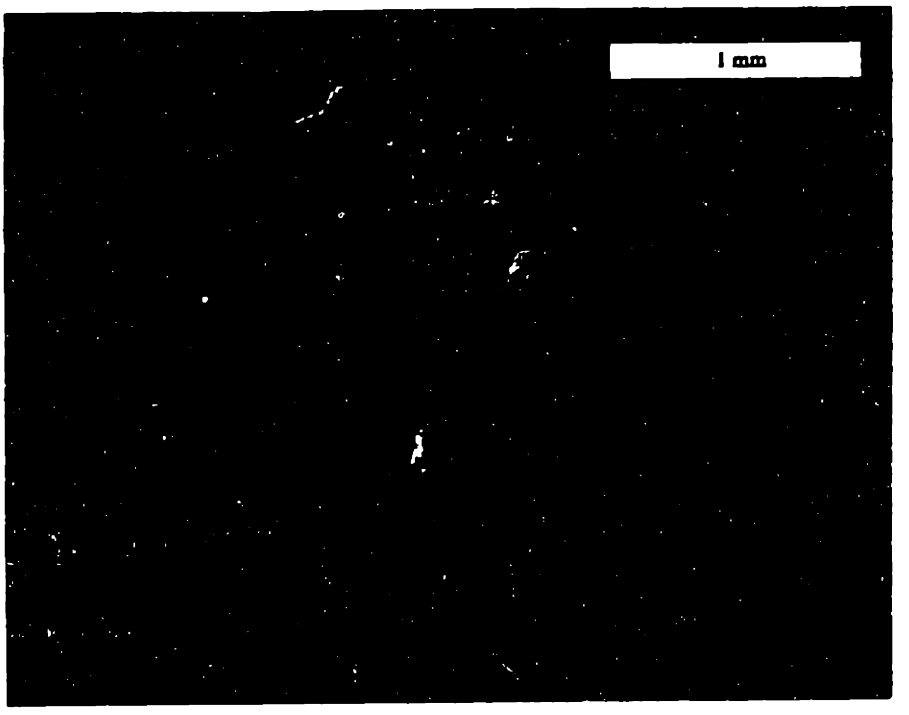

Figure 3.16 Optical micrograph of representative granules mixed for 30 seconds after application of the slurry.

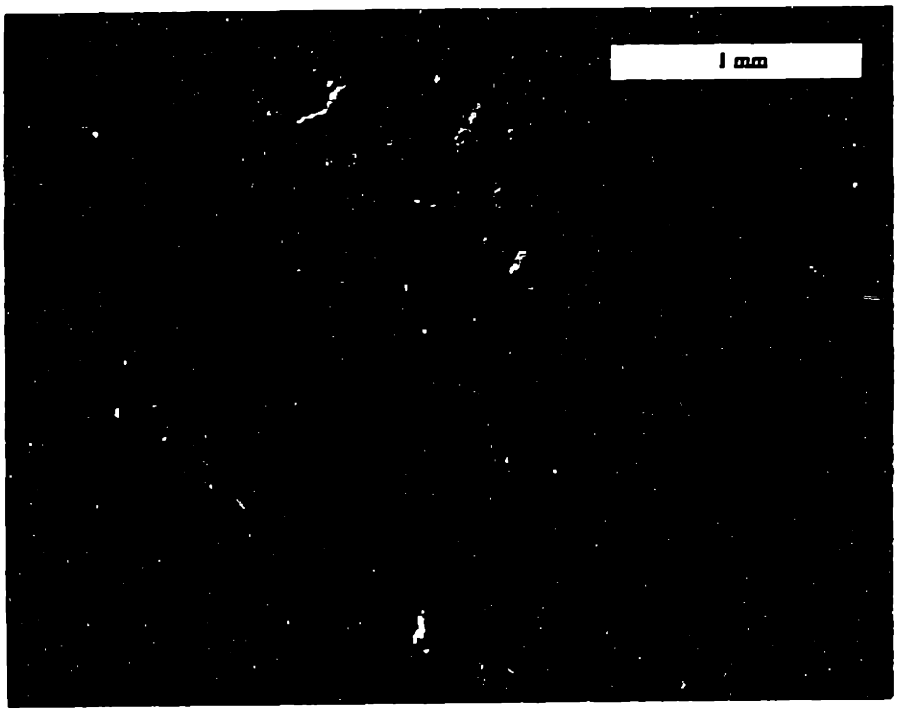

Figure 3.17 Optical micrograph of representative granules mixed for 240 seconds after application of the slurry.

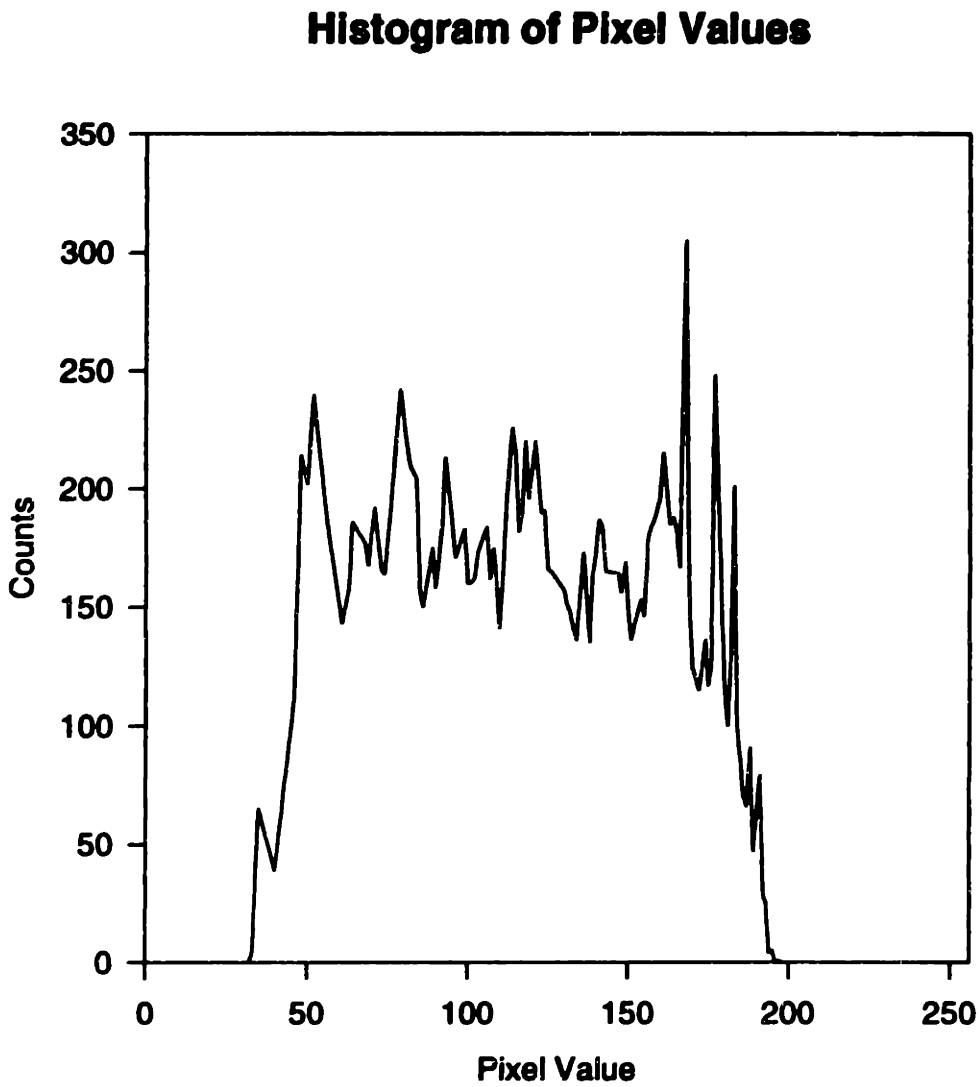

Figure 3.18 Typical histogram from an optical micrograph of a granule.

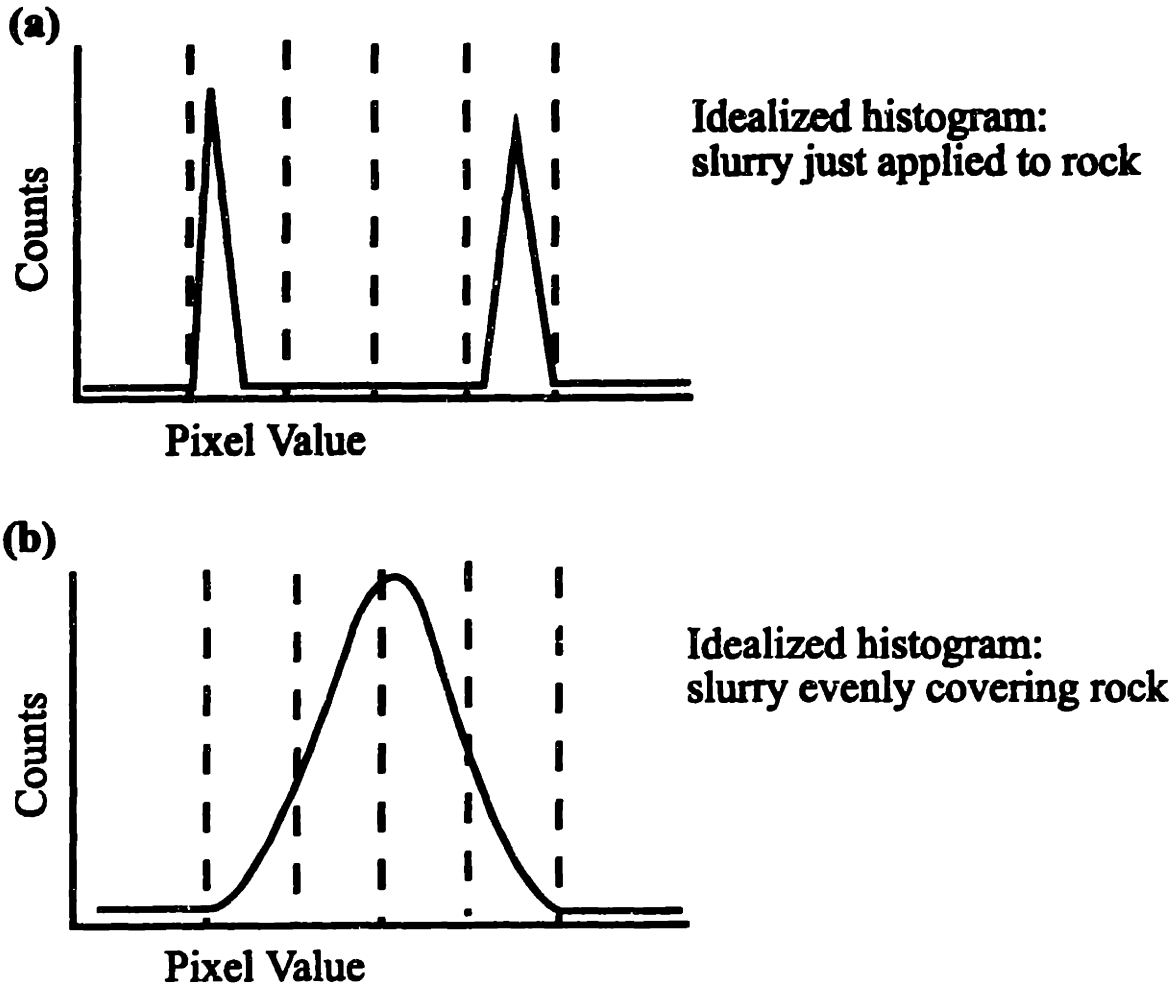

Figure 3.19 Idealized histogram of pixel values for (a) a granule just after slurry application, and (b) for a granule after long mixing times. The dotted lines represent the quartiles used for analysis of the experimental micrographs.

are sharp peaks at the low and high pixel values, corresponding to rock and slurry, respectively; and very low counts for the intermediate values. Figure 3.19 (b) shows an idealized histogram for a granule mixed for a long time. The low counts in the high and low pixel ranges indicate a lack of gaps in the coating and thick droplets. The slurry has spread into a more uniform coating.

The experimental histograms were divided into four quartiles in order to study the relative amounts in each of the pixel ranges. The formula for the quartile boundaries for each micrograph was computed as follows:

$$b_n = low + n\left(\frac{high - low}{4}\right) \tag{3.16}$$

where n ranges from 0 to 4, *low* is the lowest observed pixel value and *high* is the highest observed value. The fraction of the total pixels in the cropped region in each quartile was computed. The value for each micrograph was averaged with all the values for the particular batch. The average fraction is plotted for all four quartiles in Figure 3.20. The results of these experiments will be discussed in Section 3.4.2.

3.4.1.2 PILOT PLANT TRACER EXPERIMENT

Slurry spreading from coated granules to uncoated rock was studied in a pilot plant production line used to evaluate new process techniques and parameters.[23] The pilot production line was brought up to steady state operation with process conditions similar to those typically used in pilot plant studies and normal production. The slurry being applied was the same formulation used in previous optical properties and slurry spreading studies.

Tracer granules in a contrasting color were introduced into the mixer; see Figure 3.21 for locations. The tracers were collected as they emerged from the mixer and examined under the optical microscope.

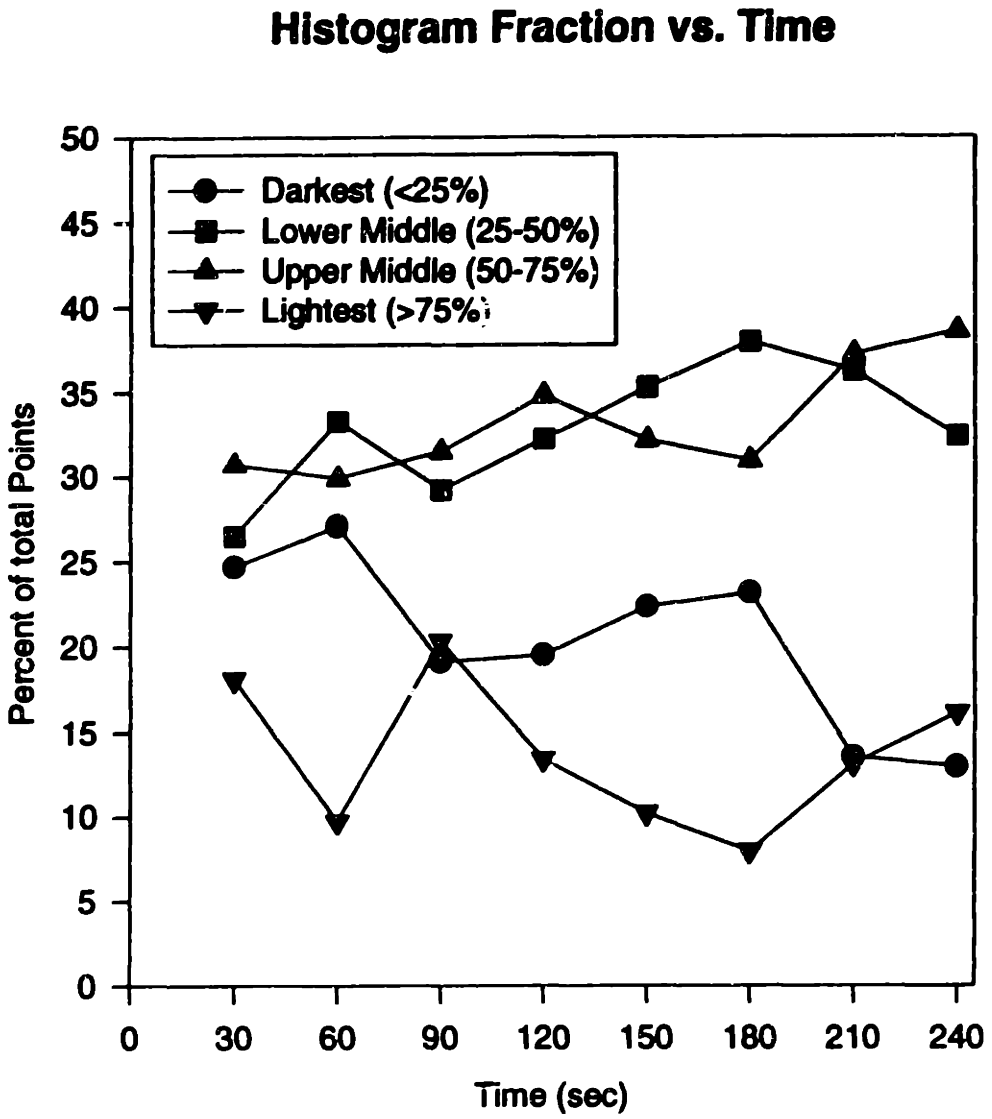

Figure 3.20 Fraction of total pixels in each quartile for the mixing pot samples.

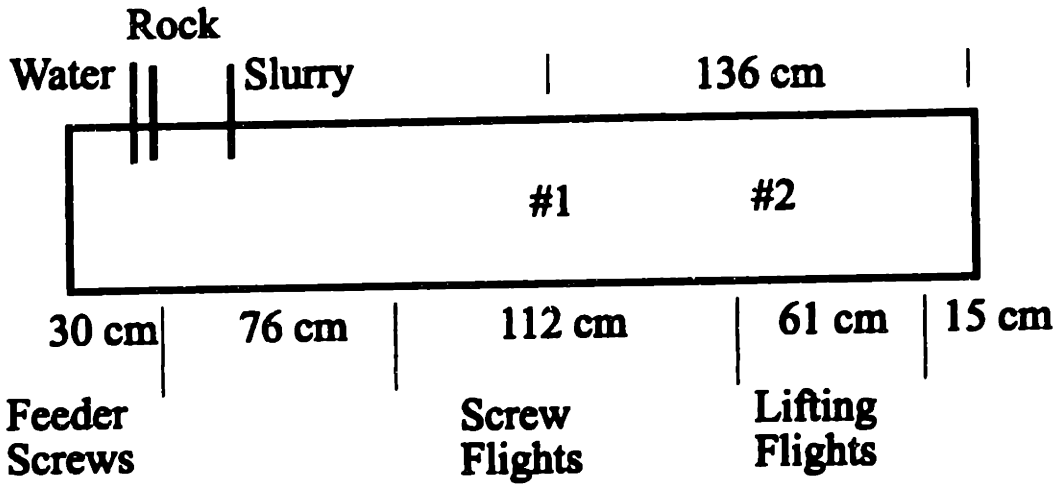

Figure 3.21 Location of tracer addition for pilot plant slurry transfer studies.

3.4.2 DISCUSSION

The laboratory mixer data shows a definite increase in the combined fraction of the two middle quartiles, showing that the slurry is spreading out to form a coating. The lowest quartile, the uncoated rock, shows a downward trend. No trend is obvious in the highest quartile data for the droplets of slurry.

The amount of spreading observed between 30 and 240 seconds is minor when compared with the period before 30 seconds. Coating coverage in this batch with the shortest mixing time is well advanced, indicating that slurry spreading occurs over a very short period of time in the mixing pot.

Figure 3.22 shows a typical micrograph from each batch of tracers. Very little slurry has been transferred to these granules. Batch 1 was introduced as close to the slurry application point as possible given the space constraints in the pilot plant production area. The lack of slurry transfer reinforces the conclusion of Section 3.5; slurry spreading over the granules occurs very quickly in the mixer over a short distance. Figure 3.23 shows the distance of the mixer over which spreading and drying must occur. Residence time data in Chapter 4 will quantify the amount of time spent in this zone of the mixer.

Slurry transfer occurs in this section of the mixer through contacts between two granules. There are three types of granules present: uncoated wet rocks, granules with wet slurry, and granules with dried slurry. This gives six distinct combinations that yield different types of interactions. These combinations are summarized in Table 3.4, along with relevant contact angles, as measured in Section 3.2.2. Most of the combinations do not lead to slurry transfer because granules with no slurry or dried slurry are interacting with other granules with no slurry or dried slurry. The cases where one granule has wet slurry and the other does not show differences in contact angle. The slurry will prefer to spread on uncoated wet rock rather than onto dried slurry. This difference in contact angle and spreadability is a driving force for spreading the slurry to all granules.

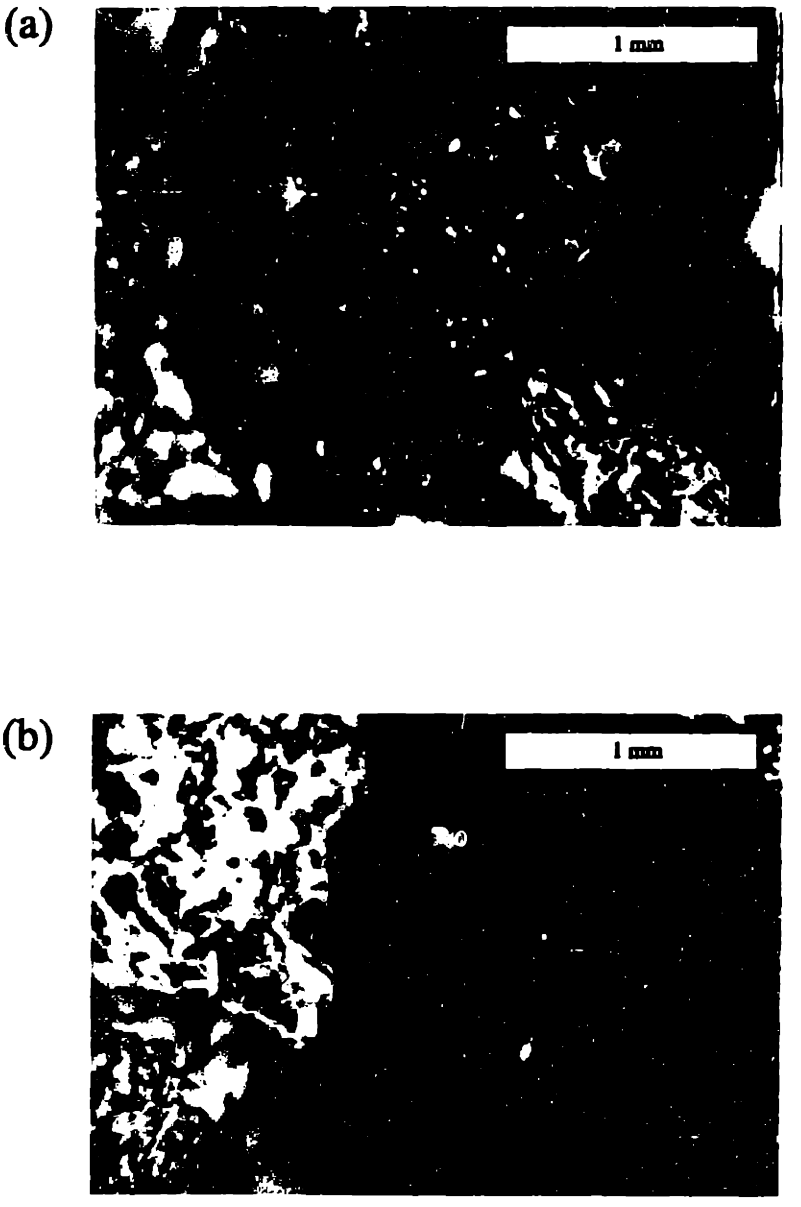

Figure 3.22 Optical micrographs of tracer granules introduced in the pilot plant mixer (a) at location #1 and (b) location #2. Each micrograph contains a non-tracer granule on the left, and a tracer granule on the right.

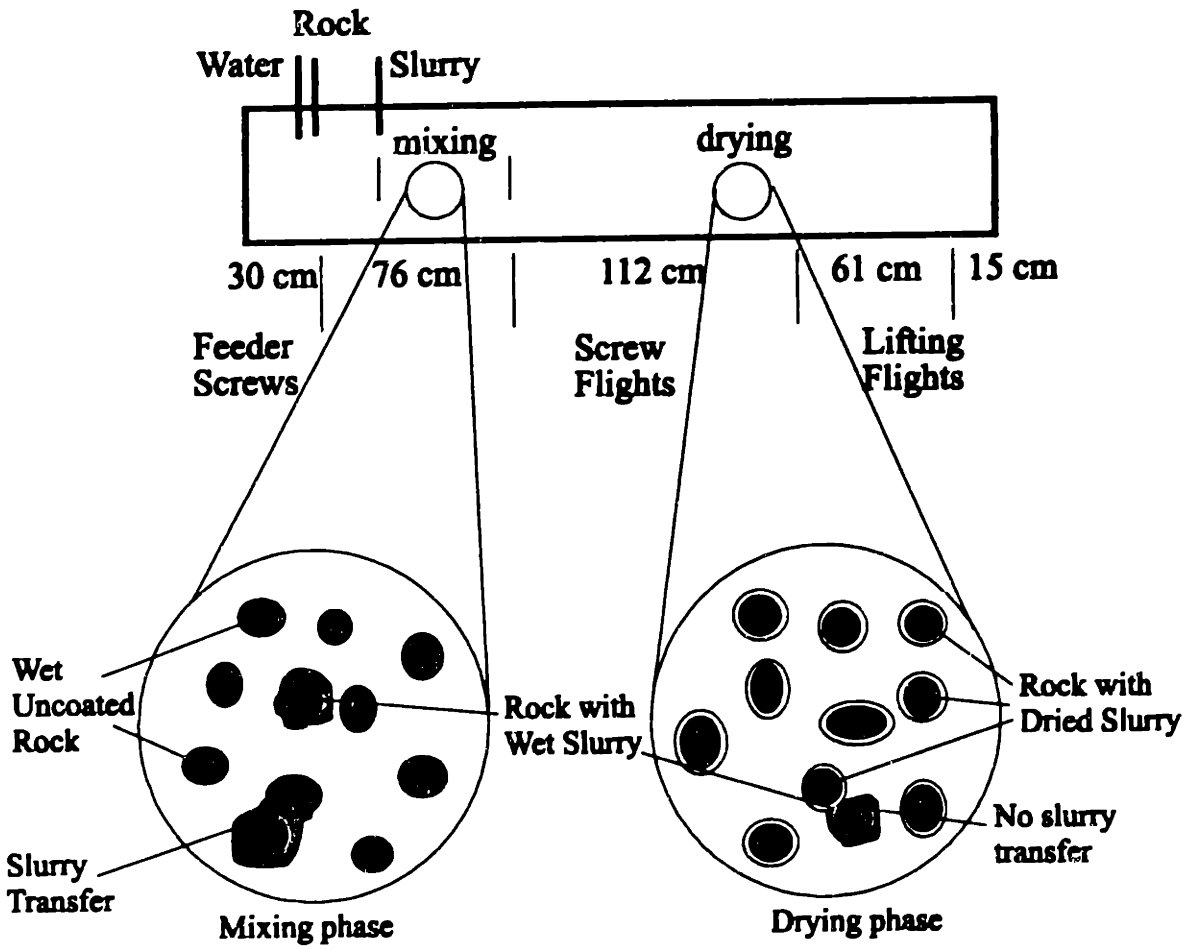

Figure 3.23 Regions in the pilot plant mixer where mixing and drying occur.

Table 3.4 Summary of granule interactions.

First Granule	Second Granule	Contact Angle
Uncoated Wet Rock	Uncoated Wet Rock	No slurry
Uncoated Wet Rock	Coated with Wet Slurry	51°
Uncoated Wet Rock	Coated with Dry Slurry	No wet slurry
Coated with Wet Slurry	Coated with Wet Slurry	0°
Coated with Wet Slurry	Coated with Dry Slurry	82°
Coated with Dry Slurry	Coated with Dry Slurry	No wet slurry

3.5 APPLICATION TO PRODUCTION SCALE

Another experiment carried out in the pilot plant involved the implementation of some of the recommendations from Section 3.2. Lower coating temperatures and increased water application rates were used to apply the third layer of a three coat roofing granule product. Slurry application rates were reduced to one half the normal values while the granules produced continued to compare favorably with granules produced under normal operating conditions.

The lower coating temperatures and additional water promoted better initial spreading of the slurry as indicated by the contact angle and penetration depth experiments. Better spreading led to more uniform coating thicknesses. The thickness was enough to meet the minimum thickness criteria established in Chapter 2 without creating thicker regions where material was wasted. The reduction or elimination of this waste coating allowed for the reduction in applied slurry without compromising coating quality.

Further experiments were carried out to implement these process changes in a production scale mixer.[30] Coating quality similar to that obtained in the pilot plant was observed and the granules passed all performance standards established for the product. This coating was again achieved using less than half of the normal amount of slurry.

Approximately 30-35% of the production cost of roofing granules is the materials cost associated with the slurry.[14] Reducing the amount of slurry used by one half would cut the cost of granule production by 15-18%, a significant savings. Although the process

changes have only been implemented on one coating of a single color granule, testing and implementation is planned for other roofing granule products.[14]

3.6 CONCLUSIONS

The experiments described in this chapter characterized the initial interaction of the slurry with the rock granules. The slurry does not penetrate very far into the rock bed, and tends to pool on top. The tumbling action of the granules in the mixer is required to spread the slurry over all the granules. This spreading operation occurs in a narrow portion of the mixer between the slurry application point and the beginning of the flights.

Contact angle data showed that the slurry preferentially spreads over a wet rock surface in comparison with a dry rock or dry slurry coating. The wet coated rock is being continually mixed with larger quantities of dry coated rock in the mixer. This promotes uniform coatings on the granules because wet slurry does not transfer to dry coated rock, so a wet rock can dry with dry coated rocks present without creating defects in the coating.

A theoretical model was developed to describe the slurry penetration into the rock bed. The model relates the penetration of the slurry into the bed with the reciprocal of the room temperature yield stress of the slurry. This model correlated extremely well with experimental results and provides a predictive tool for evaluating new slurry formulations based on laboratory measurements of rheology. The model also applies to other shear thinning liquids infiltrating porous media, such as metal or polymer matrix composites .

Specific recommendations for changes in the process parameters were indicated by experiments on the contact angle of the slurry on rock surfaces. The presence of a film of water on the granule surface was found to be crucial to slurry spreading. When water application rates were increased and rock preheat temperatures were lowered to decrease evaporation, coating quality improved. It was found that satisfactory coatings could be produced on a production scale with half the normal slurry application rate, at a significant materials cost savings.

CHAPTER 4
RESIDENCE TIME AND DRYING

4.1 INTRODUCTION

The residence time of a granule in the mixer strongly affects the quality of the coating. A granule that moves quickly through the mixer may not be completely coated which degrades the optical properties of the granule. A granule spending more than average time in the mixer will have a coating that is too thick, wasting material, or too dry which causes damage to the coating in subsequent processing.

Residence time is not typically measured in roofing granule manufacturing; however it is an important concern in bulk coating processes.[31-38] Experimental studies to determine overall residence time in a pilot plant scale mixer were carried out and are described in Section 4.2. The average residence time gives an average velocity of the granules through the mixer; however, the arrangement of the flights in the mixer changes along the length of the mixer, so it cannot be assumed the granules travel at the same velocity throughout the mixer. Most of the existing literature on rotary mixer residence times does not mention the common practice of using flights, and none of the authors treat the effects of these devices on the overall residence time distribution.

Residence times for each type of flights in the mixer were determined using a second series of experiments. Section 4.3 presents the results of these experiments and calculated average velocities in each of the sections of the mixer. Section 4.4 discusses the effect of each type of flights on residence time. Slurry spreading results of the previous chapter are compared with the velocity measurements to determine the amount of time a granule will spend in the slurry spreading section of the mixer and how long the drying process takes in the mixer. Chapter 3 showed that slurry was not transferred between wet rock and dry coated rock, allowing defect free coatings to be produced. The

locations in the mixer where the coated rocks are dry enough for this to occur are determined in Section 4.5 with a mathematical model of rock moisture content in the mixer based on data collected from the experiments in Section 4.2 and 4.3. Section 4.6 presents the conclusions of this chapter.

4.2 EXPERIMENTAL PROCEDURES

Overall residence time in the pilot plant mixer[23] was measured with a pulse tracer method. Normal operating conditions for the pilot plant were used to bring the system to steady state. The feed into the mixer was granule with two previously applied coats of a brown pigmented, copper containing coating. The slurry being applied in the run was a seal coat that did not contain copper.

After running at steady state for 10 minutes, the feed of preheated granules was interrupted for thirty seconds and replaced with a feed of an equivalent quantity of tracer granules. These granules were coated with a previously applied white coating with no copper. This provided two means of identifying the tracers: the lack of copper, and a visual difference due to the fact that the seal coat was thin enough to see the underlying color. The normal feed of brown, copper containing granules was resumed at the end of the 30 second tracer pulse.

Samples of the material exiting the mixer were collected every 15 seconds. These samples were later analyzed for copper content with an X-ray fluorescence (XRF) technique. Each sample from the mixer was divided into four sub-samples and each was scanned four times with an X-Met XRF detector[39] calibrated to read copper content. The sixteen data points for each sample were averaged and plotted. These plots were normalized by the largest count reading for all the sub-samples.

A second set of tracer experiments were performed in the pilot plant mixer[23] to determine residence time distributions for the different segments of the mixer. Figure 4.1 shows the types and lengths of the flights in the mixer. The lifting flights at the end of the mixer and the screw flights just before them are of principal concern in these experiments.

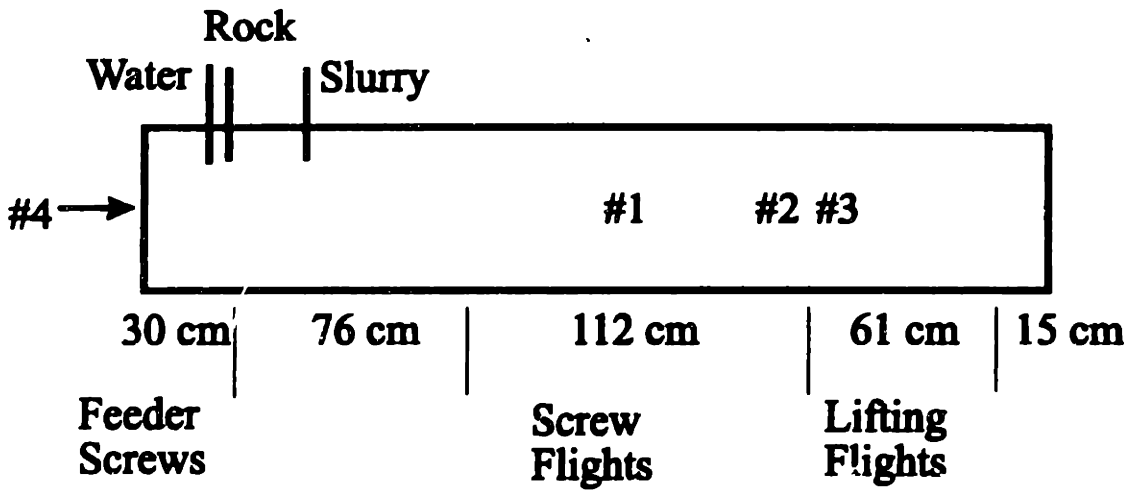

Figure 4.1 Diagram of the pilot plant mixer with injection points for the tracers in the residence time experiments. #1-#3 are flight residence time experiments, #4 is the overall residence time experiment.

Steady state conditions were established in the pilot plant production line. The feed from the preheater was raw uncoated rock and the slurry used was a white similar to that used for the experiments in Chapter 2 and 3. The tracer granules used were rock that had been previously coated with a brown, copper containing coating. The tracers were introduced into the mixer by means of a small can attached to a pole. The can was filled with tracers and pushed into the mixer. The can was turned upside down and removed once it was in position. Samples were collected at the mixer exit every 15 seconds.

Initial analysis of the samples from the first run was by the XRF method, as described in Section 4.2. This method was too time consuming for all runs and an optical counting method was employed for some runs. The optical count and XRF data for the first run are compared in Figure 4.2. The width of the peak and the position of the maximum are identical and the two methods appear to produce comparable results.

4.3 OBSERVATIONS

Figure 4.3 is a plot of the normalized counts recorded over the time of the experiment. The time axis is the time elapsed since the beginning of the introduction of the tracer pulse. The error bars on each point represent one standard deviation as calculated from the sixteen measurements made for each sample. The data shows a high, steady copper concentration at the beginning, indicating the mixer was in steady-state operation. The copper concentration begins to decrease around 250 seconds as the first tracer granules begin to exit the mixer. The copper concentration reaches a minimum at 375 seconds as the tracer concentration reaches its maximum. The tracer concentration falls to zero and the copper concentration resumes its normal level by 480 seconds. A second smaller pulse of tracers exiting the mixer occurs from 495 seconds to 600 seconds. The copper concentration returns to normal steady-state values after this seconds pulse.

Table 4.1 contains a summary of the average linear velocities computed for several residence times of interest determined from the plot. There is a large variation in residence times and velocities, especially if the granules in the second pulse are

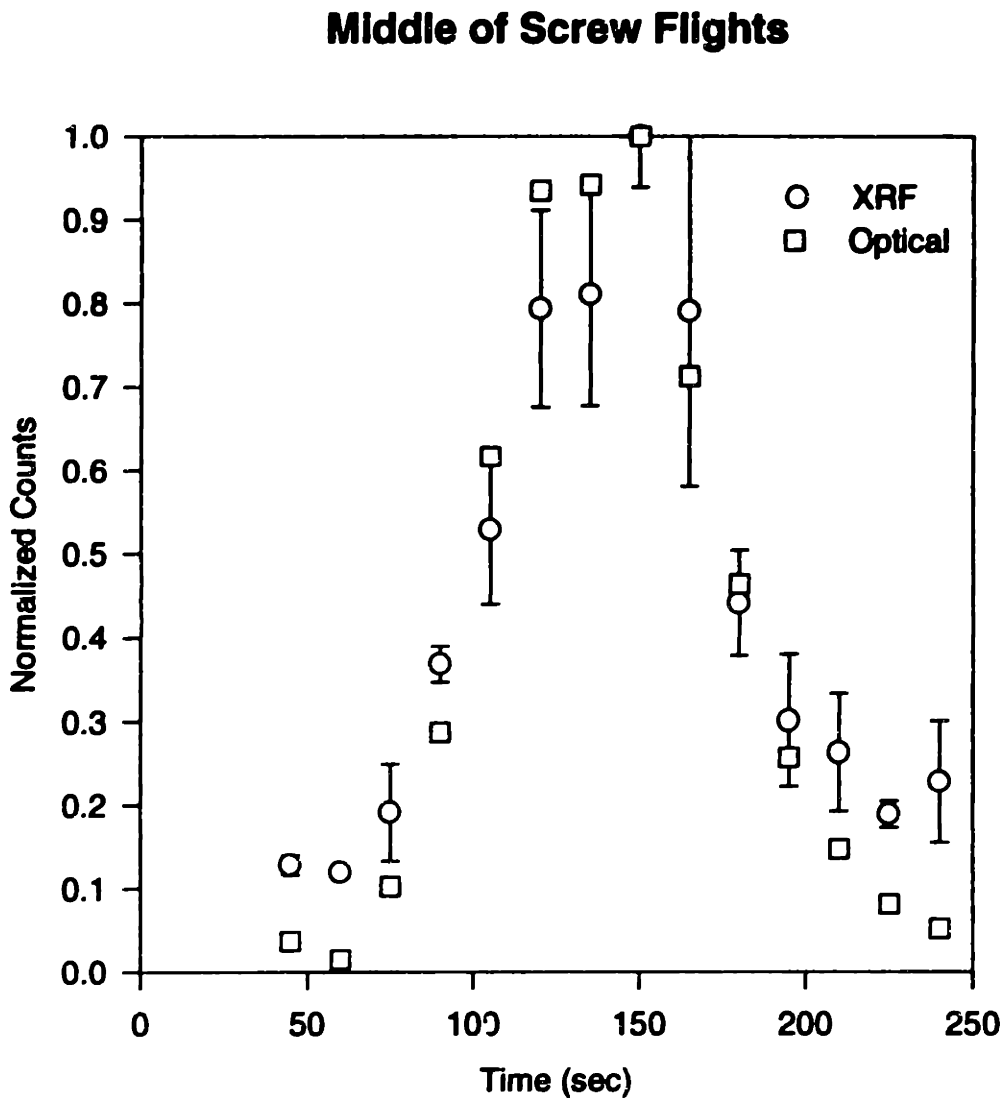

Figure 4.2 Comparison of XRF and optical count data for a tracer experiment. Tracers were introduced at location 1 in Figure 4.1.

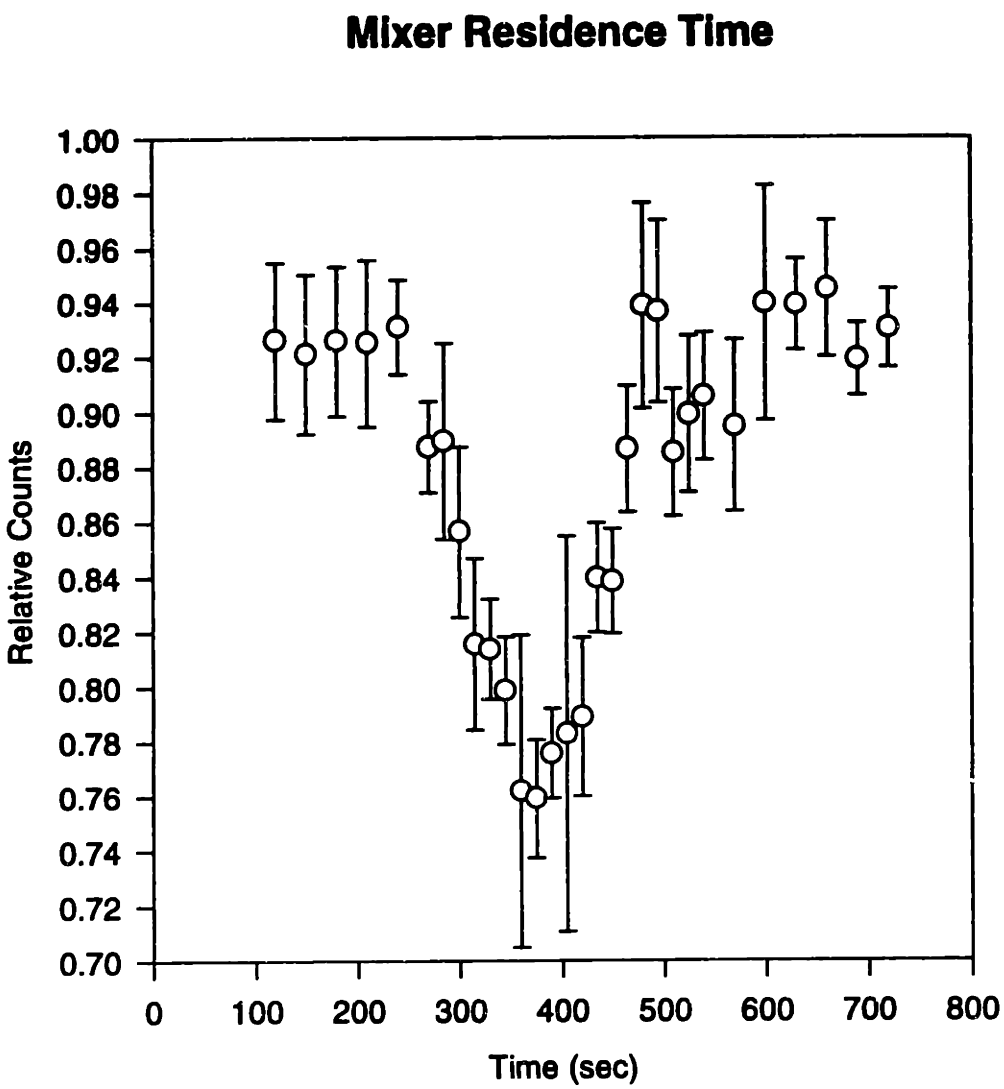

Figure 4.3 Plot of normalized copper counts vs. time for the pulse tracer experiment to measure overall residence time.

considered. This variability in the process inhibits reproducibility in coating quality from one granule to the next. Each section of the mixer must be examined to determine how the different types of flights present in the mixer affect the average velocity of the granules and the variation among granules

Table 4.1 Average Velocities calculated from the overall residence time experiment.

Pulse	Time to Exit Mixer (sec)	Average Velocity (cm sec^{-1})
Start of First Pulse	270	1.13
Peak of First Pulse	395	0.77
End of First Pulse, Start of Second Pulse	480	0.64
End of Second Pulse	600	0.51

Figure 4.4 and 4.5 are plots for the remaining runs in the tracer experiment. All three residence time distributions for this experiment show a single maximum, unlike the overall distribution in Figure 4.3. This indicates that the second pulse observed in that experiment must occur before location #1 in Figure 4.1. It is likely that some granules are held up in the slurry application area just prior to entering the screw flights, possibly because they are sticking to the walls of the mixer and are later released. The velocities of these granules were not used in later calculations due to this phenomenon, and only velocities of granules in the main peak were used.

Average granule velocity through each section of the mixer was calculated from the average residence time in each segment and the segments following. It was assumed that the granules did not change velocity through a particular segment, and that the final 15 cm segment after the lifting flights was negligible.

A summary of the pertinent data can be found in Table 4.2 and a plot of the average linear velocity is shown in Figure 4.6. Average velocity for the first section includes the initial rock feeder flights and the slurry application area. Although the velocity is shown to be constant in Figure 4.6, it is almost certainly not constant in reality. The difficulty of accessing these areas prevented tracer introduction to measure the velocity.

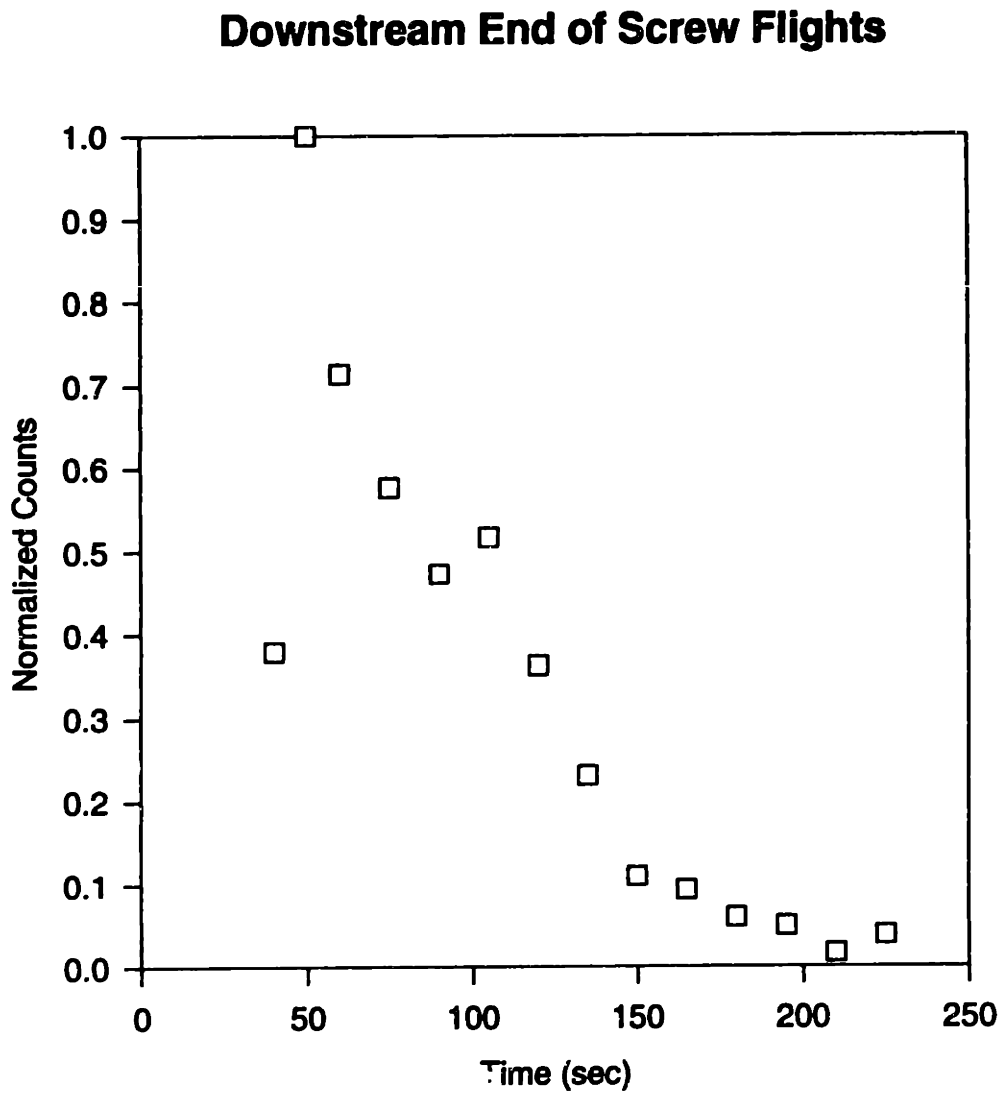

Figure 4.4 Residence time distribution for tracer experiment. Tracers were introduced at location 2 in Figure 4.1.

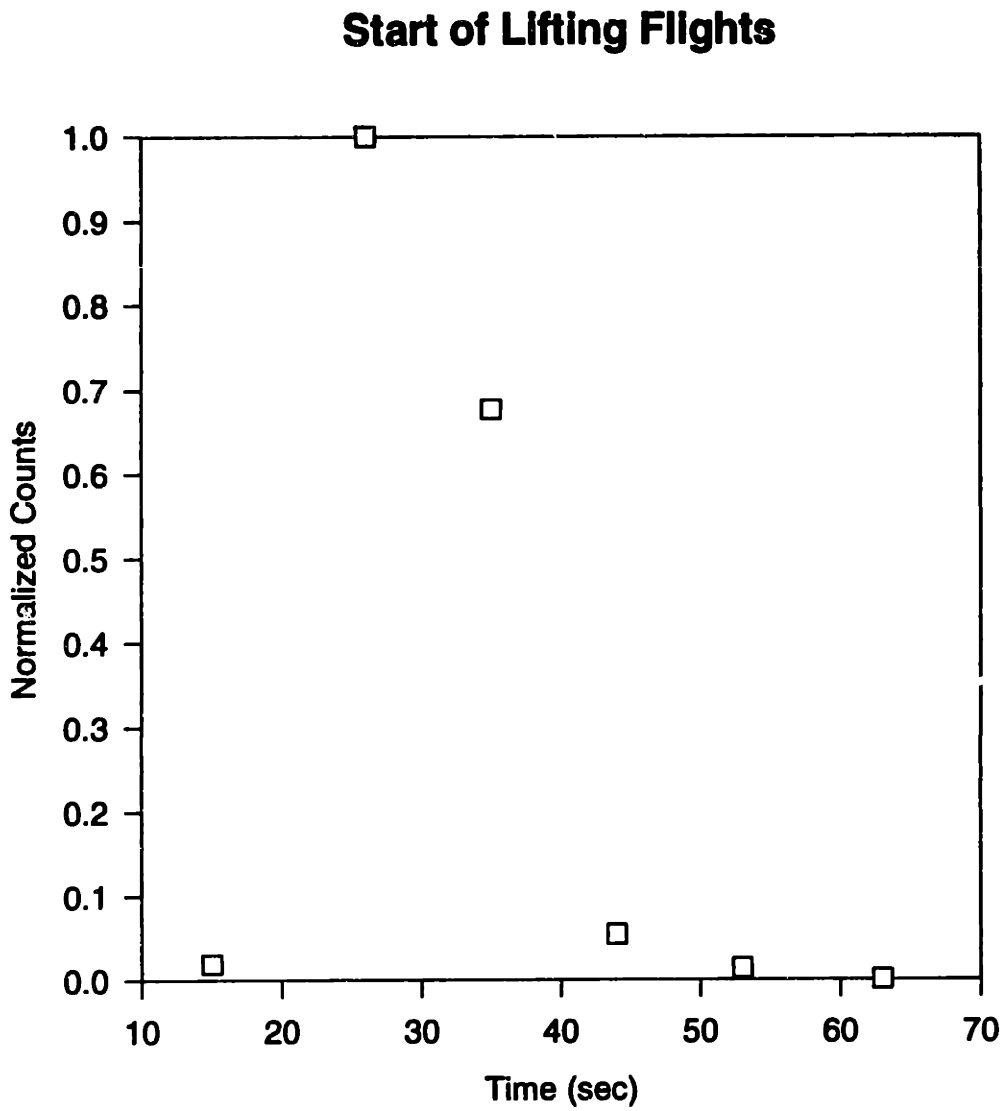

Figure 4.5 Residence time distribution for tracer experiment. Tracers were introduced at location 3 in Figure 4.1.

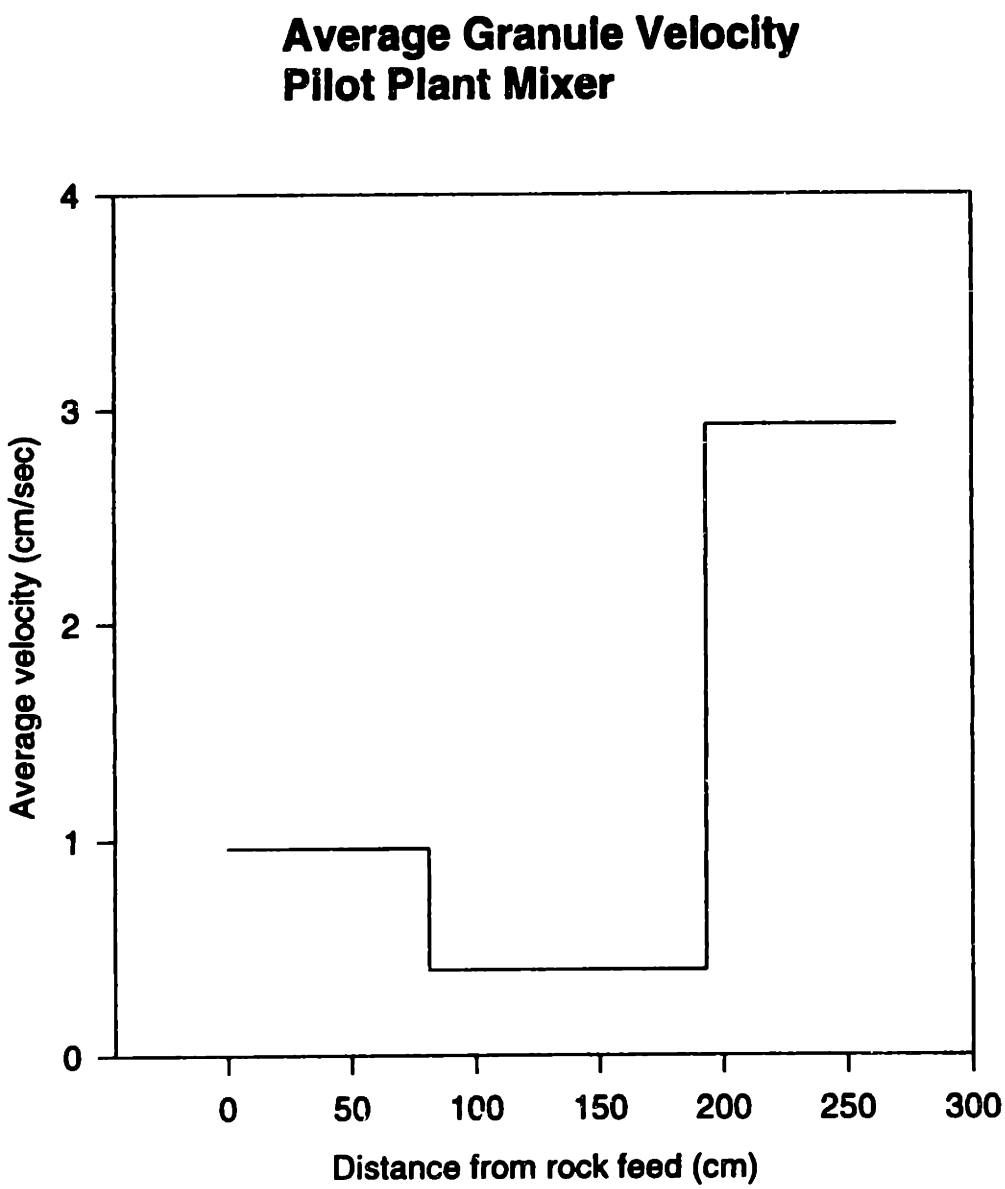

Figure 4.6 Plot of average granule velocity through each section of the mixer calculated from tracer experiments.

Table 4.2 Average velocities calculated for various sections of the pilot plant mixer from tracer data.

Section	Residence Time (sec)	Velocity (cm sec^{-1})
Rock Feed and Slurry Application	85	0.96
Screw Flights	140	0.40
Lifting Flights	26	2.93

4.4 DISCUSSION

4.4.1 EFFECT OF FLIGHTS

Average velocity through the screw flights is very low due to the back mixing effect of this type of flights. Figure 4.7a shows that the geometry of the flights pushed the granules "upstream," opposite the normal plug flow. The lifting flights show a much faster velocity because the shape of these flights does not cause as much back mixing. The average granule velocity through the slurry mixing stage must be quite slow if it is assumed that the feeder flights in the front end of the mixer have a faster average granule velocity. Although the average velocity through the mixer is not constant, the mixer can be run in steady state. The areas where back-mixing is occurring have a deeper bed and therefore a higher mass flux to compensate for the slower linear velocity. Figure 4.7b shows a schematic of typical granule trajectories in the mixer. The figure is shaded to represent mass flux in the mixer, darker shading indicating higher mass fluxes and a deeper bed.

The screw flights are also responsible for the broadening of the residence time distribution. The distribution in Figure 4.4, for the screw flights, is significantly broader than the width of the injected pulse and approaches the width of the distribution of the overall residence time.

Most models of back-mixing in rotary mixers involve a step-wise motion along the axis of the mixer, with the lengths of the steps and their intervals determined randomly as the particle reaches the top surface of the bed and cascades down the fluidized layer.[38] Flights lift the particles higher, effectively increasing the size of the fluidized region and

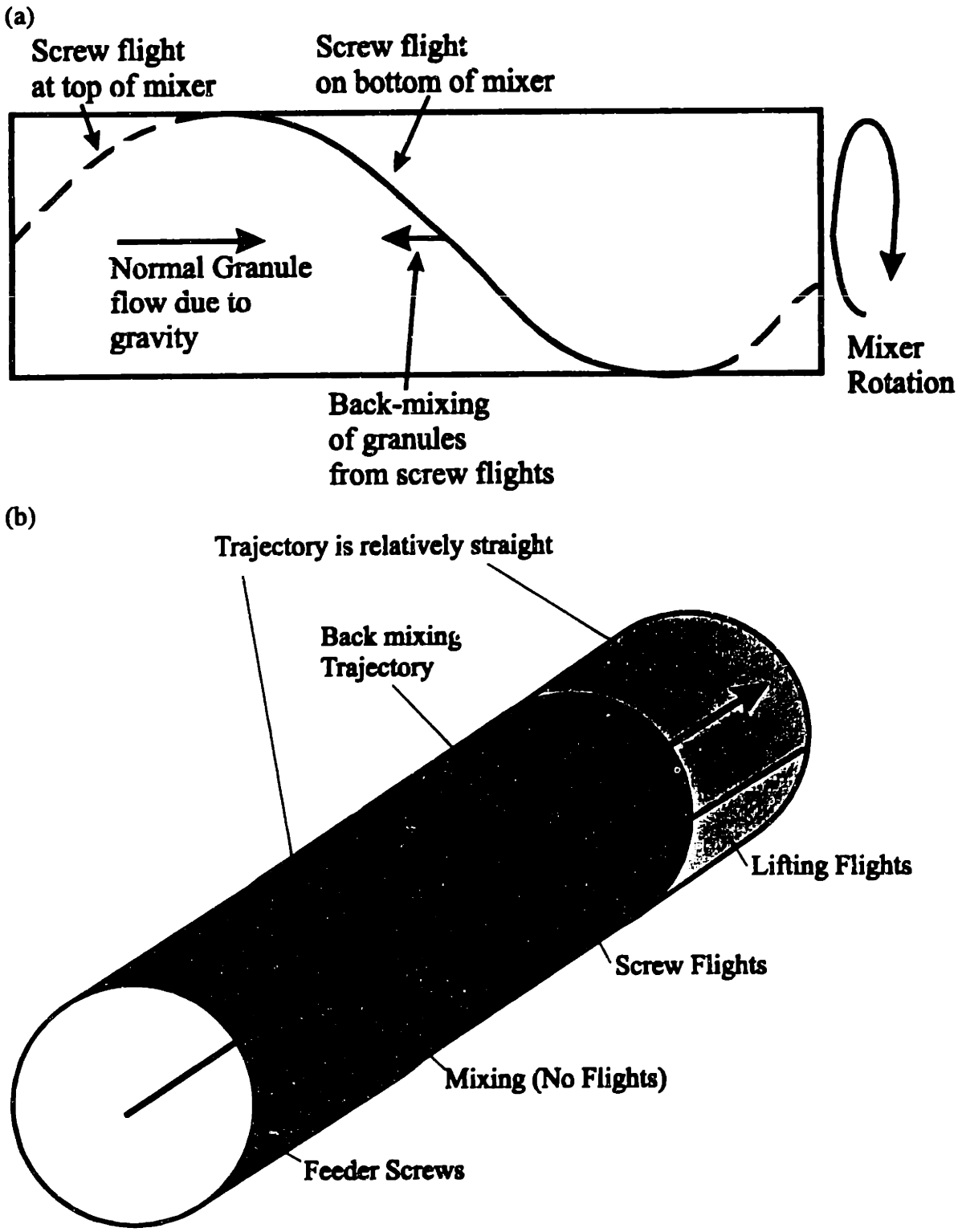

Figure 4.7 (a) Geometry of a screw flight showing how "back-mixing" occurs. The mixer is viewed from above. The screw flight is repeated at 90° intervals around the interior surface of the mixer. (b) Typical particle trajectory through each section of the mixer. Linear velocity though the screw flights is the slowest. Shading indicates bed depth, darkest corresponding to the deepest bed.

lengthening the distance over which random collisions with other particles can act, and increase the size of the random steps the particle can take. The increased randomness due to the flights causes the broader peak in residence time.

The lack of flights in the section of the mixer where spreading is occurring means that the residence time in that section probably has a much narrower distribution, ignoring the second pulse due to sticking to the mixer walls. The narrower distribution of residence times in this section means that the large majority of the granules spend approximately the same amount of time in contact with the slurry pool and under the right conditions could produce a coating of uniform thickness on each granule.

Another effect of the flights in the mixer is to reduce segregation of the granules by particle size. Numerous authors have reported axial segregation of particles in rotary mixers.[40-43] These studies have shown that particles in rotary mixer systems exhibit two different types of motions. Most particles in the bed move in solid body rotation with the mixer itself. A cascading action fluidizes the top surface of the bed when the particles have rotated such that the surface of the bed is inclined more than the angle of repose of the powder material. These particles travel downwards and rejoin the solid body rotation, see Figure 4.8.

Segregation occurs because the surface roughness of the boundary layer between the solid body rotation and the fluidized layer affects particles of different sizes differently. Smaller particles are more likely to fall into a gap between two particles, while larger particles tend to keep rolling and travel farther from the mixer axis. Figure 4.9 is an extreme example of mixer segregation in a bidisperse particle system.[41]

The flights in the mixer in roofing granule manufacture effectively prevent any such segregation. The flights lift all the material much higher than solid body rotation would carry it. The granules cascade from a greater height than would be the case without the flights. The granules have more energy and are traveling almost vertically, and the likelihood that they will be stopped by crevices in the surface of the bed is greatly reduced.

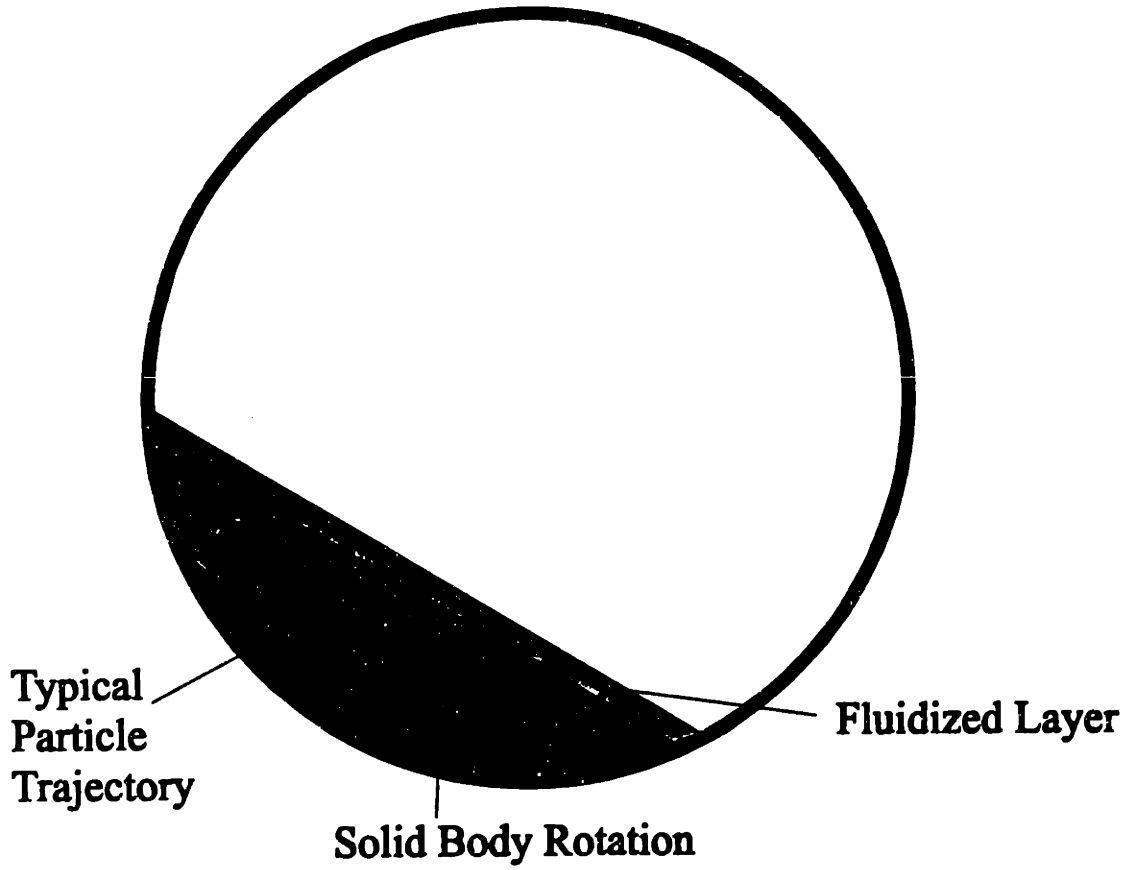

Figure 4.8 (a) Schematic of particle motion in a rotary mixer in the plane perpendicular to the mixer axis.

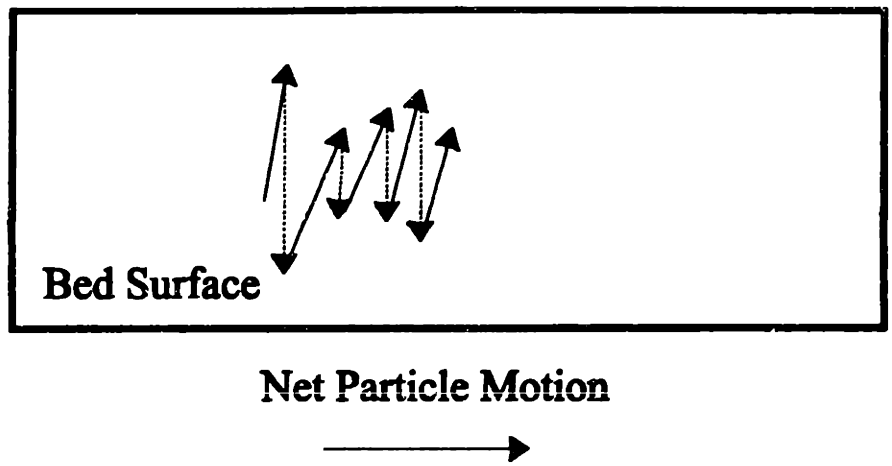

Figure 4.8 (b) Schematic of particle motion in a rotary mixer viewed from above the bed surface.

Figure 4.9 Exar, ple of axial segregation in a rotary mixer. The white particles are 6 mm in diameter and the white particles are 10 mm in diameter. From [41]

4.4.2 SLURRY SPREADING AND DRYING IN THE MIXER

The results of the mixing pot and slurry transfer to tracer experiments discussed in Chapter 3 indicated that the slurry spreads quickly over the granules and much of the mixer was devoted to drying. The average granule velocity can be used to estimate the amount of time required for these processes.

Slurry mixing seems to be completed before the average granule reaches the screw flights, as indicated by the slurry transfer experiments. The time spent in this section is 58 sec, based on a distance of 55.9 cm and an average velocity of 0.961 cm sec^{-1}. This time is long compared with the initial mixing time observed in the mixing pot (less than 30 seconds) and extends into the time where slower changes were taking place (see Figure 3.20).

Drying of the granules occurs during passage through the screw and lifting flights, which is estimated to be 290 seconds. The rate of slurry application is 0.0624 kg slurry per kilogram of rock. The slurry was 30 wt.% water, meaning that approximately 0.0187 kg water per kilogram of rock must be removed during this section of the mixer. The data is only approximate because additional water, as much as 0.006 kg water per kilogram of rock is applied to promote spreading, and it is not known how much of that water is retained through mixing into the drying phase. Additionally, the granules are not completely dry when they exit the mixer, and still contain 0.007-0.008 kg water per kilogram of rock.

The residence time data indicate that the average granule spends 290 seconds in the screw flights and lifting flights. The slurry transfer data indicates that drying occurs principally in these sections, giving a drying flux of approximately 6×10^{-3} kg sec^{-1} m^{-2} based on a rock surface area of 10 mm^2 per gram of granules.

4.5 MIXER DRYING MODEL

4.5.1 CONTINUOUS FLOW STIRRED TANK REACTORS

The average velocity of the granules was found to be much slower in the screw flight section than in other sections. The combination of the slow velocity and long residence time with the back-mixing effect of the screw flights indicates that this section of the mixer can be represented by a series of continuous flow stirred tank reactors (CSTR). The main features of a CSTR are that the reactor contents are perfectly mixed and that the outflow composition is identical to the composition of the material in the reactor.[44]

The assumptions governing a CSTR allow a simple mathematical model to be developed which will allow calculation of the output response to any changes in the input flow. The governing equation for a CSTR is:

$$V\frac{dC}{dt} = F_{input} - F_{output} - R_{reaction} \tag{4.1}$$

where V is the volume of the reactor, C is the concentration of a reactant in the reactor, and dC/dt represents an accumulation term. F_{input} is the rate of flow of the reactant into the reactor and F_{output} is the rate of flow of the reactant out of the reactor. $R_{reaction}$ is the rate of disappearance of the reactant through chemical reactions in the reactor.

The introduction of a tracer pulse to the mixer can be considered a reactant in the above equation. The tracers' reaction rate is zero, so the reaction term is ignored. The input flow is:

$$F_{input} = Q\delta(t - t_0) \tag{4.2}$$

where Q is the total volumetric flow rate through the reactor and $\delta(t-t_0)$ is a delta function

input of the tracers introduced at time $t=t_0$. The output flow is simply the volumetric flow rate, Q, times the concentration of tracers in the output flow:

$$F_{output} = QC_1(t) \tag{4.3}$$

A characteristic of CSTR's is that the output flow is identical to the composition of the contents of the reactor, so:

$$C(t) = C_1(t) \tag{4.4}$$

Combining Equations 4.1-4.4 yields the differential equation:

$$V\frac{dC_1(t)}{dt} = Q\delta(t-t_0) - QC_1(t) \tag{4.5}$$

This differential equation is readily solved by utilizing Laplace transforms. The transform of the differential equation is:

$$V\left(sF - C_{1,t=0}\right) = Q(e^{-st_0} - F) \tag{4.6}$$

where $F(s)$ is the transform of $C_1(t)$. $C_{1,t=0}$ can be assumed to be zero if the tracer pulse is introduced at a time t_0 greater than zero. The transformed differential equation can be simplified by dividing through by the volume of the reactor, V,

$$sF = \frac{Q}{V}\left(e^{-st_0} - F\right) \tag{4.7}$$

and defining a characteristic time constant, τ, equal to the volume of the reactor divided by the volumetric flow rate into the reactor:

$$\tau = \frac{V}{Q} \tag{4.8}$$

The transformed equation can then be solved for F as follows:

$$F = \frac{e^{-st_0}}{s\tau + 1} \tag{4.9}$$

Taking the inverse Laplace transform results in the solution:

$$C_1(t) = u_{t_0} e^{-(t-t_0)/\tau} \tag{4.10}$$

where u_{t0} is a step function:

$$\begin{aligned} u_{t_0} &= 0, t < t_0 \\ u_{t_0} &= 1, t \geq t_0 \end{aligned} \tag{4.11}$$

The output Equation 4.10 is plotted in Figure 4.10. The output concentration of tracers from a single CSTR has an initial peak at $t=t_0$, and falls off exponentially. This residence time distribution does not correspond to the shape of the experimental distribution in Figure 4.2, so the screw flight section cannot be modeled by a single CSTR. Adding a second CSTR in series to the first gives the equation:

$$V\frac{dC_2(t)}{dt} = QC_1(t) - QC_2(t) \tag{4.12}$$

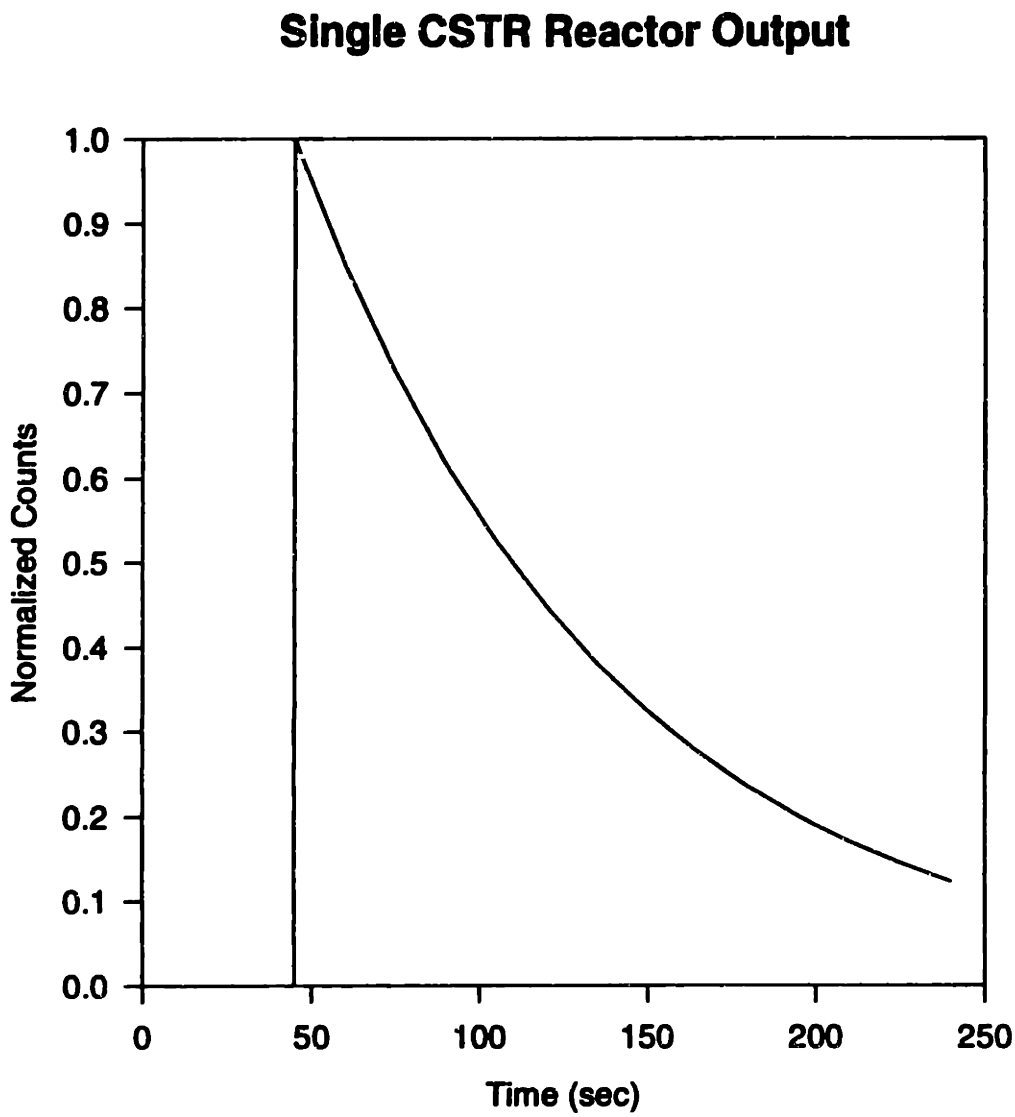

Figure 4.10 Plot of single CSTR output vs. time. From Equation 4.10, t_o=45, τ=279.

This equation is identical to Equation 4.5, except that the accumulation term and outflow term have a subscript 2, referring to the second CSTR, and the input term is now the output of the first CSTR, $C_1(t)$. This equation can be solved by Laplace transform as before, with the solution:

$$C_2 = \frac{1}{2\tau^2} u_{t_0} e^{-(t-t_0)/\tau}(t-t_0) \tag{4.13}$$

Adding more CSTR's in series and solving the differential equation gives a general solution for n CSTR's:

$$C_n = \frac{1}{n!}\frac{1}{\tau^n} u_{t_0} e^{-(t-t_0)/\tau}(t-t_0)^{n-1}, n = 1,2,3... \tag{4.14}$$

It can be seen that this general solution reduces to the specific solutions solutions in Equations 4.10 and 4.13 for n=1 and n=2, respectively.

The general solution in Equation 4.14 can be used to fit the theoretical model CSTR series to the actual data from the pilot plant mixer. The average velocity through the screw flights section was calculated to be 0.40 cm sec^{-1} and the length of this section is 111.8 cm. The length divided by the linear velocity is identical to the volume divided by the volumetric flow rate and is defined as τ in Equation 4.8. The time constant for a single reactor in the series is:

$$\tau = \frac{V}{Q} = \frac{V_T}{nQ} = \frac{L}{nv} \tag{4.15}$$

where V_T is the total volume of all CSTR's in the series, V is the volume of an individual CSTR, L is the total length of the screw flight section of the mixer and v is the linear velocity of the granules. The beginning of the pulse in Figure 4.2 is at t=45 sec, so this is the value of t_0.

Figure 4.11 is a plot of the data in Figure 4.2 and the output of the mathematical model for several values of n. Figure 4.12 is a plot of the indicated average residence time from Figure 4.11. The data shows that a value of n=6 is sufficient to represent the data, and increasing n does not increase the accuracy of the fit.

The injection point for the tracers in Figure 4.2 was location #1 in Figure 4.1, and was halfway along the length of the screw flights. A total of 12 CSTR's are necessary to represent the screw flights.

4.5.2 MIXER MODEL

A numerical mixer model was developed using 12 CSTR's in series. The mixer was assumed to be in steady state, and each CSTR was assumed to be in equilibrium. The model first computes the temperature and moisture content of the rock after injection of water and slurry. The equation for rock temperature after water injection is:

$$T_{r,-1} = T_{r,-2} + \frac{\left[m_{water} c_{p,water}\left(T_{water} - 100\right) - m_{water}\lambda_{water}\right]}{Q_{rock} c_{p,rock}\left\{T_{r,-2}\right\}} \tag{4.16}$$

where $T_{r,-1}$ is the rock temperature after water injection (°C), $T_{r,-2}$ is the rock inlet temperature (°C), m_{water} is the water application rate (kg sec^{-1}), $c_{p,water}$ is the heat capacity of water (J kg^{-1} K^{-1}), T_{water} is the temperature of the water (°C), λ_{water} is the latent heat of evaporation of water (J kg^{-1}), Q_{rock} is the rock flow rate (kg sec^{-1}), and $c_{p,rock}\{T_{r,-2}\}$ is the heat capacity of the rock (J kg^{-1} K^{-1}) at temperature $T_{r,-2}$. The rock temperature after water application is 111.8 °C for rock input temperature of 126.7 °C and typical operating conditions.

The heat capacity of the rock was modeled with the equation:[45]

$$c_{p,rock}\left\{T(^{\circ}C)\right\} = 680.52 + 2.3738T - 6.1x10^{-3}T^{2} \tag{4.17}$$

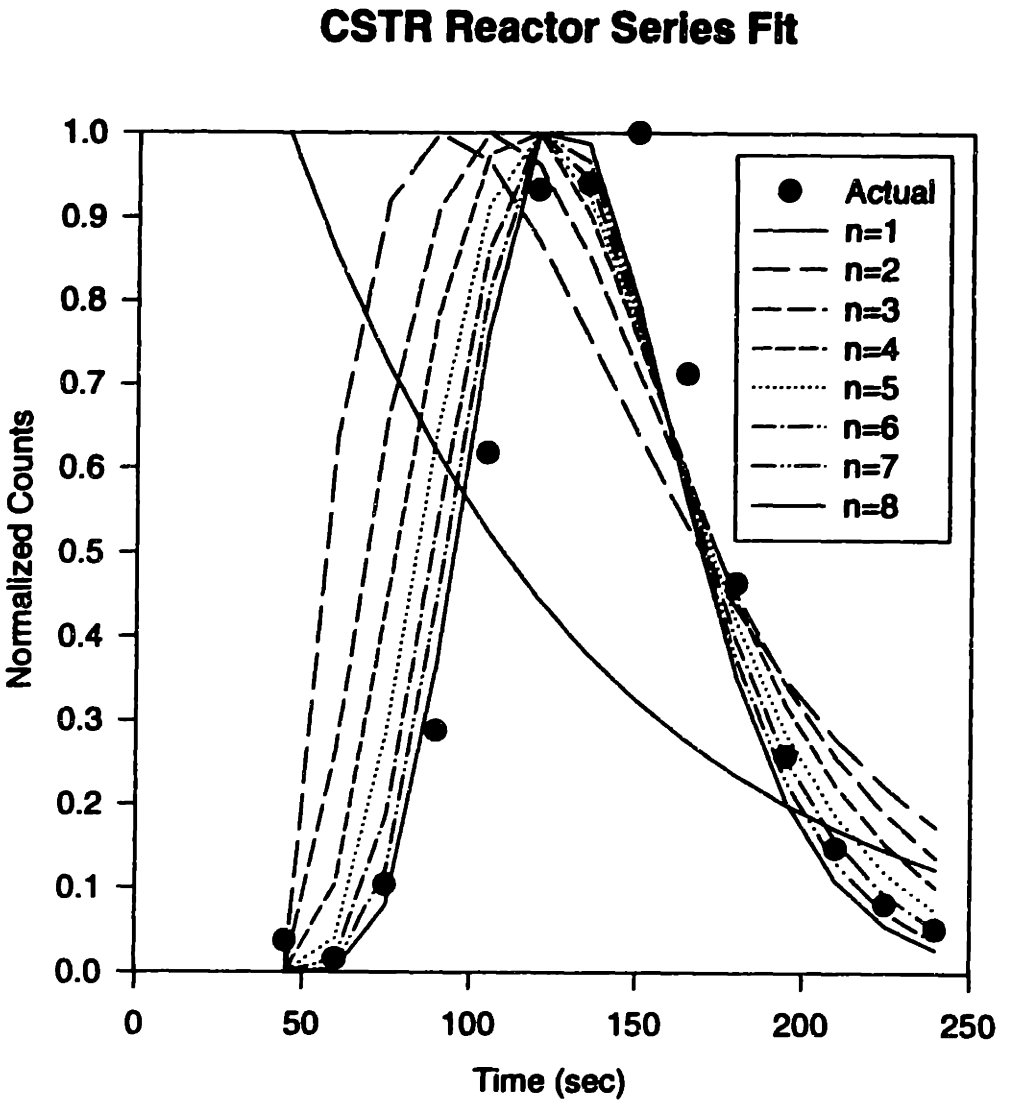

Figure 4.11 Plot of residence time data from Figure 4.2 and output of Equation 4.14 for n=1,2,3,4,5,6,7,8.

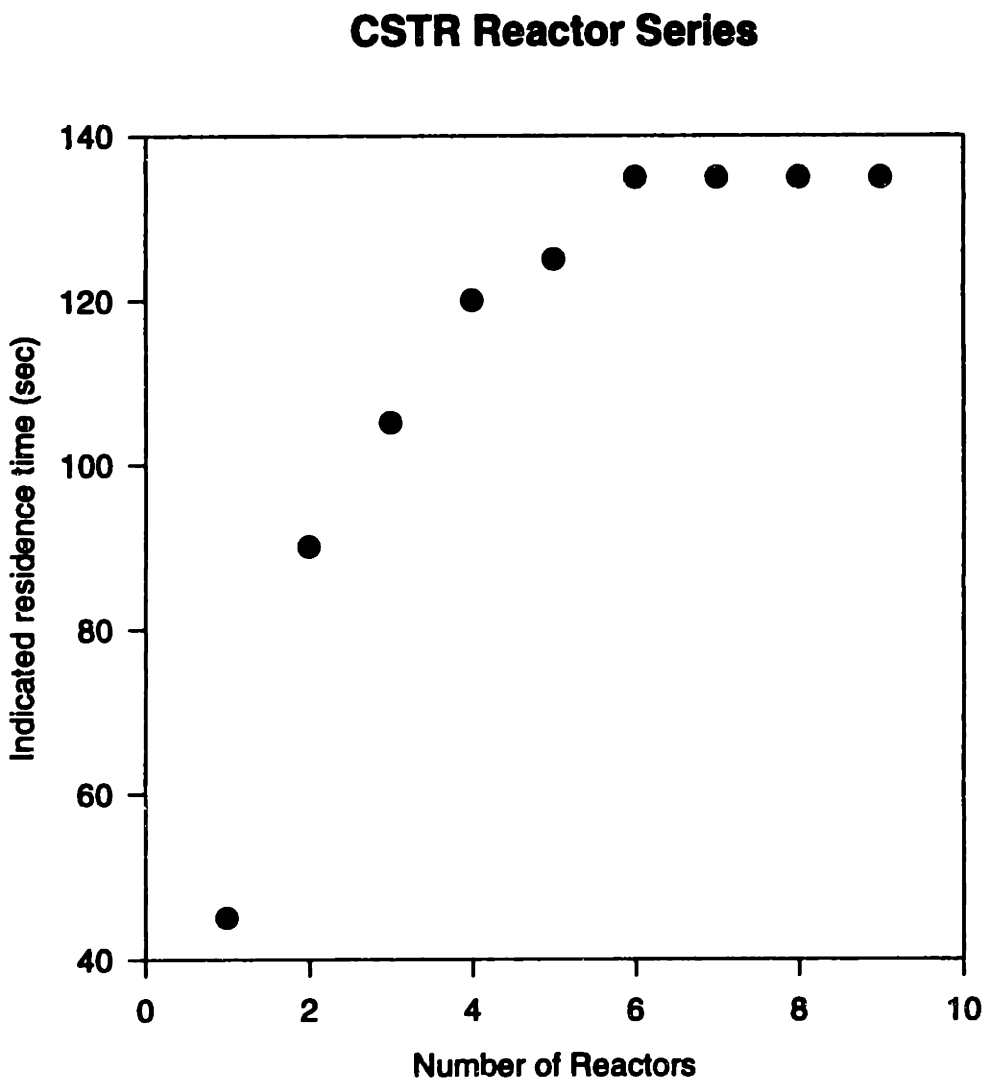

Figure 4.12 Plot of predicted residence time of the fits in Figure 4.11 vs. value of *n*.

The rock temperature after slurry application was calculated as follows:

$$T_{r,0} = \frac{Q_{rock} C_{p,rock} T_{r,-1} + T_{slurry}\left[m_{slurry} f c_{p,solids} + m_{slurry}(1-f) c_{p,water}\right]}{c_{p,rock} Q_{rock} + m_{slurry} f c_{p,solids} + m_{slurry}(1-f) c_{p,water}} \tag{4.18}$$

where $T_{r,0}$ is the rock temperature after slurry injection (°C), $T_{r,-1}$ is the rock temperature after water injection calculated in Equation 4.16, T_{slurry} is the slurry injection temperature (24 °C), m_{slurry} is the slurry application rate (kg sec^{-1}), f is the volume fraction solids in the slurry (0.65), and $c_{p,solids}$ is the heat capacity of the slurry solids (880 J kg^{-1} K^{-1}).

The moisture content of the rock/slurry mixture was calculated by adding the water injected to the water in the slurry:

$$Q_{w,0} = m_{water} + (1-f) m_{slurry} \tag{4.19}$$

This rock stream temperature and moisture content was used as the input to the first CSTR. Each CSTR had four unknowns: rock temperature ($T_{r,n}$), air temperature ($T_{a,n}$), rock moisture content ($Q_{w,n}$), and air humidity ratio (H_n). The humidity ratio is defined as the mass of water vapor per unit mass of dry air. It is related to the relative humidity, ϕ, by the following formula:

$$H = \frac{\frac{\phi}{100\%} P_{sat} \frac{MW_{water}}{MW_{air}}}{P_{total} - \frac{\phi}{100\%} P_{sat}} \tag{4.20}$$

where P_{sat} is the saturation vapor pressure of water as a function of temperature (Pa):[45]

$$P_{sat} = \begin{cases} T < 60°C, \dfrac{101325}{760} 10^{(8.10765 - 1750.286/(T(°C)+235))} \\ T \geq 60°C, \dfrac{101325}{760} 10^{(7.96681 - 1668.21/(T(°C)+228))} \end{cases} \quad (4.21)$$

MW_{water} is the molecular weight of water (18001 kg mol^{-1}), MW_{air} is the molecular weight of air (29000 kg mol^{-1}), and P_{total} is the total pressure of the system (101,325 Pa).

There are four governing equations for each CSTR: a heat flux equation between the rock/slurry stream and the air stream, a moisture flux equation between the rock/slurry stream and the air stream, an energy balance in the reactor, and a mass balance in the reactor.

The heat flux equation is:

$$\Delta Q = -hA(T_{r,n-1} - T_{a,n+1}) \quad (4.22)$$

where ΔQ is the heat lost by the rock and gained by the air (J sec^{-1}), h is the heat transfer coefficient (J sec^{-1} m^{-2} K^{-1}), A is the area over which the heat transfer occurs (m^2), $T_{r,n-1}$ is the rock temperature output from the previous CSTR, and $T_{a,n+1}$ is the air temperature output from the next CSTR to represent a counter-current airflow. h and A were not known separately, since the flights lift the material and create a large, unknown surface area; therefore, the product hA was treated as a parameter of the model and used in the optimization process, see Section 4.5.3 below.

The mass transfer equation in each CSTR is:

$$m_{vap,n} = h_m A\left[\rho_{sat.air}\{T_{r,n}\} - \frac{\phi}{100\%}\rho_{sat.air}\{T_{a,n}\}\right] \quad (4.23)$$

where $m_{vap,n}$ is the mass of water vaporized in CSTR n (kg sec^{-1}), h_m is the mass transfer coefficient (m sec^{-1}), A is the area over which mass transfer occurs (m^2), $\rho_{sat.air}\{T\}$ is the density of saturated air (kg m^{-3}) at temperature, T, and ϕ is the relative humidity (%).

The density of saturated air (kg m^{-3}) was calculated as follows:[45]

$$\rho_{sat\,air} = \frac{P_{sat}\{T\}MW_{water}}{R[T(^{\circ}C)+273.15]} \tag{4.24}$$

where $P_{sat}\{T\}$ is the saturation vapor pressure as calculated in Equation 4.21, MW_{water} is the molecular weight of water (18001 kg mol^{-1}), and R is the gas constant (8.314 J mol^{-1} K^{-1}).

The mass transfer coefficient and area in Equation 4.23 are again unknowns for the same reasons given above for the heat transfer equations. The product h_mA was used as an optimization parameter in Section 4.5.3.

The energy balance in each reactor was considered by assuming an adiabatic system. Any heat lost by the rock/slurry stream and the energy required to vaporize water would be gained by the air. The energy balance equation is:

$$\begin{aligned}&\left(Q_a c_{p,air}\{T_{a,n}\} + Q_a H_n c_{p,vap}\{T_{a,n}\}\right)\left(T_{a,n+1} - T_{a,n}\right) - m_{vap,n}\lambda_{water} = \\ &\left(Q_r c_{p,rock}\{T_{r,n}\} + m_{slurry} f c_{p,solids} + Q_{w,n} c_{p,water}\right)\left(T_{r,n-1} - T_{r,n}\right)\end{aligned} \tag{4.25}$$

where Q_a is the air flow rate (0.1394 kg sec^{-1}), $c_{p,air}\{T_{a,n}\}$ is the heat capacity of air (J kg^{-1} K^{-1}) at temperature $T_{a,n}$, and $c_{p,vap}\{T_{a,n}\}$ is the heat capacity of water vapor (J kg^{-1} K^{-1}) at temperature $T_{a,n}$. The equations used to calculate the heat capacity of air and water vapor for temperature in °C, are:[45]

$$c_{p,air} = 6.713 + 4.697x10^{-4}T + 1.147x10^{-6}T^2 - 4.696x10^{-10}T^3 \tag{4.26}$$

and

$$c_{p,vap} = 6.97 + 3.464x10^{-3}T - 4.833x10^{-7}T^2 \tag{4.27}$$

Each side of the energy balance in Equation 4.25 can be set equal to ΔQ, the heat flux between the rock/slurry stream and the air stream calculated in Equation 4.22. This gives two equations that can be solved for the temperature of the rock/slurry stream in each reactor:

$$T_{r,n} = T_{r,n-1} + \frac{\Delta Q}{Q_r c_{p,rock}\{T_{r,n}\} + m_{slurry} f c_{p,solids} + Q_{w,n} c_{p,water}} \tag{4.28a}$$

and the air stream in each reactor:

$$T_{a,n} = T_{a,n+1} - \frac{\Delta Q + m_{vap,n}\lambda_{water}\{T_{a,n}\}}{Q_a c_{p,air}\{T_{a,n}\} + Q_a H_n c_{p,vap}\{T_{a,n}\}} \tag{4.28b}$$

The final equation in each CSTR is the mass balance. The flow rates of rock, slurry solids, and air are assumed to be constant in each CSTR, so the flow into the CSTR equals the flow out. Hence, these flow rates do not appear in the mass balance. The only substance that must balance is the water:

$$m_{vap,n} = Q_a\left(H_n - H_{n+1}\right) = Q_{w,n-1} - Q_{w,n} \tag{4.29}$$

4.5.3 MODEL IMPLEMENTATION AND RESULTS

A computer program was written in Labview[46] to calculate Equations 4.22, 4.23, 4.28(a), 4.28(b), and 4.29 iteratively until a solution was found. The solution was allowed to converge until the following condition was met:

$$\sum_n \left(T_{r,n,j} - T_{r,n,j-1}\right)^2 \le 0.01 \tag{4.30}$$

where $T_{r,n,i}$ is the rock temperature in the nth CSTR in the current iteration cycle, i, and $T_{r,n,i-1}$ is the rock temperature in the nth CSTR in the previous iteration cycle, $i-1$. Operating parameters taken from the pilot plant mixer used to perform the residence time experiments in Section 4.2 were used as the input parameters. A set of known outputs; rock outlet temperature of 55 °C and rock outlet moisture content of 0.7 wt. %, was used to optimize the model. The parameters hA and h_mA were varied until the correct outputs were obtained. The optimized values were hA=223 J sec^{-1} K^{-1}, and h_mA=1.51x10^{-3} m^3 sec^{-1}.

These optimized values were used to obtain plots of rock temperature (Figure 4.13a), air temperature (Figure 4.13b), rock moisture (Figure 4.13c), and air relative humidity (Figure 4.13d). Each value is plotted versus distance from the mixer entrance. Additional data are plotted corresponding to the air inlet temperature and air inlet humidity. Rock temperature data after water injection and after slurry injection are also shown.

Several features of the data are notable. The rock temperature shows continuous decrease through the length of the mixer; however, the air temperature does not change monotonically. The air temperature rises when moving from the inlet then it falls when passing through the upper portions of the mixer. This drop in temperature is due to the large evaporation of water in this section. The rock moisture data confirms this, and indicates that much of the drying occurs during the first 40 cm, or approximately the first one-third of the screw flights.

The optimized model was run with varying operating parameters to test the sensitivity of the model. Rock inlet temperature ($T_{r,-2}$) and slurry application rate (Q_s) were the operating parameters varied, and the output rock moisture content ($Q_{w,6}$) was the output parameter observed, as this has been found to be a good indicator of granule quality.[14]

Figure 4.14 is a plot of output rock moisture content as a function of rock inlet temperature. The open circle represents the conditions used to optimize the model. The data has been fitted to a straight line with a slope of -3.340x10^{-2} wt.% $°C^{-1}$ and an r^2=0.995. Values of output rock moisture content that have been found to be acceptable

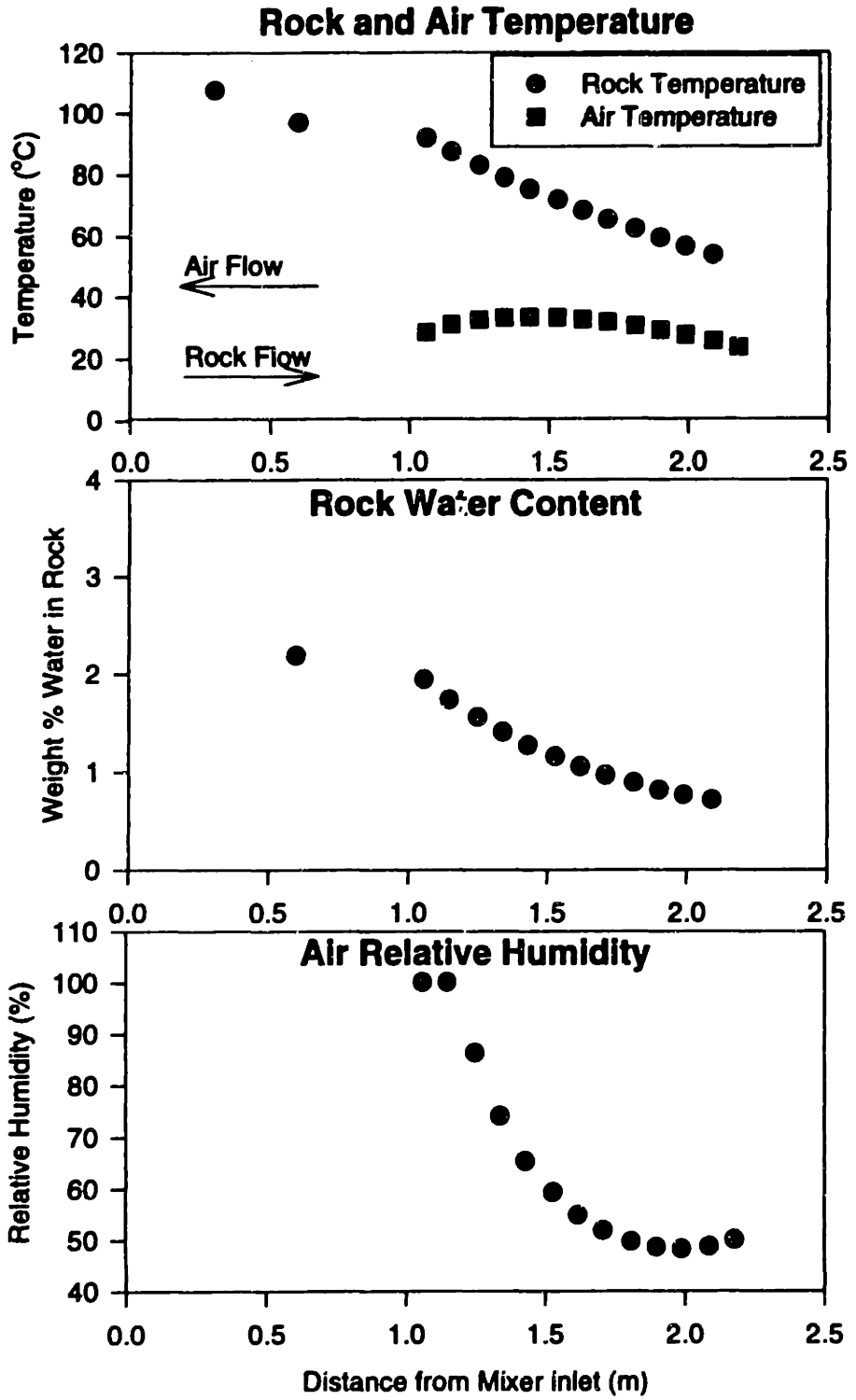

Figure 4.13 Output of mixer model for (a) rock temperature and air temperature, (b) rock moisture content, and (c) air relative humidity. Input rock temperature was 126.67 °C, hA=223, and h_mA=1.51x10^{-3}.

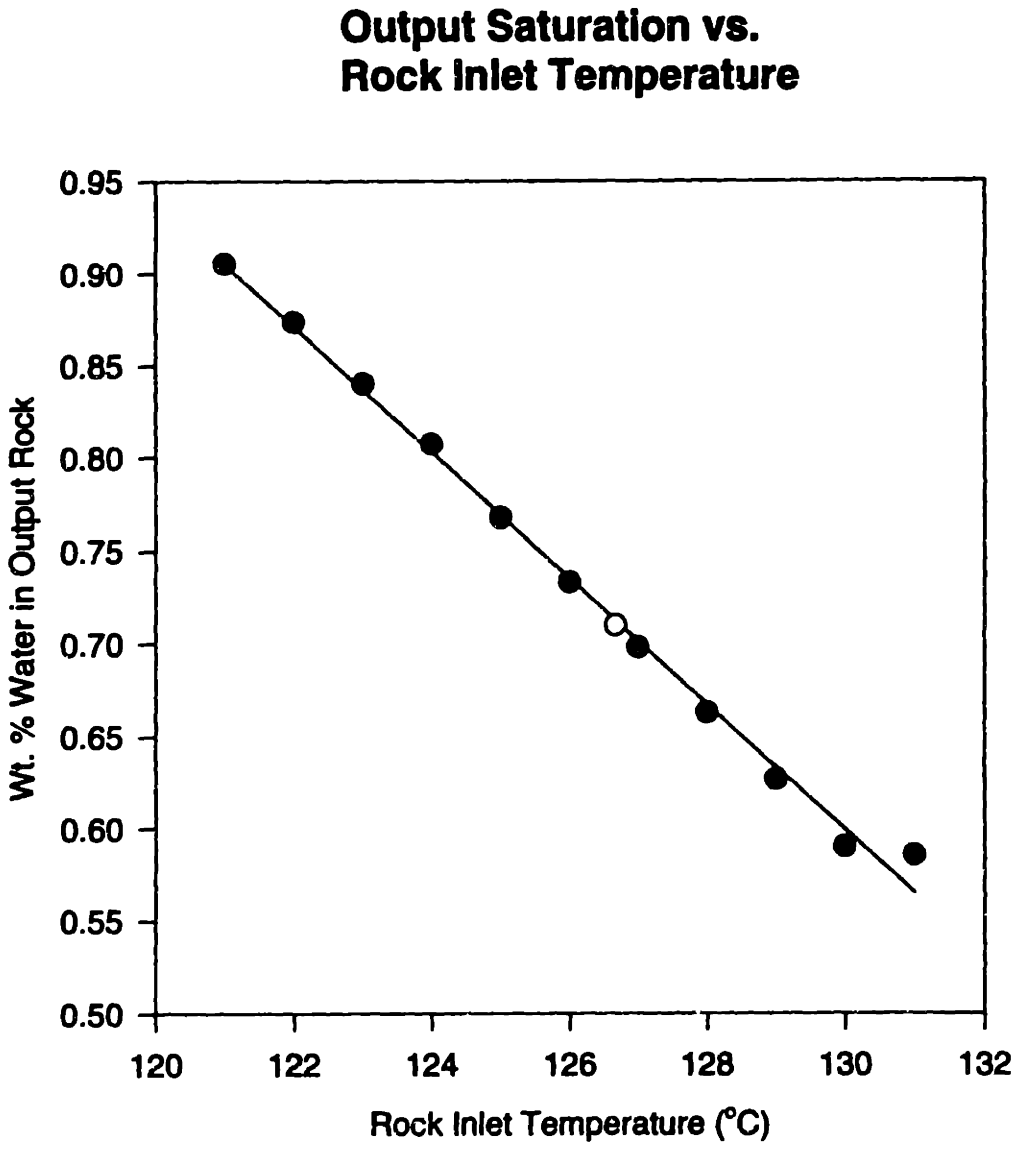

Figure 4.14 Rock output moisture content vs. rock inlet temperature. From mixer model, hA=223 and h_mA=1.51x10^{-3}. Open circle represents conditions used for optimization. Linear fit has a slope of -0.0340 wt.% °C^{-1}.

range from 0.6-0.8 wt.%.[14] Inlet rock temperature must be controlled to 127 ± 2 °C to achieve this moisture content. This temperature control is much more precise than current controls on the process.

Figure 4.15 is a plot of output rock moisture content as a function of slurry application rate. The open circle represents the conditions used to optimize the model. The data was fitted to a straight line with a slope of 155 wt.% sec kg^{-1} and an r^2=0.9999. The range of slurry application rates shown in the graph is the optimized rate ±10%. The slurry application rate must be controlled to within ±5% to assure the proper output rock moisture content. This level of control is within the capabilities of the current process.

4.6 CONCLUSIONS

The residence time experiments in this chapter show that granules move through the mixer at different speeds in different sections of the mixer. The overall residence time distribution is quite broad and shows two distinct peaks, one with approximately double the residence time of the other. The separation of the distribution into two peaks is probably due to granules sticking to the walls of the mixer in the slurry application section, while the broadening of the distribution is due to back-mixing in the screw flights.

The variability in residence time from granule to granule is a concern for coating quality and uniformity; however, most granules spend approximately the same amount of time in the spreading portion of the mixer and the variability comes in the drying phase. This variability, caused by the action of the flights, is the tradeoff for increased drying rates due to larger surface area presented to the air flow and the decreased segregation caused by the lifting action.

The mixer model indicates that most of the drying occurs during the first third of the screw flights' length. The model also shows that the output rock moisture content is very sensitively dependent on inlet rock temperature. This is the single most important parameter controlling the drying rate. Better control over this parameter would increase

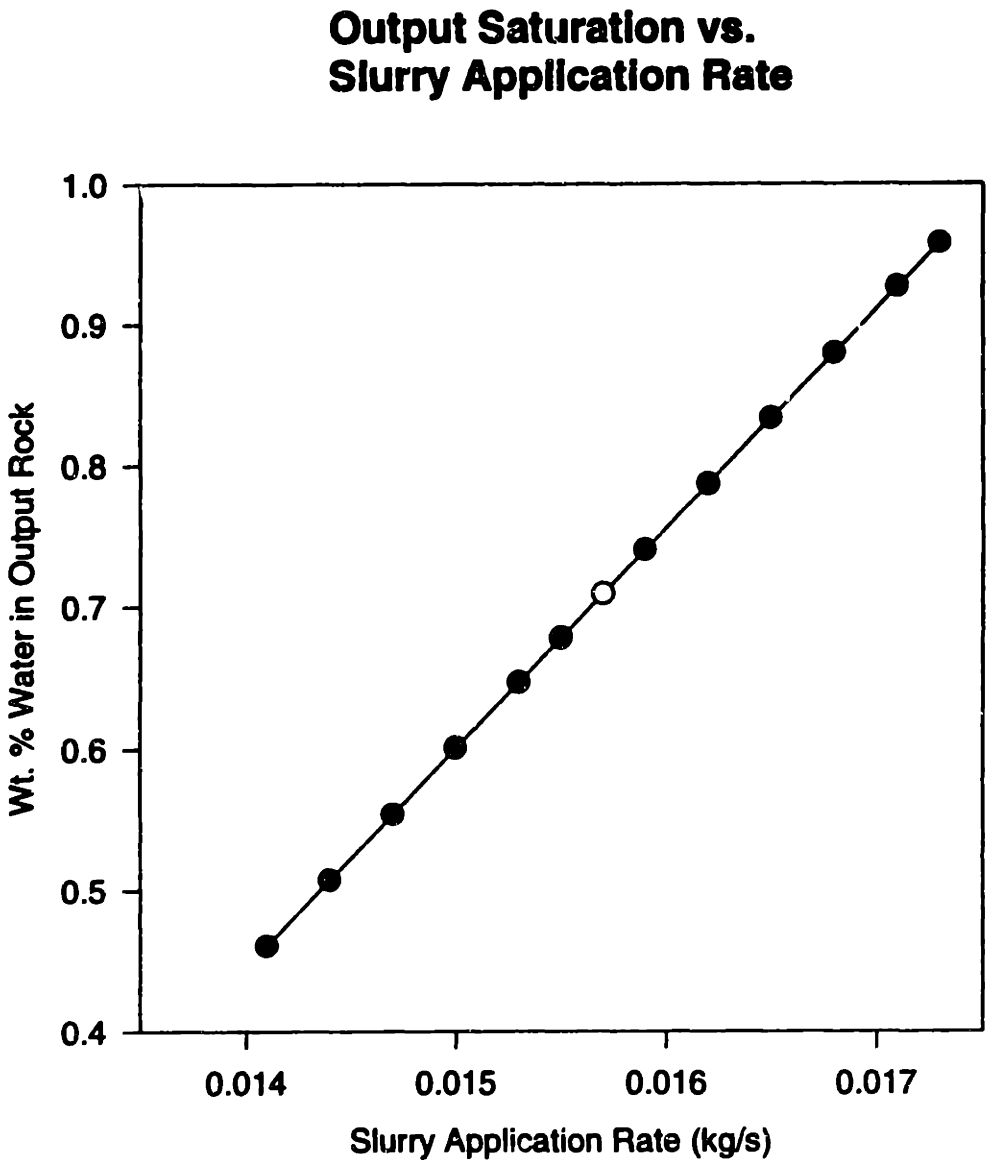

Figure 4.15 Rock output moisture content vs. slurry application rate. From mixer model, hA=223 and h_mA=1.51x10^{-3}. Open circle represents conditions used for optimization. Linear fit has a slope of 155 wt.% sec kg^{-1}.

process control. A major difficulty will be the long time constant required for the pre-heater to reach steady state, so any feedback control system would have difficulty eliminating variations in input to the mixer.

The model treats the screw flight section of the mixer as a series of Continuous flow Stirred Tank Reactors (CSTR's) due to the back mixing of the screw flights. This is in contrast to a plug flow analysis typically used by other authors, which is applicable to mixers without flights.

CHPATER 5
COATING SOLUBILITY AND LEACHING

5.1 INTRODUCTION

Optical properties are one of the key measures of granule and coating quality; weatherability is another. A roofing granule must maintain its optical properties for the guaranteed lifetime of the shingle, typically 10 years or more. It must resist degradation of the coating due to environmental effects during this period, principally rainwater.

A dried, but unfired, coating on a roofing granule is highly soluble in water. It was known that the firing process induced chemical changes in the coating material that made it highly insoluble in water and resistant to weathering effects, but a mechanism for this change was not known. This chapter will explore the chemical changes in the coating, describe the mechanism, and will present a means of evaluating future coating formulations. Section 5.2 will describe the standard industry tests used to evaluate roofing granule weatherability. Section 5.3 will describe laboratory methods to determine rates of dissolution from the coating for two of the principal species. Section 5.4 will describe the experimental observations. Section 5.5 will present a discussion of the experimental results and the effect of trace quantities of aluminum ions on coating solubility. It will be shown that the clay releases aluminum ions during the firing process and makes the coating insoluble. Section 5.6 will present conclusions for this chapter.

5.2 ALKALINITY TEST

Roofing granule coatings are evaluated in industry in exposure tests lasting up to six years. These tests are often performed in extreme climates, with large yearly rainfalls and

extremely strong sunshine.[14] A long test period is unacceptable for evaluating daily production runs of the product where feedback between measured quality and changes in the operating conditions must be made hourly or more often. Any test developed must provide data very quickly, yet must also correlate with data obtained by long term exposure tests.

A standard test of coating weatherability has been developed in industry. The accelerated test, known as the alkalinity test, uses boiling water to increase the simulated weathering. The standard test procedure calls for the addition of 25 g of granules to boiling water. The granules remain in the water which is kept at the boiling point for the duration of the test. Typical test times are 5 minutes, 15 minutes, or 24 hours. The granules are removed from the water after completion of the test and a small quantity of phenolphthalein indicator is added to the test solution. The indicator makes the test solution turn pink due to the hydroxide ions that dissolved from the coating. The test solution is titrated with 0.1 N sulfuric acid until the indicator turns colorless, at ~7.5 pH. The alkalinity reported is the volume of acid required to titrate the solution. A lower alkalinity is considered better, since it seems to indicate that a smaller amount of the coating has dissolved in the test.[14]

Data from the alkalinity tests have been compared with the results of long-term exposure tests, and the 15 minute alkalinity test was found to correlate well with the exposure data.[14] The test is also much quicker than the 24 hour test, and fulfills the need for a process control test with quick feedback times.

5.3 EXPERIMENTAL PROCEDURES

Leach rates of several coating components were measured using chemical trace analysis of the leach solution in order to determine which species in the coating were dissolving. Leach rates were determined by measuring the concentration of the species in a leach solution prepared in a manner similar to the alkalinity test. A sample of granules or a laboratory prepared coating was immersed in boiling water for a specified time. The

sample was removed after the test and the volume of the resulting solution was measured immediately.

Samples of the leach solution were removed for chemical analysis to determine the mass of the species of interest in the sample. The leach rate was calculated based on the mass measured m_1, the size of the sample V_1, the total leach solution volume V_0, the area of the coating A (estimated from granule geometry), and the time of the leach test t.

$$rate = m_1 \frac{V_0}{V_1} \frac{1}{tA} \tag{5.1}$$

5.3.1 SILICA LEACH RATE

The aqueous silica concentration was measured using a test adapted from Iler.[48] 1-20 ml of a solution containing up to 50 μg of silica was diluted with deionized water to 20 ml volume. 3 ml of a molybdic acid solution (20 g l^{-1} $(NH_4)_6Mo_7O_{24} \cdot 4H_2O$, 60 ml l^{-1} 36% HCl) is added to the sample and allowed to react for ten minutes. The molybdic acid reacts with silica to form a yellow colored silicomolybdic acid complex. This complex is reduced with a reducing agent to a blue colored complex for increased test accuracy. The reducing agent is freshly prepared for each test as follows: 100 ml stock solution A (an aqueous solution of 20 g l^{-1} 5-amino-2-hydroxytoluene sulfate and 12 g l^{-1} Na_2SO_3), 60 ml stock solution B (100 g l^{-1} of oxalic acid in water), 120 ml 9 N H_2SO_4, and 20 ml deionized water. The reducing agent was allowed to react with the silicomolybdic acid complex for three hours.

The absorbance of the test solution was measured at 810 nm in a Beckman DU640 UV/Visible spectrophotometer.[18] Deionized water was tested for silica with the same procedure and used as a blank. The absorbance was converted to concentration by comparison with the absorbance measured for a 40 ppm standard prepared by heating 1.00 g amorphous silica and 4.00 g NaOH to 800 °C in a nickel crucible. The cooled mixture was dissolved in warm water and diluted to 1 liter volume to make a 1000.0 ppm

standard. 40 ml of this standard was added to 600 ml 0.1 N H_2SO_4 and made up to 1 liter to make a stable 40 ppm standard.[48]

5.3.2 SODIUM LEACH RATE

Sodium concentrations in the leach solutions were measured with a sodium sensitive ion selective electrode.[49] The electrode potential measured was compared with measurements performed on 10 and 100 ppm standards.[50] The formula used to calculate concentration is:

$$C = C_s \cdot 10^{(E-E_{100})/S} \tag{5.5}$$

where C_S is the concentration of the standard, usually 100 ppm, E is the measured potential in the sample, E_{100} is the measured potential in the 100 ppm standard, and S is the slope:

$$S = (E_{100} - E_{10}) \tag{5.6}$$

where E_{10} is the potential measured in the 10 ppm standard.

5.3.3 ALUMINUM LEACH RATE

Aluminum was detected using a procedure described by James et al.[51] A known volume of the test sample containing 0.1 to 20 μg of aluminum ion is added to a culture tube containing 5 ml of a 1 M sodium acetate solution, 10 ml deionized water, and 4 ml of a 1% 8-hydroxyquinoline solution. The tube is capped and shaken vigorously for 15 seconds, during which time the aluminum forms a complex with the hydroxyquinoline.

The complex is extracted by adding 5 ml of butyl acetate and shaking the culture tube.

The organic phase is collected and transferred to a borosilicate glass cuvette and the absorbance measured at 395 nm. A sample of pure deionized water was tested for aluminum content in the same manner, and the organic phase extracted was used as a reference blank for the spectroscopy measurements.

Absorbance was converted to concentration of aluminum by comparing with a standard. A stock standard was prepared by dissolving 3.331 g $Al_2(SO_4)_3 \cdot 18H_2O$ in 0.1 liter of 0.1 M HNO_3 and diluting to 1 liter. This stock solution, at a concentration of 134.885 $\mu g\ ml^{-1}$, was diluted by adding 14.0 ml stock standard to 0.86 ml concentrated HNO_3 and making up to 100 ml. This standard contained 18.9 μg aluminum ml^{-1}.

5.3.4 CLAY LEACHING

Clays similar to those used in granule production were tested for aluminum content by heating 1.0 g of clay in 10 ml of deionized water in a sealed pressure vessel. The pressure vessel (Parr Instrument Company[47]) was made from Inconel stainless steel and rated to 3000 psi at 350 °C. The vessel was heated to typical firing temperatures and cooled down. The volume of water was chosen to exceed the volume of water required to saturate the atmosphere in the vessel at the temperature of the run, so that liquid water would remain in the vessel at all times. The water in the vessel was recovered and tested for aluminum as described in Section 5.3.3.

5.4 OBSERVATIONS

A leach solution was prepared by boiling 25 g of roofing granules in 75 ml deionized water for 15 minutes. The granules were removed and the three tests described above were performed on the solution. The measured leach rates for the three components measured are 0.733 μg silica $mm^{-2}\ min^{-1}$, 1.47 μg sodium $mm^{-2}\ min^{-1}$, and less than

0.01 μg aluminum mm^{-2} min^{-1}. These calculation are based on three samples and an estimated surface area of 10 mm^2 per gram of granules. Alkalinity tests performed on granules from the same batch indicated an alkalinity of 1.05-1.10 ml acid to titrate, which is comparable to value measured at the production plant.[14]

The principal components of the matrix material, the silica and the sodium, are leaching from the coating, but at different rates. The molar ratio of silica to sodium in the silicate is 2.75:1, but the molar ratio of silica to sodium in the leach solution was 1:3.21. Sodium is leaching from the coating much faster than the silica. Aluminum, a major component of the clay, was not detected in the leach solution.

The leaching and alkalinity tests were extended to laboratory prepared coatings in order to study the role of the various coating components. Laboratory coatings were dip cast on 2.5 cm x 7 cm glass microscope slides. The coatings were dried in air for 4-5 hours then dried overnight in a vacuum oven at 60 °C. The dried coatings were heated at 3 °C min^{-1} to 450 °C and held for 18 minutes. The fired coatings were cooled in air and then leached in a similar manner to the granules. The area of the slide covered by the coating was typically 2000 mm^2.

Silica leach rates for a coating of this type prepared from the same slurry formulation as used to coat the granules were 0.725 μg mm^{-2} min^{-1} for a 15 minute leach test. This leach rate is very similar to the rate measured for the granules, indicating that the laboratory coatings were leaching in a manner similar to the granules. Figure 5.1 is a plot of mass of silica leached from a coating over time. The initial leaching of silica was linear for the first 15 minutes and then began to level off, probably because the silica saturated the test solution.

Figure 5.2 is a plot of silica leach rates for dip cast coatings prepared with sodium silicate and various weight fractions of clay. The upper curve is coatings that were dried but not fired, the lower curve is for fired coatings. The strong correlation between clay fraction and leach rate indicates that the clay has a major effect on coatings solubility, but only after firing. The fired and unfired samples that contain no clay (0 wt.%) showed very little difference in silica leach rate.

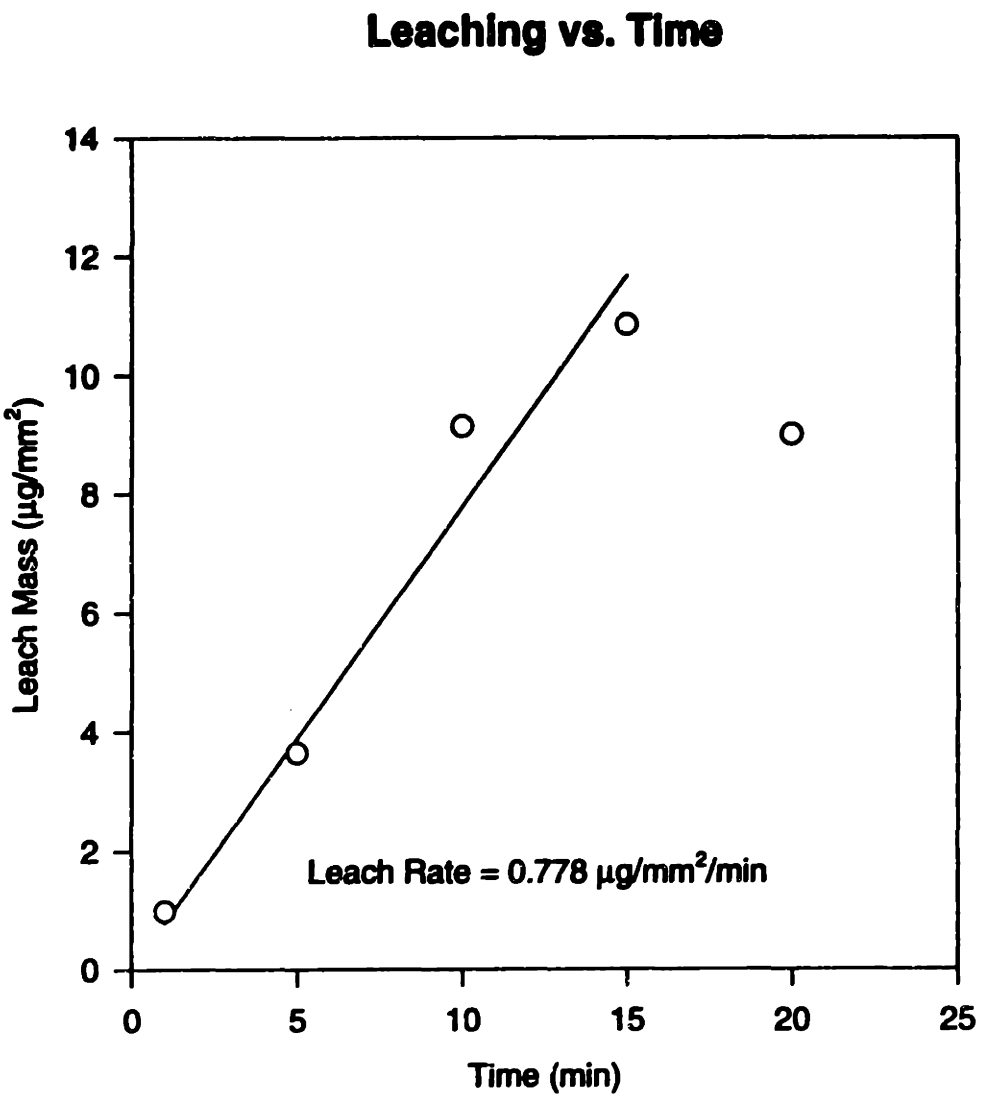

Figure 5.1 Plot of mass of silica leached from a dip cast coating vs. time.

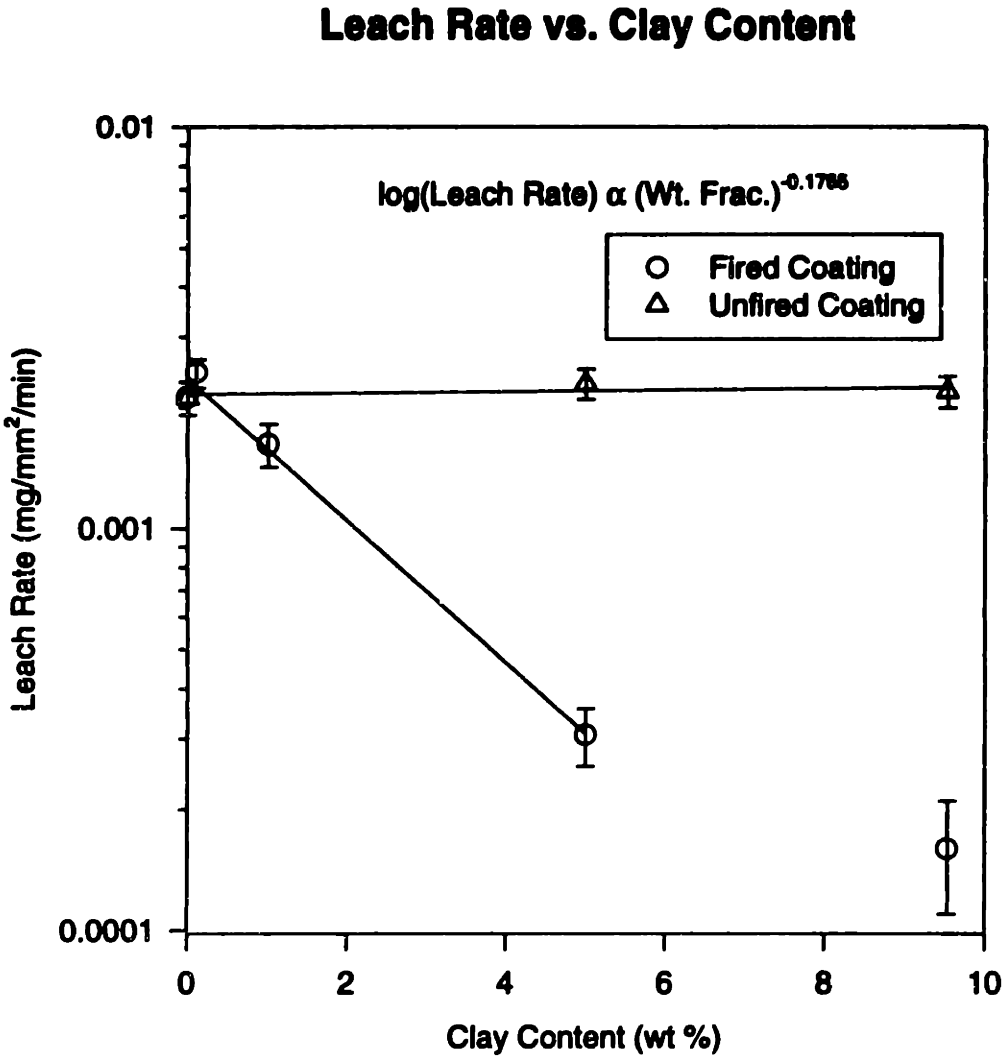

Figure 5.2 Plot of silica leach rate vs. weight fraction of clay in the slurry. Slurry contained silicate and clay only.

Figure 5.3 is a plot of aluminum leached from clays during heating in water in the pressure vessel. Aluminum is released from the clay when heated in water, but not during a room temperature soak in water.

5.5 DISCUSSION

Research by Iler[48] has shown that the presence of trace quantities of aluminum ions can reduce the solubility of silica by several orders of magnitude. Several methods to incorporate aluminum ions into the coating on roofing granules were attempted. Post-firing treatments apply aluminum containing solutions and have been shown to be effective in reducing alkalinity and solubility. Addition of aluminum salts to the coating slurry prior to application was unsuccessful because they cause slurry gelation. The data obtained from the clay leaching experiments in the pressure vessel indicates that the clay is releasing aluminum ions during firing.

5.5.1 POST-FIRING TREATMENTS

Post-firing treatments have been used in industry to reduce coating alkalinity.[14] These processes, often called "pickling," use an application of an aqueous aluminum salt solution to the granules. Application rates are low, typically 1-3 kg aluminum per 900 kg of granules. A reduction in alkalinity has been noted with pickling processes.[14]

Granules pickled in the laboratory with aluminum chloride solutions showed large reductions in alkalinity, silica leach rate, and sodium leach rate. 25 g of granules were treated with 10 ml of 0.01 M $AlCl_3$. The solution was added to the granules and allowed to dry in air prior to being leached as described in Section 5.2. See Table 5.1 for a summary of the alkalinity and leach rate data. Both silica and sodium showed significant reductions in leach rate. The alkalinity reported for the pickled granules is 0.0 ml

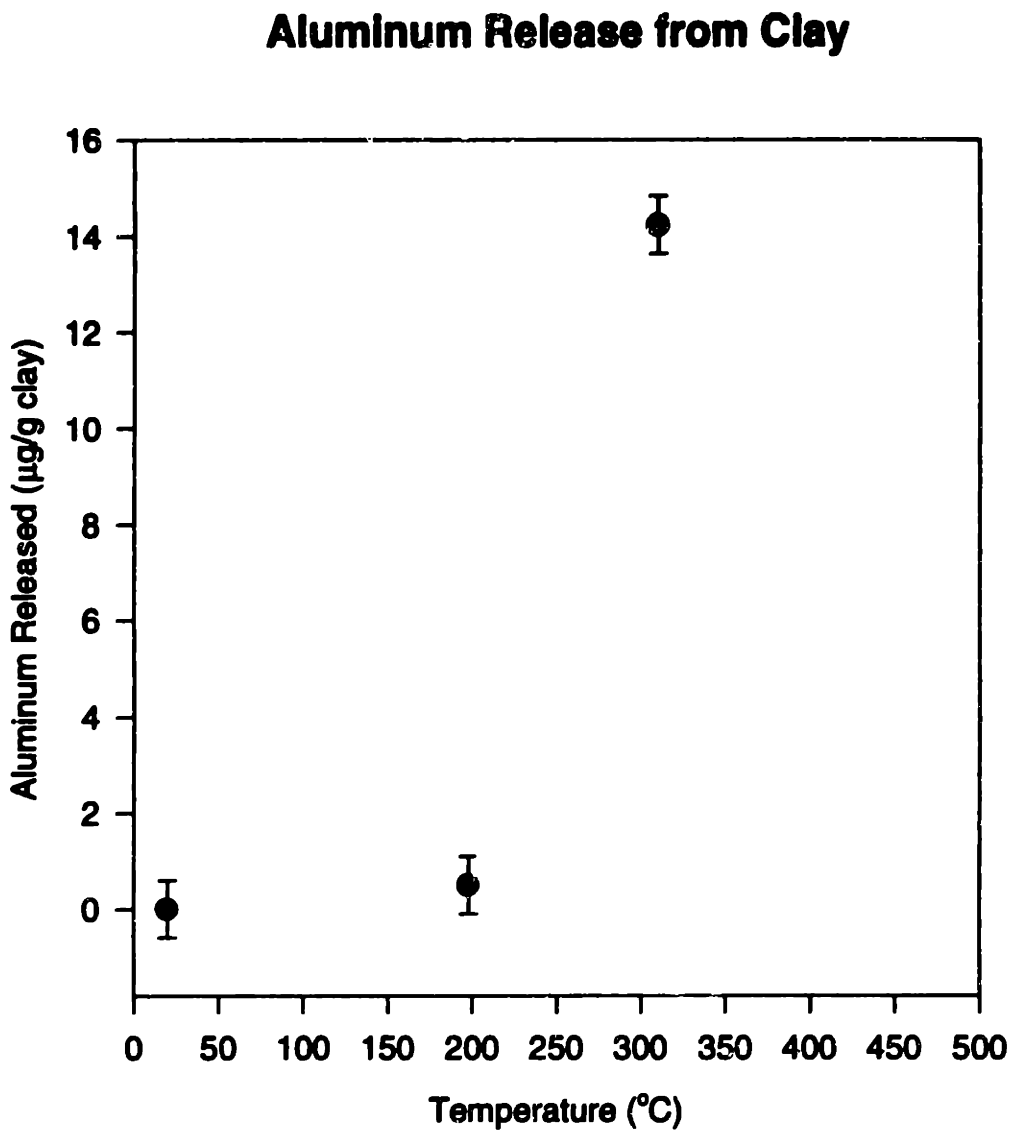

Figure 5.3 Aluminum released from clay vs. temperature.

because the phenolphthalein indicator failed to change color in the leach solution because the pH was 6.

Table 5.1 Summary of alkalinity and leach rates for roofing granules with and without an $AlCl_3$ pickling process.

	No Al^{3+}	With Al^{3+}
Alkalinity (ml acid)	1.1	0.0
Silica Leach Rate ($\mu g\ mm^{-2}\ min^{-1}$)	0.733	<0.067
Sodium Leach Rate ($\mu g\ mm^{-2}\ min^{-1}$)	1.467	0.480

Pickling processes cause reductions in alkalinity and leach rates, but this introduces another processing step to the production process, which increases production costs. The concentrations of aluminum used in the solution are much higher than the trace levels required to insolubulize the coating.

5.5.2 INCORPORATION OF ALUMINUM IONS INTO THE SLURRY

Silicate solubility can also be reduced by adding aluminum ions to the silicate in the gel form, before drying. Dip cast coatings were prepared from sodium silicate and varying concentrations of $AlCl_3$ salt; no clay or titania was included in the slurry. Figure 5.4 is a plot of silica leach rate versus aluminum ion concentration in the slurry. The circles are for the dip cast coatings prepared for silicate and $AlCl_3$. The dotted line represents the silica leach rate for a dip cast coating prepared from the normal roofing granule slurry.

The silica leach rate is strongly affected by the presence of aluminum ions. Small quantities of aluminum ions in the 10-30 ppm range lower the silica leach rate to levels comparable with the leach rate from a roofing granule coating (open circle). Higher levels of aluminum ions, 100 ppm in the slurry, show a higher leach rate than samples with less aluminum due to the fact that the high levels of aluminum cause the slurry to partly gel prior to casting. This partly gelled slurry is not suitable for the coating process.

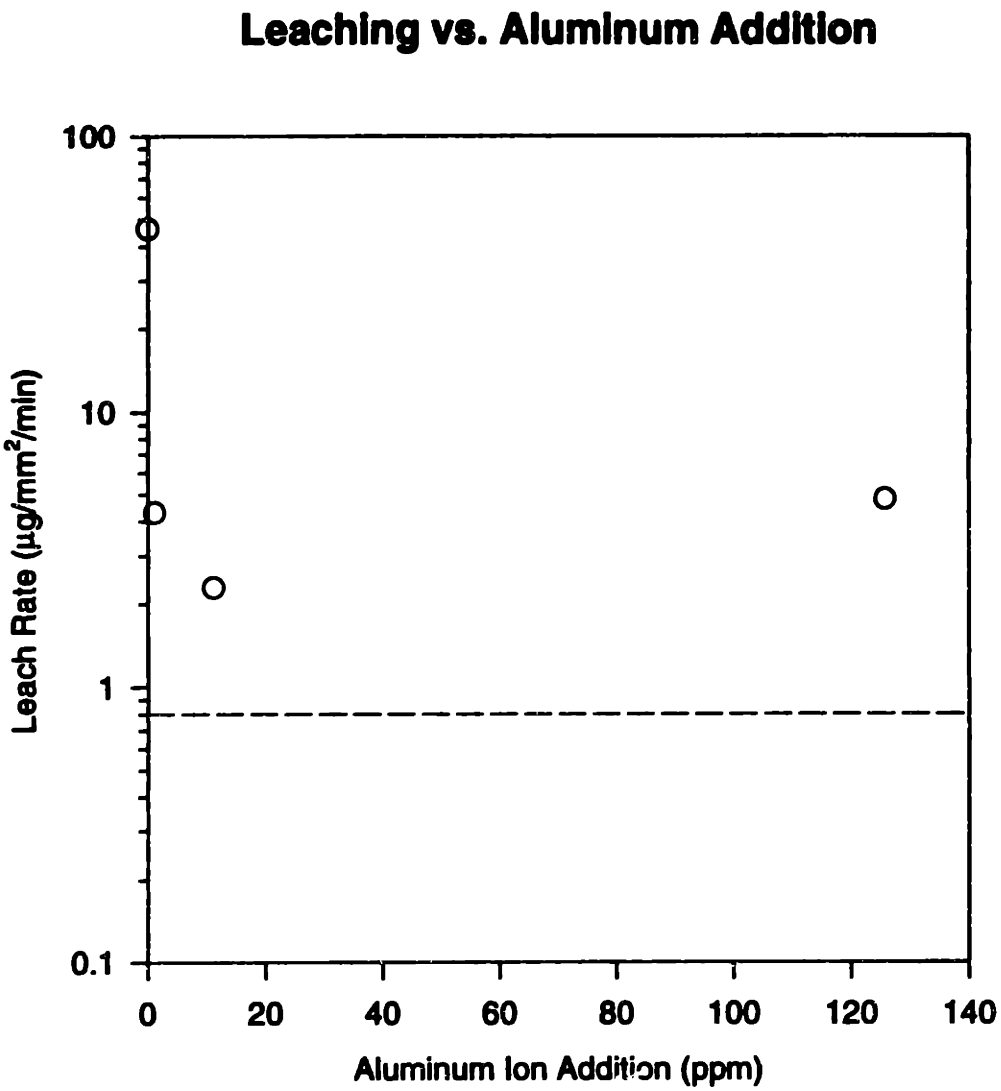

Figure 5.4 Plot of silica leach rate vs. aluminum ion concentration.

5.5.3 THE ROLE OF THE CLAY IN THE SLURRY

The role of the clay in the silicate slurries used to coat roofing granules is provide a source of aluminum ions to insolubulize the silicate matrix. The clays release the aluminum ions during the firing process to avoid the problem of slurry gelation.

The experimental protocol used to determine aluminum release from the clay can be used to evaluate various clays for use in the process. A clay with a higher aluminum release rate could be used in place of current clays, reducing the amount of clay required for the slurry. This would yield a savings in materials costs and reduce the yield stress of the slurry. The results of Chapter 3 indicate that lower yield stress would promote better penetration of the slurry into the rock bed and slurry spreading.

5.6 CONCLUSIONS

Unfired sodium silicate coatings are highly water soluble, and not very useful for the manufacture of roofing granules. The sodium silicate matrix is made insoluble by the incorporation of trace quantities of aluminum ions. Various methods were examined to introduce aluminum ions to the coating; release from the clay during the firing process was shown to be the most efficient.

CHAPTER 6
CONCLUSIONS AND FUTURE WORK

6.1 CONCLUSIONS

The goal of this thesis was to study bulk coating processes with sodium silicate slurries in order to determine what type of coating is desirable and which operating parameters are important to production of such a coating. The specific conclusions of this thesis are as follows:

(1) UV/Vis Diffuse Reflectance Spectroscopy was used to determine that the color of the coatings was constant for coating thicknesses greater than 25 μm, for the slurry formulation used in these experiments. The experimental protocols developed in this thesis can be used to determine optimal coating thickness for any slurry formulation.

(2) Optical microscopy of polished cross-sections of roofing granules showed that the coating currently being applied contained significant variations in thickness. Some areas were much thicker than required for consistent color, wasting coating material, and other areas were too thin, allowing the rock's absorption spectrum to alter the color of the granules. This highlights the need for better understanding of the coating process in order to produce a more uniform coating.

(3) Interaction of the slurry with polished rock section and rock granules showed that the presence of a thin film of water on the rock surface greatly enhances the spreadability of the slurry by lowering the contact angle between the slurry and the rock. This effect

was shown to be independent of rock temperature, although higher temperatures cause faster drying of the water film and provide a shorter time interval for spreading to occur.

(4) Slurry penetration into the rock bed in the mixer was shown to be a small fraction of the total bed depth for the conditions and slurry formulations studied in this thesis. This causes a layered structure of slurry on top of saturated slurry and rock on top of uncoated rock. This layered structure must be broken up by the tumbling of the mixer and the slurry distributed to all the granules.

(5) A Kozeny model of a shear-thinning slurry infiltrating a porous medium was developed which related the penetration depth of the slurry to the inverse of the room temperature yield stress of the slurry. The model predictions were verified with experimental data.

(6) Residence time studies of the mixer showed that the overall residence time distribution is quite broad, due to the "back mixing" of granules in the screw flights. These data were used to calculate average granule velocities through each section of the mixer. Back mixing was shown to be crucial to the bulk coating process, since it allows wet granules to dry in the presence of large numbers of dry granules. The non-wetability of wet slurry onto dried slurry, combined with back-mixing allows the production of defect free coatings.

(7) A mathematical model of the temperature and drying profiles in the mixer was developed, based on a series of continuous flow stirred tank reactors (CSTR's). This model showed that the output rock moisture content is strongly affected by changes in the inlet rock temperature. The drying rate is largely controlled by the inlet rock temperature.

(8) Leaching data from the coatings and clays showed that aluminum ions released from the clay during firing are responsible for making the coating insoluble in water. The experimental protocol developed in this thesis can be used to evaluate new clay materials

for suitability in the manufacture of roofing granules and has wider applicability to paints and other materials used to change the optical appearance of substrates.

(9) The experimental results indicate lower coating temperatures and higher water application rates prior to slurry application would lead to better spreading of the coating. These recommendations were implemented on an industrial roofing granule manufacturing mixer, and high quality coatings were produced using half the normal quantity of slurry used in the process. Coating thickness variability was reduced, so the minimum thickness requirements determined by optical measurements were met, without thicker regions that waste material. The reduction in slurry application rate resulted in significant cost savings in granule production.

6.2 SUGGESTIONS FOR FUTURE WORK

Several issues studied in this thesis warrant further investigation. The spectroscopy data was analyzed using the Kubelka-Munk remission function for optically "thick" materials. The data collected show that the coatings studied are not optically thick below 25 μm. Because the pigment used was white, a ratio of absorbance at different wavelengths was used to determine color. For a non-white pigment with absorption edges in the visible wavelengths, a modified derivation of the Kubelka-Munk model would be necessary to evaluate spectral data for coatings with these pigments.

The residence time data showed that residence time in the screw flights sets the amount of time available for the granules to dry. The acceptable moisture content of the product exiting the mixer is critical, so control of the drying time is necessary for production of a quality product. However, the relationship between operating conditions and residence time and drying rate are complex. Continuous measurement of the residence time during production would be useful to optimize operating conditions to produce the best product.

A tracer method would be ideal for measuring residence times; however, the methods developed in this thesis would be too time consuming and labor intensive for use in the

production process. An automated injection and detection system could be developed to introduce a tracer at set intervals and detect the output pulses in the product stream. A fluorescent dye could be used for this purpose, since it would be easy to detect in the output stream with a photodiode. The dye would be destroyed during the firing process, so the tracers would not contaminate the product.

Leach data indicated that aluminum from the clay insolubilized the silicate matrix so the coating would last on a roof. The clay also raises the yield stress of the slurry, which was shown to limit slurry penetration into the rock bed. A reduction in clay content in the coating would be desirable to promote better spreading and coating uniformity. Further research could be done to select clay sources with higher release rates of aluminum per unit weight clay.

BIBLIOGRAPHY

1. S.M. Smith and J.R. Stow, Ann. Appl. Biol., **104**, 383, (1984).

2. Hyun J. Park, Manjeet S. Chinnan, and Robert L. Shewfelt, J. Food Sci., **59**, 568, (1994).

3. Ashley Shih, Jeff Falkowsky, Neelan Choksi, and Joe Berghammer, "Continuous M&M's," 10.26 Class report, MIT, 1990.

4. Stuart C. Porter, Charles H. Bruno, and Gerald J. Jackson, "Pan Coating of Tablets and Granules," pp. 73-118, in Pharmaceutical Dosage Forms: Tablets, Volume 3, edited by Herbert A. Lieberman and Leon Lachman, Marcel Dekker Inc., New York, 1982.

5. e.g. Taketoshi Keshikawa and Hiroaki Nakagami, Chem. Pharm. Bull., **42**, 656, (1994).

6. Dale E. Wurster, "Particle Coating Methods," pp. 119-148, in Pharmaceutical Dosage Forms: Tablets, Volume 3, edited by Herbert A. Lieberman and Leon Lachman, Marcel Dekker Inc., New York, 1982.

7. Yoshiyuki Koida, Masao Kobayashi, Noriko Nagahama, and Masayoshi Samejima, Chem. Pharm. Bull., **34**, 5115, (1986).

8. Masayoshi Samejima, Goichi Hirata, and Yoshiyuki Koida, Chem. Pharm. Bull., **30**, 2894, (1982).

9. Hideki Ichikawa, Hiroyuki Tokumitsu, Kaori Jono, Tomoaki Fukuda, Yoshifumi Osako, and Yoshinobu Fukumori, Chem. Pharm. Bull., **42**, 1308, (1994).

10. Göran Källstrand and Bo Ekman, J. Pharm. Sci., **72**, 772, (1983).

11. e.g. A. G. Ozturk, S.S. Ozturk, B.O. Palsson, T.A. Wheatley, and J.B. Dressman, J. Controlled Release, **14**, 203, (1990).

12. Shinji Narisawa, Hiroyuki Yoshino, Yoshiyuki Hirakawa, and Kazuo Noda, Chem. Pharm. Bull., **42**, 1485, (1994).

13. L.X. Liu and J.D. Lister, Powder Technology, **74**, 215, (1993).

14. Bob Messner, 3M Corp., private communication.

15. Hunterlab, Reston, VA.

16. Richard Harold, "An Introduction to Appearance Analysis," p. 36 in Proceedings of SPIE, April 1983.

17. Commision Internationale de l'Eclairage (CIE), "Recommendations on Uniform Color Spaces, Color-Difference Equations, Psychometric Color Terms," supplement No. 2 to CIE Publication No. 15, Paris, 1978.

18. Beckman Instruments, Columbia, MD.

19. LabSphere Inc., North Sutton, NH.

20. Harvard University Mineralogical Laboratory, Harvard, MA.

21. P. Kubelka, F. Munk, Z. Techn. Physik, **12**, 593, (1931).

22. Deane B. Judd, Günter Wyszecki, Color in Business, Science, and Industry, Second Edition, John Wiley and Sons, 1963, pp. 387-394.

23. 3M Corp., St. Paul, MN.

24. Gaton, Warrendale, PA.

25. J. Kozeny, Ber. Wien. Akad., **136a**, 271, (1927).

26. Morton M. Denn, Process Fluid Mechanics, Prentice Hall, 1980, pp. 67-69.

27 Xiao Mei Xi and Xiao Feng Yang, J. Am. Ceram. Soc., **79**, 102, (1996).

28 Erik O. Einset, J. Am. Ceram. Soc., **79**, 333, (1996).

29 E. Taheri-Nassaj, M. Kobashi, and T. Choh, Scripta Materiala, **34**, 1257, (1996).

30. 3M Corp., Little Rock, AR.

31. W.C. Saeman, Chem. Eng. Prog., **47**, 508, (1951).

32. R. Rutgers, Chem. Eng. Sci., **20**, 1079, (1965).

33. V. D. Ryvkin, G.V. Telyatnikov, and L.N. Braginskii, Theor. Found. Chem. Eng., **6**, 362, (1972).

34. R. Hogg, K. Shoji, and L.G. Austin, Powder Tech., **9**, 99, (1974).

35. G. W. J. Wes, A.A.H. Drinkenburg, and S. Stermerding, Powder Tech., **13**, 177, (1976).

36. L. G. Austin, K. Shoji, R. Hogg, and J. Carlson, Powder Tech., **20**, 219, (1978).

37. A. Z. M. Abouzeid, D.W. Fuerstenau, and K.V.S. Sastry, Powder Tech., **27**, 241, (1980).

38. S. Das Gupta, D.V. Khakhar, and S.K. Bhatia, Powder Tech., **67**, 145, (1991).

39. X-Met, Boulder, CO.

40. A. R. Rogers, J. A. Clements, Powder Tech., **5**, 167, (1971).

41. J. P. Troudec, J. A. Dodds, "Global Geometrical Descriptions of Homogeneous Hard Sphere Packings," in Disorder and Granular Media, ed. D. Bideau and A. Hansen, North-Holland, New York, 1993, pp. 157-158.

42. G. Baumann, I.M. Janosi, and D.E. Wolf, Europhys. Lett., **27**, 203, (1994).

43. G. H. Ristow, Europhys. Lett., **28**, 97, (1994).

44. Charles G. Hill, Jr., An Introduction to Chemical Engineering Kinetics and Reactor Design, Wiley and Sons, New York, 1977, pp. 245-304.

45. Michelle Brincat, "Development of a Model for 3M Roofing Granule Mixers," 3M IMP Report, 1995.

46. National Instruments, Austin, TX.

47. Parr Instrument Company, Moline, IL.

48. R.K. Iler, The Chemistry of Silica, Wiley and Sons, New York, 1979, pp. 56-58, 98-101.

49. Corning Inc., Corning, NY.

50. Orion Research Inc., Boston, MA.

51. Bruce R. James, Christopher J. Clark, and Susan J. Riha, Soil Sci. Soc. Am. J., **47**, 893, (1983).